



National Library
of Canada

Acquisitions and
Bibliographic Services Branch

395 Wellington Street
Ottawa, Ontario
K1A 0N4

Bibliothèque nationale
du Canada

Direction des acquisitions et
des services bibliographiques

395, rue Wellington
Ottawa (Ontario)
K1A 0N4

Notice - Acquisition

Notice - Acquisition

NOTICE

The quality of this microform is heavily dependent upon the quality of the original thesis submitted for microfilming. Every effort has been made to ensure the highest quality of reproduction possible.

If pages are missing, contact the university which granted the degree.

Some pages may have indistinct print especially if the original pages were typed with a poor typewriter ribbon or if the university sent us an inferior photocopy.

Reproduction in full or in part of this microform is governed by the Canadian Copyright Act, R.S.C. 1970, c. C-30, and subsequent amendments.

AVIS

La qualité de cette microforme dépend grandement de la qualité de la thèse soumise au microfilmage. Nous avons tout fait pour assurer une qualité supérieure de reproduction.

S'il manque des pages, veuillez communiquer avec l'université qui a conféré le grade.

La qualité d'impression de certaines pages peut laisser à désirer, surtout si les pages originales ont été dactylographiées à l'aide d'un ruban usé ou si l'université nous a fait parvenir une photocopie de qualité inférieure.

La reproduction, même partielle, de cette microforme est soumise à la Loi canadienne sur le droit d'auteur, SRC 1970, c. C-30, et ses amendements subséquents.

Theoretical and Experimental Investigation of Converging
Cylindrical Shock Waves Propagating in
Narrow Cylindrical Chambers

Gley Zitouni

A Thesis

in

The Department

of

Mechanical Engineering

Presented in Partial Fulfilment of the Requirements
for the Degree of
Master of Applied Science at
Concordia University
Montreal, Québec, Canada

September 1992

© Gley Zitouni, 1992



National Library
of Canada

Acquisitions and
Bibliographic Services Branch

395 Wellington Street
Ottawa, Ontario
K1A 0N4

Bibliothèque nationale
du Canada

Direction des acquisitions et
des services bibliographiques

395, rue Wellington
Ottawa (Ontario)
K1A 0N4

Author's Acknowledgement

Autre reconnaissance

The author has granted an irrevocable non-exclusive licence allowing the National Library of Canada to reproduce, loan, distribute or sell copies of his/her thesis by any means and in any form or format, making this thesis available to interested persons.

L'auteur a accordé une licence irrévocable et non exclusive permettant à la Bibliothèque nationale du Canada de reproduire, prêter, distribuer ou vendre des copies de sa thèse de quelque manière et sous quelque forme que ce soit pour mettre des exemplaires de cette thèse à la disposition des personnes intéressées.

The author retains ownership of the copyright in his/her thesis. Neither the thesis nor substantial extracts from it may be printed or otherwise reproduced without his/her permission.

L'auteur conserve la propriété du droit d'auteur qui protège sa thèse. Ni la thèse ni des extraits substantiels de celle-ci ne doivent être imprimés ou autrement reproduits sans son autorisation.

ISBN 0-315-84694-1

Canada

ABSTRACT

Theoretical and Experimental Investigation of Converging Cylindrical Shock Waves Propagating in Narrow Cylindrical Chambers

Gley Zitouni

The propagation and stability of converging cylindrical shocks, produced in an annular shock tube, equipped with a three increment area contraction, was investigated for various cylindrical chamber widths and two annular shock Mach numbers of 1.26 and 1.44.

The Method of Characteristics, integrated using the Hartree scheme, was employed to determine the shock Mach number and pressure-time variations in the cylindrical chamber. These numerical values were verified experimentally by employing a set of piezoelectric pressure transducers placed at five different locations. In narrow cylindrical chambers, a new test section was employed to determine boundary layer effect on the shock strength. For a cylindrical chamber width of 2.5 *mm*, experimental results were found in excellent agreement with the inviscid numerical solution. For smaller widths, an empirical equation of the shock Mach number variation was developed. Stability of the converging shocks was examined from the series of spark shadowgraphs taken near the geometric centre.

ACKNOWLEDGEMENTS

The author would like to express his greatest gratitude to his supervisor Dr. R. A. Neemeh for his continued support and encouragement throughout the course of investigation. Extended thanks go to Miss Laura Neemeh for her helpful suggestions in the improvement of the text.

This work was supported by the National Sciences and Engineering Research Council under Grant No. O.G.P.D.D.D. 4206

TABLE OF CONTENTS

LIST OF FIGURES	vii
NOMENCLATURE	x
CHAPTER 1: INTRODUCTION	1
CHAPTER 2: THEORETICAL DEVELOPMENT	6
2.1 Method of Characteristics	6
2.2 Computational Method	11
2.3 General Point	14
2.4 Shock Point	17
2.4.1 Converging Shock	17
2.4.2 Diverging Shock	20
2.5 Flow Near The Axis	22
2.6 Implosion Chamber Inlet	23
2.7 General Remarks About The Computational Procedure	25
CHAPTER 3: EXPERIMENTAL SET UP AND PROCEDURE	27
3.1 Shock Tube	27
3.2 Upstream of the Test Section	28
3.3 Test Section	29
3.4 The Schlieren System	30
3.5 Experimental Procedure	31
CHAPTER 4: RESULTS AND DISCUSSION	35
4.1 Pressure and Shock Mach Number Measurements	35
4.2 Narrow Cylindrical Chamber Width	39
4.2.1 Experimental observations	39
4.2.2 Theoretical Formulation	43
4.3 Stability Analysis	45

4.3.1 Amplification	48
4.3.2 The Collapse Mechanism	50
CHAPTER 5: CONCLUSION AND RECOMMENDATIONS	52
5.1 Conclusion	52
5.2 Future Work	54
REFERENCES	55

LIST OF FIGURES

FIGURE:

2.1	The general solution of the characteristics method	59
2.2	The computational solution of the characteristics method	59
2.3	The characteristics method for a subsonic flow	60
2.4	The characteristics method for a supersonic flow	60
2.5	The characteristics method solution for converging shock points	61
2.6	The characteristics method solution for diverging shock points	61
2.7	The characteristics method solution for flow points at the test section inlet	62
2.8	The characteristics method computational solution for flow points near the axis	62
3.1	A schematic diagram of the experimental set up	63
3.2	A schematic diagram of the plunger mechanism	64
3.3	Upstream of the test section	65
3.4	Sectional view of the flange	66
3.5	Sectional view of the downstream end of the shock tube	67
3.6	A schematic diagram of the test section (original model)	68
3.7	A schematic diagram of the test section (new model)	69
3.8	A schematic diagram of the schlieren photography system	70

4.1	Oscilloscope traces for $M_o=1.44$ and $M_o=1.26$ with $W=2.5$ mm	74
4.2	Shock Mach number variation for $M_o=1.44$ and $W=2.5$ mm	75
4.3	Shock Mach number variation for $M_o=1.26$ and $W=2.5$ mm	76
4.4	Shock Mach number versus radius for $M_o=1.44$ in log-log scale	77
4.5	Oscilloscope traces for $M_o=1.44$, $R=24.13$ mm, 13.87 mm, 8.89 mm and 3.81 mm, $W=0.6$ mm and 0.3 mm	81
4.6	Pressure history for $M_o=1.44$, $W=2.5$ mm and $R=24.13$ mm,...	82
4.7	Pressure history for $M_o=1.44$, $W=0.6$ mm and $R=24.13$ mm,...	83
4.8	Pressure history for $M_o=1.44$, $W=0.3$ mm and $R=24.13$ mm,...	84
4.9	Pressure history for $M_o=1.44$, $W=2.5$ mm and $R=13.87$ mm,...	85
4.10	Pressure history for $M_o=1.44$, $W=0.6$ mm and $R=13.87$ mm,...	86
4.11	Pressure history for $M_o=1.44$, $W=0.3$ mm and $R=13.87$ mm,...	87
4.12	Pressure history for $M_o=1.44$, $W=2.5$ mm and $R=8.89$ mm,...	88
4.13	Pressure history for $M_o=1.44$, $W=0.6$ mm and $R=8.89$ mm,...	89
4.14	Pressure history for $M_o=1.44$, $W=0.3$ mm and $R=8.89$ mm,...	90
4.15	Pressure history for $M_o=1.44$, $W=2.5$ mm and $R=3.81$ mm,...	91
4.16	Pressure history for $M_o=1.44$, $W=0.6$ mm and $R=3.81$ mm,...	92
4.17	Pressure history for $M_o=1.26$, $W=2.5$ mm and $R=24.13$ mm,...	93
4.18	Pressure history for $M_o=1.26$, $W=0.3$ mm and $R=24.13$ mm,...	94
4.19	Pressure history for $M_o=1.26$, $W=2.5$ mm and $R=13.87$ mm,...	95
4.20	Pressure history for $M_o=1.26$, $W=0.3$ mm and $R=13.87$ mm,...	96
4.21	Pressure history for $M_o=1.26$, $W=2.5$ mm and $R=8.89$ mm,...	97

4.22	Pressure history for $M_o=1.26$, $W=0.3\text{ mm}$ and $R= 8.89\text{ mm},...$	98
4.23	Mach number variation for $M_o=1.44$ with $W=2.5\text{ mm}$, 0.6 mm and 0.3 mm	99
4.24	Mach number variation for $M_o=1.26$ with $W=2.5\text{ mm}$, 0.6 mm and $0.3\text{ mm}...$	100
4.25	Perturbation rate, the experimental results were compared with Butler's small perturbation analysis	101
4.26	Oscilloscope traces for $M_o=1.26$, $R=24.13\text{ mm}$, 13.87 mm , 8.89 mm and 3.81 mm , $W=0.6\text{ mm}$ and 0.3 mm	105
4.27	Spark shadowgraphs illustrating the propagation of cylindrical shock wave in a narrow cylindrical chamber for $M_o=1.26$ and $W=0.6\text{ mm}$	106
4.28	Spark shadowgraphs illustrating the propagation of cylindrical shock wave in a narrow cylindrical chamber for $M_o=1.26$ and $W=0.3\text{ mm}$	107
4.29	Spark shadowgraphs illustrating the propagation of cylindrical shock wave in a narrow cylindrical chamber for $M_o=1.26$ and $W=2.5\text{ mm}$	109
4.30	Rate of perturbation of the converging cylindrical shock for $M_o=1.26$	110
4.31	Spark schlieren photographs of plane shock reflection from a semi-circular end wall, $M_s=2.2$	111

NOMENCLATURE

Latin Symbols

a	Speed of sound
C^+	Positive characteristics
C^-	Negative characteristics
C°	Particle path characteristics
D	Major diameter of the shock front
d	Minor diameter of the shock front
K	Coefficient found experimentally (equation (4.7))
M	Mach number
M_o	Annular shock Mach number
M_s	Cylindrical shock Mach number
M_{sp}	Plane shock Mach number
n	Amplification exponent
P	Fluid pressure
p	fluid pressure in Log form
p_1	Driven chamber pressure
p_2	Driver chamber pressure
R_o	Distance between the outer edge of cylindrical chamber and the centre
R_s	Shock radius
s	Specific entropy

S	Cross section area
t	Time
T	Temperature
u	fluid velocity
x	x-coordinate

Greek Symbols

γ	Isentropic gas constant
ϵ	Distance between the centre and the last point on the data line
λ	Mesh ratio
ξ	Perturbation parameter
ρ	Density
σ	Courant number

CHAPTER 1

INTRODUCTION

The focussing of spherical and cylindrical shock waves has been used for various engineering and scientific applications. It is an effective and economic means of producing high temperature and pressure gas at the implosion centre. For instance, converging shock waves process has been successfully adopted in the production of high temperature and density plasmas [1], synthetic diamonds from graphite carbide and neutrons [2]. Moreover, they are used in research related to particles launched at hypersonic velocity. They are also associated with research related to substance behaviour under severe conditions in a high energy medium [3].

For over three decades, converging shock waves production and analysis has been the focus of numerous experimental and theoretical studies. Perry and Kantrowitz [4,5] were the pacesetters for the production of converging cylindrical shock waves. They used a conical shape known as *teardrop* configuration. Their set up consisted of a cylindrical shock tube having an axisymmetric tear drop shaped inner core used to transform a plane shock wave into a cylindrical shock one. Based on the same principle, converging shock detonation wave was investigated experimentally by Knystaus *et al.* [6] and Takayama *et al.* [7,8]. Wu *et al.* [9] and Neemeh *et al.* [10], however, used a three increment area arrangement. Shock waves produced using this method were proven to be highly

symmetric in shape. Apart from these methods, Matsuo *et al.* [11] produced cylindrically converging waves using explosive shells. Here, shock strength is controlled by the amount of explosives. Parameters related to shock propagation were determined by employing an electrical ionization probing mechanism.

Analytically, Guderley [12] was the first to present a comprehensive investigation involving cylindrical and spherical shock wave propagation in air and he obtained a similarity solution. In his solution shock strength was found to be proportional to R^{-n} , R being the distance from the centre of implosion and n a constant that depends on the specific heat ratio γ . This model clearly implies that theoretically a converging shock wave can increase in strength indefinitely as the radius R approaches zero. In practice, at the centre of implosion, temperature and pressure can attain very high but finite values due to experimental limitations. Based on Guderley's theory many investigators focused their effort on the development of similarity solutions for the converging process. Among these we find Butler [13] and Stanyukovich [14]. Since the above principle was based on strong shock assumption, it is considered an adequate description of the shock motion at the vicinity of the centre where shock Mach number is very high. Other investigators have attempted to provide approximate solution to shock propagation away from the point of collapse. Chester [15,16,17] treated the problem by considering a shock wave moving through a small area change and using small perturbation theory he derived a Mach-area relationship. Based on the same principle but with different assumptions, Chisnell [18] developed a more general first-order relationship between change in area

and shock strength. Later, Whitham [19], adopting a completely different approach, derived a Mach-area relationship using the characteristics set of equations. Chester, Chisnell and Whitham relation, known as the CCW theory, describes the effect of the change in area on the shock dynamics. Surprisingly, the CCW theory was found to give excellent results when compared with the experimental values.

Simple physical argument, analytical [20] and numerical [21] treatments confirm the general prediction that converging shocks ought to be unstable. Stability of converging shock waves is an important factor for the understanding of the imploding mechanism. The final state of gas at the centre of implosion depends directly on the degree of symmetry of the converging shock wave. Conventionally, the degree of symmetry is a scale by which stability can be measured. In other words, a converging shock wave is said to be stable if it is unsensitive to the external perturbations as well as those within the flow domain. Based on this principle Ahmad [22] investigated the stability of converging cylindrical shock wave through the interaction of the converging shock with cylindrical rods of different diameters. He noticed a shift in the collapse point from the geometrical centre, in all cases, indicating shock instability. Earlier, Wu *et al.* [23] studied the stability of converging shocks perturbed by a small circular aperture in the shock tube and found a similar degree of instability as they progressed towards the centre. In recent experiments Watanabe and Takayama [24] have shown that initial perturbations caused by the supports of the annular section of the shock tube grew with shock propagation, resulting in early onset of shock instability. The theoretical work of Butler

[13] and Whitham [19] gave a comprehensive investigation of imploding shock stability. This analysis shows that converging shocks are unstable and for perturbed shocks the perturbation increases with R according to the relation $\xi \propto R^{-5/2}$. However, their analysis was limited to very strong converging shocks and the use of the CCW Area-Mach number shock propagation law.

An important factor that influence the converging shock propagation is the cylindrical chamber configuration at the end of the shock tube. Any modification in the cylindrical chamber width involves changes in the upstream conditions. Since the CCW area-Mach number relation was based on uniform upstream conditions, it is not evident that the produced converging shocks would follow a specific propagation law. Narrow cylindrical chambers result in shock attenuation due to the boundary layer and produces a complex flow field in the pre-shock region. However, large cylindrical chamber width is associated with multiple lateral reflections of the imploding shock. The scope of this thesis was, therefore, to examine experimentally the converging cylindrical shocks produced by the present apparatus. The experiments consist of pressure measurements to determine the shock strength and pressure time variation at different radii. The effect of the cylindrical chamber gap on the law of shock propagation will also be investigated. Exact solution to this problem will be numerically obtained by the method of characteristics. Assuming inviscid flow, the solution will be compared with the experimental results to judge whether the produced cylindrical shock is following any shock propagation law and to determine the minimum cylindrical width below which

boundary layer becomes significant. Due to the difficulties in isolating the effect of the upstream conditions from those due to the boundary layer in the original model, a new one is designed to remedy this problem.

In chapter 2, the details of the computational method used is outlined. The description of the experimental set up including the new design is given in chapter 3. A detailed discussion of the experimental results vis-a-vis the computational and the theoretical ones is presented in chapter 4. A comprehensive analysis of shock propagation is outlined through the interpretation of the pressure measurements and the different sets of the schlieren photographs obtained near the geometric centre. In chapter 5, the conclusion drawn from this thesis work is presented along with future progress.

CHAPTER 2

THEORETICAL DEVELOPMENT

1.1. Method Of Characteristics

The unsteady compressible form of the Navier-Stokes equation is a set of nonlinear partial differential equations that describe completely the fluid flow. However, the fact that these equations are nonlinear, analytical solutions are not possible without adequate simplifications. Although, the linearization of these equations provides approximation solutions, it is not without loss of accuracy. At a supersonic speed the flow witnesses the presence of wave-like discontinuities with well defined direction of propagation, known as Mach Waves. The determination of these Mach Waves or characteristics is the technique on which the solution of supersonic flow problems depends. The propagation of these waves can be represented in a wave diagram which can be constructed using the method of characteristics. In spite of its complexity, when it comes to multi-dimensional flow field, it still retains a considerable advantage over the other numerical methods when dealing with many unsteady one dimensional flow problems, which is our case. It provides simple, exact and adequate means of analyzing the propagation of converging (diverging) shocks, as well as the determination of fluid properties at a given point in space and time.

In the absence of body forces and neglecting gravitational effect, the one-

dimensional time-dependent compressible flow can be represented by the following set of equations [25].

$$\frac{\partial \rho}{\partial t} + u \frac{\partial \rho}{\partial x} + \rho \frac{\partial u}{\partial x} = -\rho \frac{u}{S} \frac{\partial S}{\partial x} \quad (2.1)$$

$$\frac{\partial u}{\partial t} + u \frac{\partial u}{\partial x} + \frac{1}{\rho} \frac{\partial P}{\partial x} = 0 \quad (2.2)$$

where ρ , u , p and S are the density, particle velocity, pressure and cross section area, respectively.

If we assume that each particle in the flow maintains a constant entropy along its path we have

$$\frac{\partial s}{\partial t} + u \frac{\partial s}{\partial x} = 0 \quad (2.3)$$

where s is defined as

$$s = c_v \ln \left(\frac{P}{\rho^\gamma} \right) + \text{const} \quad (2.4)$$

by differentiating equation (2.4) and using equation (2.3) we get

$$\frac{\partial P}{\partial t} + u \frac{\partial P}{\partial x} = \frac{\gamma P}{\rho} \left(\frac{\partial \rho}{\partial t} + u \frac{\partial \rho}{\partial x} \right) \quad (2.5)$$

The local speed of sound is defined by

$$a = \sqrt{\frac{\gamma P}{\rho}} \quad (2.6)$$

Multiplying equation (2.1) by a^2 and using equation (2.5) we get

$$\frac{\partial P}{\partial t} + u \frac{\partial P}{\partial x} + \rho a^2 \frac{\partial u}{\partial x} = -\frac{\rho u a^2}{S} \frac{\partial S}{\partial x} \quad (2.7)$$

Multiplying equation (2.2) by ρa we obtain the following:

$$\rho a \frac{\partial u}{\partial t} + \rho a u \frac{\partial u}{\partial x} + a \frac{\partial P}{\partial x} = 0 \quad (2.8)$$

Adding and then subtracting equations (2.7) and (2.8) we get

$$\frac{\partial P}{\partial t} + (u+a) \frac{\partial P}{\partial x} + \rho a \left[\frac{\partial u}{\partial t} + (u+a) \frac{\partial u}{\partial x} \right] = - \frac{\rho u a^2}{S} \frac{\partial S}{\partial x} \quad (2.9)$$

Dividing equation (2.9) by ρa and using equation (2.6) to eliminate the density term we get

$$\frac{a}{\gamma P} \left[\frac{\partial P}{\partial t} + (u+a) \frac{\partial P}{\partial x} \right] + \left[\frac{\partial u}{\partial t} + (u+a) \frac{\partial u}{\partial x} \right] = - \frac{ua}{S} \frac{\partial S}{\partial x} \quad (2.10)$$

since

$$\frac{1}{P} \frac{\partial P}{\partial t} = \frac{\partial \ln P}{\partial t}$$

and

$$\frac{1}{P} \frac{\partial P}{\partial x} = \frac{\partial \ln P}{\partial x}$$

equation (2.10) becomes

$$\frac{a}{\gamma} \left[\frac{\partial \ln P}{\partial t} + (u+a) \frac{\partial \ln P}{\partial x} \right] + \left[\frac{\partial u}{\partial t} + (u+a) \frac{\partial u}{\partial x} \right] = - \frac{ua}{S} \frac{\partial S}{\partial x} \quad (2.11)$$

the quantities between brackets in equation (2.11) represent the substantial derivatives of

$\ln P$ and u in the x, t plane such that

$$\frac{dx}{dt} = u+a$$

If we define

then equation (2.11) becomes

$$\frac{d^+}{dt} = \frac{\partial}{\partial t} + (u+a) \frac{\partial}{\partial x} \quad \text{along } C^+ \text{ curves}$$

$$\frac{d^-}{dt} = \frac{\partial}{\partial t} + (u-a) \frac{\partial}{\partial x} \quad \text{along } C^- \text{ curves}$$

$$\frac{a}{\gamma} \frac{d^+ \ln(P)}{dt} + \frac{d^+ u}{dt} = - \frac{au}{S} \frac{\partial S}{\partial x} \quad (2.12)$$

$$\frac{a}{\gamma} \frac{d^- \ln(P)}{dt} - \frac{d^- u}{dt} = - \frac{au}{S} \frac{\partial S}{\partial x} \quad (2.13)$$

Hereafter, the term $\ln P$ will be replaced by p for simplicity.

Furthermore, equations (2.12) and (2.13) can be non-dimensionalized using the following transformations:

$$x' = \frac{x}{R_0}$$

$$u' = \frac{u}{\sqrt{RT_0}}$$

$$a' = \frac{a}{\sqrt{RT_0}}$$

$$t' = \frac{t}{\frac{R_0}{\sqrt{RT_0}}}$$

$$p' = \ln P' = \ln P - \ln P_0$$

where R_0 is the implosion chamber radius, T_0 the ambient temperature and P_0 is initial pressure at the driven section of the shock tube.

Then we have

$$\frac{a'}{\gamma} \frac{d^+P'}{dt'} + \frac{d^+u'}{dt'} = -\frac{a'u'}{S} \frac{\partial S}{\partial x'}$$

$$\frac{a'}{\gamma} \frac{d^-P'}{dt'} - \frac{d^-u'}{dt'} = -\frac{a'u'}{S} \frac{\partial S}{\partial x'}$$

It is more convenient to omit the primes and use equations (2.12) and (2.13) in non-dimensionalised form.

Equations (2.12) and (2.13) are known as the compatibility relations. They describe the behaviour of the different physical quantities along the characteristics. The characteristics are curves in $x-t$ plane whose inverse slope are $u+a$ and $u-a$. In a physical sense $u+a$ and $u-a$ are the speeds by which these waves, carrying information related to flow properties, pressure, density and velocity, propagate within the flow field. Equation (2.3) define a third characteristic direction which is the particle path.

In conclusion the method of characteristics is defined by the following three terms:

1. The characteristics speeds by which waves carry information about the physical quantities travel within the flow namely, $u+a$, $u-a$ and u .
2. Compatibility relations which are given in equations (2.12), (2.13) and (2.3). They represent the behaviour of the physical quantities along the characteristics.
3. Domain of dependence which is defined by the area ABP in figure 2.1. Any disturbance of the initial data outside of this section does not influence the solution

at point P .

2.2. The Computational Method

In general, the method of characteristics gives the most accurate solution for hyperbolic systems because it represents the physical nature of the flow. It is probably the most convenient method for solving flows involving discontinuities. Although, the characteristics equations are full description of the flow behaviour they are still nonlinear because the speeds of propagation vary from point to point. However, if we assume that $u+a$, $u-a$ and u are frozen within the time interval Δt the physical quantities can be convected in a wave-like way, unchanged and with constant speeds, at a local scale. In an axially symmetric case the solution is affected only by the change of area presented in the *RHS* of equations (2.12) and (2.13).

The *RHS* is defined as a source term given by

$$RHS = -\frac{au}{S} \frac{\partial S}{\partial x} \quad (2.14)$$

For a cylindrical wave the cross section area is proportional to the radius x , then we have

$$RHS = -\frac{au}{x} \quad (2.15)$$

The characteristics curves become straight lines in the $x-t$ plane with inverse slopes u , $u-a$ and $u+a$. The general characteristics solution can be summarized in figure(2.1). Through a point P we can draw three characteristics namely C^* , C and C' . The solution at point P depends on the initial data line $n\Delta t$ that the three characteristics C^* , C and C' intersect

at points A , B and C , respectively. These points are determined by interpolation along the initial data line. The accuracy of this method depends on the accuracy of the interpolation procedure as well as the choice of the mesh ratio $\Delta t/\Delta x$. If we define the grid coordinates in x - t plane by:

$$x(j\Delta x, n\Delta t) = x_j^n \quad (2.16)$$

Hence;

$$p(j\Delta x, n\Delta t) = p_j^n \quad (2.17)$$

$$u(j\Delta x, n\Delta t) = u_j^n \quad (2.18)$$

$$a(j\Delta x, n\Delta t) = a_j^n \quad (2.19)$$

Then from figure (2.1) we get

$$x(A) = x_j^n + (u+a) \Delta t \quad (2.20)$$

$$x(B) = x_j^n + (u-a) \Delta t \quad (2.21)$$

$$x(C) = x_j^n + u \Delta t \quad (2.22)$$

but

$$x_j^n = j\Delta x \quad (2.23)$$

Then if we define the mesh ratio

$$\lambda = \frac{\Delta t}{\Delta x} \quad (2.24)$$

We get

$$x(A) = (j + \lambda(u+a)) \Delta x \quad (2.25)$$

$$x(B) = (j + \lambda(u-a)) \Delta x \quad (2.26)$$

$$x(C) = (j + \lambda u) \Delta x \quad (2.27)$$

Define the Courant numbers as:

$$\sigma_1 = \lambda(u+a) \quad (2.28)$$

$$\sigma_2 = \lambda(u-a) \quad (2.29)$$

$$\sigma_0 = \lambda u \quad (2.30)$$

It has been proved that the characteristics method yields a stable solution if the mesh ratio λ is less than the slope of the characteristics in $x-t$ plane. This criteria for stability was obtained by Courant *et al.* [26], known as the *CFL* condition, and it is given by:

$$\lambda \leq \frac{1}{|u|+a} \quad (2.31)$$

Or in term of Courant number

$$(2.32) \quad |\sigma_i| \leq 1.0, \quad i = 0, 1, 2$$

The compatibility relations can be solved by the following numerical approximations:

$$\overline{a_1} [p_j^{n+1} - p(A)] + [u_j^{n+1} - u(A)] = -2\overline{a_1} \overline{u_1} \frac{\Delta t}{x_j^{n+1} + x(A)} \quad (2.33)$$

$$\overline{a}_2 [p_j^{n+1} - p(B)] - [u_j^{n+1} - u(B)] = -2\overline{a}_2 \overline{u}_2 \frac{\Delta t}{x_j^{n+1} + x(B)} \quad (2.34)$$

$$s_j^{n+1} = s(C) \quad (2.35)$$

where

$$\overline{u}_1 = \frac{u_j^{n+1} + u(A)}{2}, \quad \overline{a}_1 = \frac{a_j^{n+1} + a(A)}{2}$$

and

$$\overline{u}_2 = \frac{u_j^{n+1} + u(B)}{2}, \quad \overline{a}_2 = \frac{a_j^{n+1} + a(B)}{2}$$

2.3. General Point

For a general point the quantities at A , B and C are determined by linear interpolation between two known nodal points. From the stability criteria established above, these intersection points are interpolated for in the interval $[j, j+1]$ for negative characteristics slopes and in the interval $[j-1, j]$ for positive ones. The two different cases are presented as follow:

i) Subsonic flow

From figure 2.3 the flow properties at points A and B can be approximated as follow:

$$u_A = \lambda |u \pm a| [u_{j+1}^n - u_j^n] + u_j^n$$

$$a_A = \lambda |u \pm a| [a_{j+1}^n - a_j^n] + a_j^n$$

$$p_A = \lambda |u \pm a| [p_{j+1}^n - p_j^n] + p_j^n$$

ii) Supersonic flow

This case is presented in figure 2.4.

$$u_A = \lambda |u \pm a| [u_{j-1}^n - u_j^n] + u_j^n$$

$$a_A = \lambda |u \pm a| [a_{j-1}^n - a_j^n] + a_j^n$$

$$p_A = \lambda |u \pm a| [p_{j-1}^n - p_j^n] + p_j^n$$

To deal with this directivity problem many schemes have been constructed in order to establish an automatic direction switching. Among these we find Reo [27] and Moretti [28]. The above system of equations can be put in more compact form using Courant-Issacon-Rees linear interpolation formula [29] given by

$$u_A = \lambda (u^- [u_{j+1}^n - u_j^n] + u^+ [u_{j-1}^n - u_j^n]) + u_j^n \quad (2.36)$$

$$a_A = \lambda (u^- [a_{j+1}^n - a_j^n] + u^+ [a_{j-1}^n - a_j^n]) + a_j^n \quad (2.37)$$

$$p_A = \lambda (u^- [p_{j+1}^n - p_j^n] + u^+ [p_{j-1}^n - p_j^n]) + p_j^n \quad (2.38)$$

where,

$$u^+ = \frac{(\overline{u_{1,2}} \pm \overline{a_{1,2}}) + \left| \overline{u_{1,2}} \pm \overline{a_{1,2}} \right|}{2}$$

and

$$u^- = \frac{(\overline{u_{1,2}} \pm \overline{a_{1,2}}) - \left| \overline{u_{1,2}} \pm \overline{a_{1,2}} \right|}{2}$$

At point C we only need to interpolate for the entropy s and flow speed u . The latter property is employed to relocate C on the initial data line. The following scheme is used:

$$u(C) = \lambda(v^- [u_{j+1}^n - u_j^n] + v^+ [u_{j-1}^n - u_j^n]) + u_j^n \quad (2.39)$$

$$s_j^{n+1} = s(C) = \lambda(v^- [s_{j+1}^n - s_j^n] + v^+ [s_{j-1}^n - s_j^n]) + s_j^n \quad (2.40)$$

where

$$v^+ = \frac{\overline{u_o} + \left| \overline{u_o} \right|}{2}$$

$$v^- = \frac{\overline{u_o} - \left| \overline{u_o} \right|}{2}$$

and

$$\overline{u_o} = \frac{u(C) + u_j^{n+1}}{2}$$

Since the solution depends only on the slopes of the characteristics the values of u and

a at point P are initially set equal to u_j^n and a_j^n . Once provisional values of the flow quantities at P are computed, they can be used to calculate new values using the characteristics relations.

$$p_j^{n+1} = \frac{\gamma}{\overline{a_1} + \overline{a_2}} (u(A) - u(B) + \overline{a_1} \frac{P(A)}{\gamma} + \overline{a_2} \frac{P(B)}{\gamma} + 2\Delta t (\frac{\overline{a_2} u_2}{x(B) + x_j^n} + \frac{\overline{a_1} u_1}{x(A) + x_j^n}))$$

$$u_j^{n+1} = u(A) - \frac{\overline{a_1}}{\gamma} (p_j^{n+1} - P(A)) - \frac{2\overline{a_1} u_1 \Delta t}{x(A) + x_j^n}$$

$$\rho_j^{n+1} = e^{\frac{p_j^{n+1} - p_j^{n+1}}{\gamma}}$$

$$a_j^{n+1} = \sqrt{\frac{\gamma}{\rho_j^{n+1}}} e^{p_j^{n+1}}$$

2.4. Shock Point

2.4.1. Converging Shock

The fluid ahead of the converging shock is at rest ($u=0$) and assumed isentropic. The flow properties are all known and constant. However, quantities behind the shock are function of time t and the radius x , they are determined numerically by shock fitting technique. In addition to the information provided by the compatibility relation along the characteristics an additional relation should be introduced to express the sudden change (jump) in properties across the shock. This jump condition is presented in the form of Hugoniot equations [30] which are derived from the conservation laws of mass, energy and momentum.

$$p_r = \frac{2\gamma M_s^2 - (\gamma - 1)}{\gamma + 1}$$

$$\rho_r = \frac{(\gamma + 1)M_s^2}{(\gamma - 1)M_s^2 + 2}$$

where p_r and ρ_r are pressure and density ratio across the shock, respectively.

$$p_1' = \ln(p_r) + \ln(P_o)$$

$$\rho_1' = \ln(\rho_r) + \ln(\rho_o)$$

$$a_1' = \frac{a_o}{\sqrt{\frac{\rho_r}{p_r}}}$$

$$s_1' = s_o + \ln(p_r) - \gamma \ln(\rho_r)$$

$$u_1' = \frac{2a_o}{\gamma + 1} \left(M_s - \frac{1}{M_s} \right)$$

where ρ_1' , p_1' , a_1' and s_1' are density, pressure, local speed of sound and entropy, respectively, behind the shock, expressed in term of the shock Mach number M_s and the undisturbed flow quantities ahead of it. To express the influence on the shock of the flow behind it, a right moving wave is needed. The remaining other two characteristics originate from points on the shock and propagate into the flow with u and $u-a$. The left moving wave (propagating with $u-a$) counteracts with the right moving characteristics (propagating with $u+a$) and distort them creating a complex and highly nonlinear fluid

flow. This explains how the shock adjust not only to change in the medium geometry ,namely the radius x , but also to the nonlinear interaction with the flow behind it. The computational procedure which is shown in figure 2.5 can be summarized in the following steps:

1. Assume a shock Mach number M_s , then use the Rankine-Hugoniot equations given above to calculate the flow properties at point P downstream of the converging shock.
2. Calculate shock displacement Δx_s and determine the location of point P at time $(n+1) \Delta t$ in $x-t$ plane using the following relation:

$$\Delta x_s = \frac{M_s + M_j^n}{2} a_o \Delta t$$

3. From point P with a slope

$$\bar{u} = \frac{(u(A) + a(A) + u(P) + a(P))}{2}$$

determine the location of point A on the initial data line $n\Delta t$

$$x(A) = x_j^n - \Delta x_s + \bar{u} \Delta t$$

4. Knowing the location of point A it is then interpolated for between the nodal points j and $j-1$.
5. A provisional pressure value is then calculated using compatibility relation along characteristics.

$$p(P) = p(A) + \frac{\gamma}{a_1} \left[u(A) - u_1 + \frac{2\overline{u_1 a_1} \Delta t}{x(A) + x_s} \right]$$

where

$$x_s = \Delta x_s + x_j^n$$

6. Substitute the pressure value obtained in step 5 into Rankine-Hugoniot equation to calculate a new Mach number. If the new calculated Mach number is different from the assumed one the procedure is repeated until an exact solution is obtained.

2.4.2. Diverging Shock

Unlike the converging shock, the diverging shock wave is moving into a medium with unknown quantities. Figure 2.6 shows the general computation method for this case. AP is a left moving wave, namely, C characteristics. It expresses the effect of the disturbed flow on the diverging shock. Ahead of the shock the three characteristics are needed to compute the unknown quantities. The procedure is similar to that of general point except the solution should satisfy a variable boundary condition created by the presence of the shock. The following is a brief summary of the solution procedure.

1. Calculate shock displacement Δx_s and determine the location of point P at time $(n+1)\Delta t$ in the $x-t$ plane using the following relation:

$$\Delta x_s = (M_j^n a_j^n - u_j^n) \Delta t$$

here, a_j^n and u_j^n are sound speed and flow velocity ahead of the diverging shock at time $n\Delta t$, respectively.

2. Use the general point algorithm to determine the flow properties ahead of the diverging shock at point P .
3. Assume a shock Mach number M_s , then use the Rankine-Hugoniot equations to calculate the flow properties at point P behind diverging shock.
4. From point P with a slope

$$\bar{u} = \frac{(u(A) + a(A) + u(P) + a(P))}{2}$$

determine the location of point A on the initial data line; $n\Delta t$.

$$x(A) = x_j^n + \Delta x_s - \bar{u}\Delta t$$

5. Knowing the location of point A it is then interpolated for between the nodal points j and $j+1$.
6. Calculate pressure at point P using the compatibility relation along the characteristics line AP .

$$p(P) = p(A) + \frac{\gamma}{a_1} \left[u(A) - u_1 - \frac{2\bar{u}_1 a_1 \Delta t}{x(A) + x_s} \right]$$

where

$$x_s = \Delta x_s + x_j^n$$

7. Substitute the pressure value obtained in step 6 into Rankine-Hugoniot equation to calculate a new Mach number. If the difference between the new calculated Mach number and the assumed one is not within a preset error repeat steps 2 to 7 with

$$\Delta x_s = \left(\frac{M_s + M_j^n}{2} a(P) - u(P) \right) \Delta t$$

2.5. Flow Near The Axis

At the centre of the implosion chamber the source term in the compatibility relations is indeterminate as the radius x goes to zero. To overcome this singularity the incident shock reflection is assumed to take place at a small distance from the centre. Then, at the vicinity of the centre we have, $x = \epsilon$ and $u = 0$. The numerical solution is illustrated schematically in figure 2.8.

1. The values of the flow quantities at C and A are first set equal to those of point $(I, n\Delta t)$.
2. A pressure value at point P is initially guessed
3. Following the particle path the position of C is obtained using the following relation:

$$x(C) = \epsilon + |u(C)| \Delta t$$

$$u(C) = \lambda \overline{u_o} [u_\epsilon^n - u_{m-1}^n] + u_{m-1}^n$$

4. Calculate the flow properties at point C by interpolating between point ϵ and $m-1$.

$$a(C) = \lambda \overline{u_o} [a_\epsilon^n - a_{m-1}^n] + a_{m-1}^n$$

$$p(C) = \lambda \overline{u_o} [p_\epsilon^n - p_{m-1}^n] + p_{m-1}^n$$

Since the flow is isentropic along the particle path we have:

$$s_{\epsilon}^{n+1} = s(C) = \lambda \overline{u_1} [s_{\epsilon}^n - s_{m-1}^n] + s_{m-1}^n$$

and

$$a_1^{n+1} = a(C) e^{\frac{(\gamma-1)(p_{m-1}^{n+1} - p(C))}{2\gamma}}$$

5. The position of point A is obtained using the following relation

$$\tau(C) = \varepsilon + |\overline{u_1}| \Delta t$$

6. Again the quantities at point A are obtained by linear interpolation between points ϵ and $m-1$

$$u(A) = \lambda |\overline{u_1}| [u_{\epsilon}^n - u_{m-1}^n] + u_{m-1}^n$$

$$a(A) = \lambda |\overline{u_1}| [a_{\epsilon}^n - a_{m-1}^n] + a_{m-1}^n$$

$$p(A) = \lambda |\overline{u_1}| [p_{\epsilon}^n - p_{m-1}^n] + p_{m-1}^n$$

where

$$|\overline{u_1}| = \frac{|u(A) - a(A) - a(P)|}{2}$$

7. Using the relation along C a new value of p is calculated, it is compared to the initially guessed value.

8. If the difference between the old and the new value is greater than the preset error, a new value is then assumed.

2.6. Implosion Chamber Inlet

At the inlet of the implosion chamber isentropic and uniform conditions were throughout this flow domain. Constant C^* characteristics were therefore assumed at the inlet which together with the reflected C^- waves upstream give the flow properties at the open end.

The above assumption can be represented by the following relation:

$$u(P) + \frac{2}{\gamma-1} a(P) = u^o + \frac{2}{\gamma-1} a^o$$

$$a(P) + u(P) = a^o + u^o$$

Here, a^o and u^o are speed of sound and flow velocity at time $t=0$ and $x=0$, respectively.

The computational solution is illustrated in figure 2.7. The following algorithm is adopted to obtain the different flow properties.

1. Assume a pressure value at point P and set the remaining flow properties at point P equal to those of point 1.
2. Determine $u(P)$ and $a(P)$ from the above system of equations and obtain the location of point A using the following equation:

$$\Delta x = \frac{|u(A) - a(A) + u(P) - a(P)|}{2}$$

3. Determine flow properties at point A by interpolating along the line $n\Delta t$.
4. Calculate the pressure $p(A)$ using the following compatibility relation:

$$p(A) = p(P) + \frac{\gamma}{a} \left[u(A) - u(P) + \frac{\bar{u}c \Delta t}{1 - \frac{\Delta x}{2}} \right]$$

where

$$\bar{u} = \frac{u(P) + u(A)}{2}, \quad \bar{a} = \frac{a(P) + a(A)}{2}$$

5. Compare the value of $P(A)$ obtained in step 4. with the one calculated in step 3. If the difference is not within an accepted range assume a new value for $P(P)$ and restart the procedure..

2.7. General Remarks About The Computational Procedure

Based on the Courant-Friedrichs-Lewy stability criteria the smallest Courant number is taken to be 0.5. It is noticed that values greater than 0.6 yields a unstable solution especially in the neighbourhood of the of axis symmetry. In this case the largest velocity is that of the shock, so the condition of stability is

$$\lambda u_s \leq 1.0$$

where, u_s is the velocity of the shock wave.

As the shock converges toward the centre its velocity increases, then in order to keep a constant Courant number, a much smaller mesh ratio is needed. Although, in this procedure we established an algorithm that changes the space interval Δx automatically as the shock wave progresses toward the centre, there is no way we can find the exact space step that gives a stable solution.

For the shock fitting outlined above the new location of the shock on $(n+1)\Delta t$ data line is not a nodal point. To adjust to this variable boundary condition new nodal points are established, by linear interpolation, on the data line $(n+1)\Delta t$. The local pressure at any point of the flow is obtained by linear interpolation along the new data line.

CHAPTER 3

EXPERIMENTAL SET UP AND PROCEDURE

3.1. Shock Tube

Experiments were performed in a conventional air-to-air shock tube made from seamless steel tubing with .7 *cm* wall thickness, 15.41 *cm* inside diameter and 5.81 meter total length. It consists of a 2 meter long driver section, followed by a 3.81 meter long driven section as shown in figure 3.1. Furthermore, the driven section is subdivided into two parts, namely, a 2.74 meter long and a 1.07 meter long test section. Standard and well centred flanges are adopted to assemble the different subsections using eight M18 bolts. Sealing is assured by the use of neoprene O-ring seals which are seated in some grooves machined on the different flanges. High vacuum grease is also applied around the O-rings to practically eliminate any possible leakage. The shock tube is supported by five rigid steel supporters whose height can be adjusted accurately. Compressed air supply for the shock tube is taken from a large high pressure reservoir this being charged by an electrically driven reciprocating compressor. The supply enters the shock tube via a 1 *cm* diameter copper tubing through a control panel. Pressure in the driven section could be atmospheric or sub-atmospheric, depending on the annular Mach number required in the experiment, namely, 1.44 and 1.26 corresponding to 63.31 *Kpa* and 1 *atm* driven pressure, respectively. Vacuum pressure is supplied by an electrically powered Edwards' vacuum pump through a copper tubing connected to the driven section. Pressure supply is

measured by a two of gauges mounted on a control panel; *MFG* testing gauges with operating range (0 - 760 *mm Hg*) and (0-40 *bar*) were used to measure the vacuum pressure and the pressure supplied to the driver section of the shock tube, respectively. Manually operated control valves are used to monitor the preset pressure ratio between the driver and driven sections for a given Mach number. A pneumatically driven plunger centred within the driver section of the shock tube is adopted to burst the diaphragm as in figure 3.2. Diaphragms are cut from Mylar plastic sheets of different thickness in accordance with the required shock strength. At the downstream end of the test section, a three conical area contraction were employed to magnify and redirect the annular shock wave to produce a cylindrically converging shock wave as it enters the implosion chamber.

3.2. Upstream Of The Test Section

As it approaches the test section, the originally produced normal planer shock wave is converted into a planer annular shock wave by a two-part aluminium annular tube, 101.6 *mm* in diameter and 1.830 meter long, mounted concentric with the driven section of the shock tube as shown in figure 3.3. The aluminium tube is held by four webs, 1.3 *cm* thick and 4 *cm* wide, carefully machined to fit into a 280 *mm* in diameter aluminium flange to assure its alignment inside the shock tube. The schematic of this flange is shown in figure 3.4. Here, part *A* is a machined such that its internal bore is equal to the inner diameter of the shock tube. Part *B* is a ring with 10 *mm* outer diameter and 7.6 *cm* inner diameter and it equipped with four webs, 4 *cm* wide and 1.3 *cm* thick. To minimise

the effect of the webs on the shock front shape, fins of 10 degree inclined angle are placed at their both ends. A 5 degree chamfer is machined at the upstream end of the aluminum tube to minimize any disturbances caused by the inlet geometry and to assure a smooth transition from normal to annular shock wave. All the parts are designed to fit properly to avoid any possible leakage.

At the end of the shock tube a three increment area is made by means of a 20 *mm* thick and 150 *mm* diameter cylindrical part fitted inside an aluminium flange located at the downstream end of the shock tube using a set of eight *M18* bolts. An inner bore is made in the aluminium flange to accommodate a fine quality optical glass window as shown in figure 3.5. Rubber gasket of .5 *mm* thickness is used for sealing. Using this set up the annular shock wave, propagating between the two concentric aluminium tubes, is magnified as it passes through the three-area contraction and then turned ninety degree to its original direction of propagation to finally become a cylindrical shock. This cylindrical wave converges as it moves in the cylindrical implosion chamber (test section).

3.3. Test Section

The original test configuration is shown in figure 3.6. To vary the width of the cylindrical chamber' width without simultaneously modifying the geometry of the three-area contraction a more flexible design is introduced. It consisted of a 70 *mm* diameter concentric disk, mounted at the end of a 102 *mm* diameter cylinder and made to move axially inside the implosion chamber to vary its width as in figure 3.7. At the vicinity of

the cylindrical disk edge the converging shock is split into two parts one of which will propagate into the test section. To assure a smooth separation and avoid unnecessary disturbances a 15 degree chamfer is machined on the cylindrical disk. Shims of different diameter were used to vary the chamber's width. Alignment of the cylindrical disk is assured by a cylindrical step machined at its end and set to fit into a ground cylindrical bore in the 102 *mm* diameter part. In the previous design where of the gap width variation is obtained through a direct movement of the 102 *mm* diameter cylinder, it was not possible to analyze shock propagation without modifying the flow condition at the three-element contraction. The advantage of the new design is to isolate and examine the influence the boundary layer growth on the flow behind the shock. The changes in the post-shock conditions will be reflected on the shock strength through a complex wave interaction. Using this set up the analysis can be extended to very small chamber widths without choking the initially produced shock wave as the geometry of the three-element contraction is altered.

3.4. The Schlieren System

Figure 3.8 is a schematic representation of a conventional schlieren photography system. This set up consists mainly of a 4 *Kv*-spark source charged by a high voltage power amplifier and operates at pulse rate less than .10 microseconds. A pair of condensing lenses of focal length 17.5 *cm* were placed adjacent to the light source. Their function is to focus the light rays to single points on both the knife edge and the spark electrode located at their focal distances. The Knife edge, which is made of four razor

blades held together to an adjustable frame by four screws, is used to monitor the amount of light sent to the camera and provide a sharp and effective light source and remove unwanted secondary images [31]. To reorient the light beams so they can pass through the implosion chamber a double headed spherical mirror with 1230 *mm* focal length is employed. After passing through the test section, the light rays were again reflected on the spherical mirror then they were redirected through a plane mirror onto an open shutter camera. To assure the alignment of the different components of the system a continuous light source is used. The schlieren system is triggered by a pressure transducer placed upstream of the three-element contraction. Some difficulties were encountered when we attempted to photograph the converging shock wave as it collapses at the centre due to the finite time delay of the system. The set up is then adjusted by trial and error so that all the photographs are taken by referring to the converging shock collapse time ($t=0$).

3.5. Experimental Procedure

Before firing the shock wave, the shock tube was checked carefully for any nonalignment or leakage. It is also cleaned for any mylar fragments resulting from previous firings. Mylar sheet of .5 *mm* thickness, which was determined experimentally, was secured between the driver and driven sections. The test section was cleaned and initially set to 2.5 *mm* width, using shims of different thickness, separately. Then it is placed inside the shock tube axisymmetrically and secured to the downstream end of the annular aluminium tube. Initially the pressure at the driver section is raised to 30 *psig* and the pressure at driven section is kept at atmospheric conditions. Then the shock tube was

triggered and the mylar diaphragm was ruptured. Oscilloscope traces, obtained from piezoelectric pressure transducers, with sensitive element diameter of 2.5 mm and pressure/voltage gain presented in table 3.1, placed at radial distances of 35.00, 24.13, 13.97, 8.89 and 3.81 mm from the cylindrical chambers' centre, were either photographed by oscilloscope camera or directly traced on ALLEN datagraphs. A set of photographs for the converging/diverging cylindrical shock were also obtained in order to study its stability. Shock waves were generated with two different values of pressure ratio across the diaphragm that is 30 psig/1 atm and 50 psig/30 cm Hg for cylindrical chamber widths ranging from 2.5 mm to .33 mm.

Initially the Mach number for the planer shock wave M_{sp} was found from the shock tube relationship given by:

$$M_{sp} - \frac{1}{M_{sp}} = \left(\frac{a_4}{a_1}\right) \left(\frac{\gamma_1 + 1}{\gamma_4 - 1}\right) \left(1 - \left[\frac{2\gamma_1 M_s^2 + (\gamma_1 - 1)}{\gamma_1 + 1} \left(\frac{p_1}{p_4}\right)\right]^{\frac{\gamma_4 - 1}{2\gamma_4}}\right) \quad (3.1)$$

where a_4 and a_1 are sonic speeds at the driven and driver sections respectively. Similarly, γ_4 , γ_1 are the specific heat ratio for high and low pressure sections of the shock tube. However, as the shock propagates downstream its strength is altered, partially due to wall friction and boundary layer formation in the shock tube and during its transformation from planer to annular shape. It is obtained experimentally by placing a pressure transducer with 327 Kpa per volt gain, slightly upstream of the three-element contraction. Pressure measurements were also taken along the test section at different radii. Typical oscilloscope traces are shown in figure 4.1. The first sudden jump in voltage which

signals the passage of the annular shock is used to measure its strength. Knowing the voltage rise across the shock Δv and the transducer gain G_p , shock strength can be calculated using:

$$\Delta p = G_p \Delta v \quad (3.2)$$

Shock Mach number M_s , can then be calculated from the following relation(11):

$$M_s = \left(1 + \frac{\gamma + 1}{2\gamma} \frac{\Delta p}{p_1}\right)^{\frac{1}{2}} \quad (3.3)$$

where p_1 is the pressure/vacuum ahead of the shock.

In this experiment two Mach numbers were used, namely 1.26 and 1.44 corresponding to (30 *psig*)/(1 *atm*) and (50 *psig*)/(30 *cm Hg*) shock tube pressure ratio, respectively. These values are slightly less than those found using equation (3.1) which are used to set the shock tube pressure ratio. The second jump in the oscilloscope traces signals the presence of a reflected shock wave formed as the annular shock reaches the three-area contraction. It has no significance as far as this experiment is concerned.

For a purpose of double checking, a second method was adopted to calculate the annular shock strength. Two transducers were placed upstream of the three-area contraction at a distance $\Delta x = 152 \text{ mm}$. from each other. From the definition of Mach number we have:

$$M_s = \frac{u_s}{a_1} \quad (3.4)$$

where u_s is the absolute shock wave speed given by:

$$u_s = \frac{\Delta x}{\Delta t} \quad (3.5)$$

substituting equation (3.5) into equation (3.4) we get:

$$M_s = \frac{\Delta x}{a_1 \Delta t} \quad (3.6)$$

here, Δt is the measured time interval during which the shock travels the distance Δx and a_1 is the local speed of sound ahead of the shock given by

$$a_1 = \sqrt{\gamma R T_1} \quad (3.7)$$

where T_1 , γ and R are the measured temperature ahead of the shock wave, the specific heat ratio and the gas constant, respectively. Pressure difference across the shock can be calculated using:

$$\Delta p = \frac{2\gamma p_1}{\gamma + 1} (M_s^2 - 1) \quad (3.8)$$

Mach numbers obtained using both methods are close within a .2% error. This error is very insignificant since the attenuation of the shock due to both the three-element contraction and the boundary layer formation in the implosion chamber is much greater than that caused by the shock tube.

TABLE 3.1 transducers' gain and radial location

TYPE	SN 1178	SN 1175	SN 1239
GAIN (Kpa/volt)	231	327	377
LOCATION (mm)	24.13 35.00	13.97 8.89	3.81

CHAPTER 4

RESULTS AND DISCUSSION

Exact solutions to converging/diverging cylindrical shock waves were numerically obtained by integrating the characteristics equations using the Hartree time integration scheme. These results were compared with those obtained experimentally using miniature piezoelectric pressure transducers. Numerical results of the shock Mach number versus the cylindrical chamber radius were also compared with those obtained by the CCW Area-Mach relationship. Boundary layer effects was experimentally examined by varying the cylindrical chamber width using a new model. Symmetry of the converging shock was examined from a set of spark schlieren photographs taken near the geometric centre of the cylindrical chamber. The details are presented in the following sections.

4.1. Pressure and Shock Mach Number Measurements

Based on the theoretical finding of Guderley [12], Mach numbers of converging cylindrical shocks vary according to the relation $M_s \propto R_s^{-n}$. Where n is a constant which depends on the specific heat ratio γ . As the converging shock Radius R_s goes to zero, M_s becomes infinite. To determine the local values of the shock Mach numbers, pressure measurements were carried out at different locations along the shock path. Typical oscilloscope traces are shown in figure 4.1a-d. These were obtained from piezoelectric

transducers located at four different radii, $R= 24.13 \text{ mm}$, 13.87 mm , 8.89 mm and 3.87 mm with a cylindrical chamber width of 2.5 mm and a plane shock wave of Mach number 1.44. As noted in the figures there are two sudden increases in pressures; one corresponds to the converging shock and the other to the expanding one. Following the passage of the converging shock, the pressure increases gradually due to continuous wave reflection resulting from the area change. The first sudden increase in pressure ΔP_i corresponds to the incident shock and is used to determine the shock Mach number using the following relation :

$$M_i = \sqrt{\frac{\gamma+1}{2\gamma} \frac{\Delta P_i}{P_1} + 1} \quad (4.1)$$

where p_1 is the pressure in the driven section.

From equation (4.1) and the experimental results presented in figures 4.1a-d, the shock Mach number variations with radius were obtained. The results are shown in figure 4.2. Here, the radial dependence of the shock strength is very evident. Additionally, the experimental curve is characterized by a monotone profile indicating the absence of local acceleration or deceleration of the converging shock wave. These results were compared with those obtained theoretically by the CCW theory and numerically by the method of characteristics. A good agreement was noted between the three sets of data. However, at larger radius there is a tendency for the experimental points to lie below the theoretical curves. This slight divergence could be attributed to the multiple lateral reflection of the

cylindrical shock as it passes through the area contraction. Deviation of the numerical data from the simplified CCW solution represents the net effect of the secondary wave reflection, which was omitted in the derivation of the theory. Near the geometric centre the effect of these disturbances become insignificant and the three curves are almost identical. The only parameter that controls the converging shock wave strength is the area change. The scale of variation of shock strength due to flow disturbances is much negligible compared to that of area change. Due to the finite size of the transducer's sensitive element it was not possible to determine Mach number at very small radius. In this experiment the initial Mach number is 2.04 measured at $R_o = 35 \text{ mm}$ where R_o is the distance from the centre to the outer edge of the moving disk in the test section. At this radial location the calculated Mach number is 2.07. Since both the experimental and the theoretical curves merge at smaller radius, the experimental amplification factor was expected to be higher than the theoretical one.

Similar tests were conducted for annular shock Mach number of 1.26 with a cylindrical chamber width of 2.5 mm for $R=24.13 \text{ mm}$, 13.87 mm, 8.89 mm and 3.81 mm. A plot of Mach number versus radius is obtained using equation (4.1) and the oscilloscope traces shown in figures 4.1e-h. The results are shown in figure 4.3. Here, the Mach number variation follows the same trend as the previous case. However, experiment points tend to lie slightly under the theoretical curves at smaller radius than that of the stronger case. These relatively large discrepancies are partially due to the multiple reflection downstream of the contraction area. In addition this deviation suggests

that initially weak shocks tend to be more influenced by the flow conditions behind them. This effect diminishes as the converging shock approaches the centre.

Figure 4.4 represents the variation of the shock strength with the radius in a log-log scale for an annular Mach number of 1.44. Here, the converging shock amplifies according to power law $M=CR^n$ with $n \approx .20$. This value for n is slightly higher than that obtained by Chisnell [18] with $n \approx .197$ for strong shocks. This minor deviation implies that boundary layer and flow complexity due to the shock-area contraction interaction has no significant effect on shock attenuation for cylindrical chamber widths greater than 2.5 mm.

Note that all tests were carried out for a single cylindrical chamber width of 2.5 mm. Good agreement indicates that boundary layer has a minimal effect on the cylindrical shock propagation. The main parameter contributing to the shock attenuation is the lateral instability of the converging shock, specifically in the case of larger cylindrical chamber widths. This factor is the outcome of a significant change in flow variables along the shock front which in turn induces an important shock deformation. Consequently, multiple reflections take place as the shock converges toward the centre. These reflections cause the pressure to fluctuate about a mean value, as seen in the oscilloscope traces. As the converging shock approaches the centre, shock front deformation becomes large, which eventually results in a Mach type reflection followed by a shock collapse. For narrow cylindrical chambers this may be different. Further details concerning

cylindrical shock propagation in a narrow cylindrical chamber will be discussed in the following section.

4.2. Narrow Cylindrical Chamber Width

4.2.1. Experimental Observations

In order to determine the influence of boundary layer on shock wave propagation, a new model, shown in figure 3.7, was used. A set of tests were carried out for an initially strong shock ($M = 1.44$) and cylindrical chamber widths of 0.6 mm and 0.3 mm . Results are shown in figures 4.5a-d. Pressure measurements were taken 24.13 mm , 13.97 mm , 8.89 mm and 3.81 mm from the geometric centre. At these radial locations the pressure at a fixed point behind the converging shock increases with time and decreases as the reflected shock passes. The experimental results corresponding to cylindrical chamber widths of 0.30 mm , 0.60 mm and 2.5 mm were compared to the numerical values obtained using the method of characteristics as shown in figure 4.6 through figure 4.16. For $W=0.6\text{ mm}$ and 0.3 mm pressure distribution behind the converging shock is found to be lower than that corresponding to the cylindrical width of 2.5 mm which clearly illustrates that flow in region upstream of the shock displays a high degree of unsteadiness resulting in an important shock attenuation. Since the effect of area contraction is well isolated in the new model, the main source of disturbance is the viscous effect. The overall trend of the results obtained suggests that boundary layer influence on flow behaviour amplifies as the converging shock approaches the centre. The interaction of the incident shock wave and the change in the cylindrical chamber

radius gives rise to two types of shock, namely, a reflected shock and a transmitted one. The reflected wave propagates upstream as a compression wave when the change in radius is negative (converging shock) and as an expansion wave if the change in radius is positive (diverging shock). During the convergence process reflected disturbances result in a pressure increase in the pre-shock region. This effect causes the boundary layer to slow down and consequently thicken considerably depending on the converging shock strength. This thickening of the boundary layer results in a pressure increase in the free stream zone causing the flow to slow down. This phenomena has a significant effect on the driving mechanism of the converging shock. In the case of the cylindrical width of $.30\text{ mm}$ this effect is more pronounced. An important shock attenuation is observed. Flow non-uniformity behind the shock increases immensely as the shock progresses toward the centre. Such a phenomena can be seen from figure 4.14 to figure 4.16 where a large pressure fluctuation is present. In the case of cylindrical width of 0.6 mm a reasonably good agreement between the experiment and the computational is observed. The discrepancies between the two sets of data is a result of the complex interaction between the upstream moving disturbances and boundary layer. The observed drop in pressure in the pre-shock domain could also be attributed to no-uniformity of flow properties along the shock front. This variation induces a large shock deformation which grows larger with the widening of the cylindrical chamber. As the shock propagates toward the centre this effect becomes very significant yielding a lateral reflection of the shock which in turn results in pressure drop and adds to the complexity of the flow behind it. As discussed above the interaction of the reflected shock wave and a positive

radius change will produce a transmitted shock (diverging) and a rereflected wave (expansion wave). The latter will propagate downstream causing a sharp drop in pressure behind the diverging shock wave. The diverging process is quite complex because it includes shock boundary layer interaction particularly at very narrow cylindrical chamber width (.30 mm). This is concluded from the pronounced difference between the computational maximum pressure and the experimental results. Moreover, experimental values were obtained from a digital oscilloscope which gives a discrete number of points and therefore is unable to detect the exact value of the sharp peak noted due to the shock reflection. Behind the diverging shock the rate of pressure decrease obtained experimentally agrees very well with the computational. There is, however, a difference in the time at which the diverging shock reaches the sensitive element of the pressure transducer. This indicates a dramatic shift in the centre of implosion. This effect implies that boundary layer causes the converging shock to collapse at a much earlier stage. The deviation of the centre of implosion from the geometrical axial is smaller in the case of .60 mm width compared to the .30 mm cylindrical chamber configuration.

Additionally, a set of experiments were conducted for $M_0=1.26$ and $R=24.13$ mm, 13.87 mm, 8.89 mm and 8.81 mm with $W=0.60$ mm and 0.30 mm. From the results shown in figure 4.17 to 4.22 it can be concluded that pressure attenuation due to the narrowing of the cylindrical chamber is more significant than that corresponding to the strong case. Flow non-uniformity is quite strong particularly at smaller radii.

To determine the boundary layer effect on converging cylindrical shocks strength, Mach number versus radius plots were obtained using equation (4.1) and the oscilloscope traces presented in figures 4.5 and 4.26. The results are presented in figures 4.23 and 4.24 for cylindrical chamber widths ranging from 2.5 *mm* to .30 *mm* and initial Mach number of 1.26 and 1.44, respectively. From the figures the inlet conditions ($R = R_o = 35 \text{ mm}$) just downstream of the contraction area were found to be unaffected by the variation of the cylindrical chamber width. This demonstrates the ability of the new model in isolating the effect of the boundary layer on the shock wave propagation from those due to the disturbed nature of the flow downstream of the contraction area. The narrowing of the cylindrical chamber width resulted in a weaker transmitted shock wave. This is attributable to the boundary layer effect since the ratio of the boundary layer thickness to the cylindrical chamber width is greater than .167. For the stronger shock ($M = 1.44$) wave the boundary layer influence is more evident at larger diameter. As the shock progresses towards the centre, the disturbances due to the presence of the boundary layer are suppressed. This observation is valid only at cylindrical chamber width greater than .6 *mm*. For cylindrical chamber of .30 *mm* the shock attenuation is more severe.

To illustrate the effect of the area contraction on shock amplification, tests were carried out for an incident plane shock of 1.44 using the original model. The results are presented in figure 4.25. It is clear that at larger radius, the 0.6 *mm* width is found to produce stronger shocks than the 2.5 *mm* one. However, at smaller radius the latter results in a stronger converging shock wave.

At larger radius, where the flow is almost two-dimensional, and for cylindrical chamber width of .30 *mm* the converging shock displays a slight decrease in strength. This phenomena is interpreted to indicate the presence of a local deceleration somewhere downstream of the contraction area. Here the boundary layer may have attained a maximum value creating highly unsteady pre-shock flow conditions. This effect was studied by Mirels [32] for two-dimensional shock tube. For cylindrical width of 0.6 *mm* the boundary layer effect is only dominant at larger diameter (up to 13.8 *mm*). However, as the shock approaches the centre of implosion it gains enough momentum enabling it to overcome the disturbances generated by the boundary layer.

To illustrate the effect of the boundary layer on the amplification rate of shock strength a log-log plot of the shock Mach number versus radius is presented in figure 4.4. It is clear from the figure that the shock amplifies according to R^n . For cylindrical chamber width of 2.5 *mm* boundary layer effects are neglected and $n=0.20$. for the 0.60 *mm* case $n=.189$, if the new design is employed. Using the original model a lower shock amplification rate is noted with $n=.165$ for cylindrical chamber width of 0.6 *mm*. This effect is primarily attributed to the area contraction. For the cylindrical width of .30 *mm* the shock propagation did not obey the power law. This is a result of a significant weakening of the shock subjected to the boundary layer effect.

4.2.2 Theoretical Formulation

Shock attenuation in the case of plane shocks propagating in constant area tube was

studied in details by Mirels [32]. For a small range of M_s , the pressure variation behind the shock follows the relation:

$$\Delta P_{2,d} \sim \frac{(R_o - R_s)^{1/2}}{W} \quad (4.3)$$

where,

$\Delta P_{2,d}$: Pressure variation downstream of the shock (Kpa)

W : Cylindrical width (mm)

R_o : Radius of the concentric disk (mm)

R_s : Shock wave radius (mm)

From the normal shock wave relation we have

$$M_s = \sqrt{\frac{P_2}{P_1} \frac{\gamma+1}{2\gamma} + \frac{\gamma-1}{2\gamma}} \quad (4.4)$$

where,

P_1 : Pressure upstream of the shock (Kpa)

P_2 : Pressure downstream of the shock (Kpa)

The change in Mach number due to the boundary layer and area change can now be approximated by the following relation:

$$M_s = \sqrt{\frac{P_2 - \Delta P_{2,d}}{P_1} \frac{\gamma+1}{2\gamma} + \frac{\gamma-1}{2\gamma}} (R_s/R_o)^{-n} \quad (4.5)$$

equation (4.3) can be written in an alternative form by introducing the proportionality term α

$$\Delta P_{2,d} = \frac{\alpha \sqrt{R_o}}{W_o} \frac{(1 - R_j/R_o)^{1/2}}{(W/W_o)} \quad (4.6)$$

substituting equation (4.6) into equation (4.5) we get the following relation:

$$M_s = \sqrt{\frac{P_2 - K \frac{\sqrt{(1 - R_j/R_o)}}{W/W_o}}{P_1} \frac{\gamma + 1}{2\gamma} + \frac{\gamma - 1}{2\gamma} (R_j/R_o)^{-n}} \quad (4.7)$$

where,

$$K = \frac{\alpha \sqrt{R_o}}{W_o}$$

and

W_o : Maximum cylindrical width (2.5 mm)

The coefficient K was found by correlation between the theoretical and experimental results. For the annular Mach number of 1.44, $K=14.2$. There is a good agreement between the experimental results and those obtained by equation (4.7) as noted in figure 4.24.

4.3. Stability Analysis

The stability of propagating cylindrical shocks is often related to the degree of axial symmetry of the shock front. A cylindrical shock wave is said to be stable if it maintains a cylindrical shape and axial symmetry throughout the converging/diverging process. On

the basis of this principle, schlieren photography is quite sufficient to analyze the stability of the shock front subjected to strong disturbances within the flow domain. The most important source of disturbance considered in this experimental analysis is the boundary layer as it interacts with the shock propagation. In order to provide a comprehensive qualitative analysis of the of the boundary layer effect, the cylindrical chamber was first narrowed to 0.6 mm and then to 0.30 mm . The latter cylindrical chamber configuration is associated with a significant change in the shock wave dynamics and a complex flow field, as concluded from the pressure analysis presented in the previous sections. In the subsequent paragraphs detailed discussion about the influence of boundary layer on the stability of converging/diverging cylindrical waves is presented.

In order to examine the effect of the cylindrical chamber configuration on the final shock wave stability and the flow condition, two sets of photographs were obtained for $W=0.6\text{ mm}$ and 0.3 mm and annular shock Mach number of 1.26 . Figures 4.27 and 4.28 show a sequence of spark shadowgraph for cylindrical chamber width of 0.6 mm and 0.3 mm , respectively. Each photograph was taken with similar shock tube firing using different time delay settings. This experiment showed a remarkable repeatability which made it possible to obtain a reliable series of photographs showing the evolution of the shock front shape as it approaches the centre of collapse.

From figure 4.27 one can infer that the converging shock seems to maintain its cylindrical symmetry up to a relatively small radius for a cylindrical chamber width of

0.6 mm. At the vicinity of the centre, the cylindrical symmetry is lost in favour of an elliptical one. This can be observed in figure photograph (b) and (c). For the 0.3 mm case shock asymmetry started at much earlier stage. In both cases the shock front does not regain its symmetry as it converges towards the centre. In figures 4.27d and 4.28f, two pairs of vortices are noted behind the expanding shock. The presence of these vortices reveals the occurrence of Mach type reflection which is characterized by the formation of two pair of triple point where an incident shock (converging shock), reflected shock, slip line and Mach stem intersect. This shock confluence is formed as the shock breaks down near the geometrical centre. The shift of the collapse centre from the geometrical one can be perceived from figures 4.27c and 4.28c where the shock collapsing is not very acute. In the 0.3 mm case shock collapse occurred in much wider region than the 0.6 mm case indicating a larger shift in collapse centre from the geometrical one. Unfortunately, the schlieren photographs were unable to depict the changes in the flow properties behind the converging shock as it undergoes the above-mentioned transformations. The only important observation as far as flow condition is concerned is the presence of some concentric circular rings behind the collapsing shock. These are seen in figure 4.28d and they are the result of multiple reflections of trailing weak waves off the upper and the lower walls of the cylindrical chamber. Apart from this, the presence of these circular rings may possibly be a consequence of the vibration effect that the experiment set up may undergo.

From figures 4.27d and 4.28f one can see that the diverging wave has regained the

circular symmetry and seems to be stable. Expanding trailing disturbances were formed and were stronger than those observed behind the converging shock. Flow non-uniformity is more pronounced and increases with the diverging shock propagation. This intense flow non-uniformity is the result of the strong expanding waves that trail the diverging wave. The latter disturbances have the effect of decreasing the flow velocity, significantly. Consequently, the vortices seem to maintain their position at the vicinity of the centre. In figure 4.28e the converging shock is transformed into a quatrefoils. The latter effect substantiates the general hypothesis [24] that states that the supports, used to hold the inner tube just upstream of the test section (see figure 3.3), are accountable for initializing shock perturbation. The presences of the quatrefoils agrees with the number of supports adopted in the present experimental work.

Similarly, a sequence of shadowgraphs was obtained for a cylindrical chamber width of 2.5 mm and a shock Mach number of 1.26. It is clear from figure 4.29 that the shock front is circular in shape. The shock maintains its symmetrical shape up to very small radii. The pair of vortices seen behind the diverging shock indicates that break down in shock front curvature did occur somewhere near the geometric centre. The relationship between the direction of propagation of these pairs of vortices and the shape of the shock before collapse will be discussed in section 4.3.2.

4.3.1. Amplification

The boundary layer effect on shock deformation is examined using the perturbation

parameter s , defined as,

$$\xi = \frac{\Delta R}{R_s}$$

where ΔR is the value of the shock displacement given by:

$$\Delta R = \frac{D-d}{2}$$

where D and d are the major and minor axis of the shock front, respectively. The average shock diameter is given by,

$$R_s = \frac{D+d}{4}$$

therefore we have

$$\xi = \frac{2(D-d)}{D+d}$$

From the shadowgraphs in figures 4.27 and 4.29 the variation in shock front perturbation was obtained. The results are presented in figure 4.30. The experimental values were compared to those obtained theoretically from the analysis of the stability of cylindrical converging shock (Butler, 1956). The theoretical perturbation parameter is given by:

$$\xi = \frac{\Delta R}{R_s} \propto \left(\frac{R_s}{R_o} \right)^{-0.598} \quad (4.8)$$

from the figure the experimental perturbation parameter was obtained

$$\xi = \frac{\Delta R}{R_s} \propto \left(\frac{R_s}{R_o}\right)^{-0.62}, \quad \text{for } W=0.60 \text{ mm}$$

$$\xi = \frac{\Delta R}{R_s} \propto \left(\frac{R_s}{R_o}\right)^{-0.60}, \quad \text{for } W=2.50 \text{ mm}$$

These relations are in fairly good agreement with the equation (4.8). The experimental results, however, tend to increase in a modest rate in comparison to the theoretical ones. This is due to the fact that Butler's analysis was based on a very high Mach number. In the present experiment, however, Mach number attains a reasonably high value only at the centre of collapse. In both relations the ratio of the shock deformation to the mean shock front radius does not tend to zero. It increases monotonically with shock front travel. The rate of shock distortion for $W=0.60 \text{ mm}$ grows more rapidly than that corresponding to $W=2.5 \text{ mm}$. This is an indication that a cylindrical shock wave, travelling in a narrow cylindrical chamber, tends to be more unstable. The converging shock does not seem to regain its symmetry. This analysis provides a good quantitative demonstration of the degree of shock deformation, but it fails to explain the nature of the shock collapse as it approaches the centre. The degree of sharpness of shock collapse dictates the final state of the gas at the centre of the cylindrical chamber. Therefore, more details are required to undertake this mechanism.

4.3.2 The Collapse Mechanism

To shed light on the different stages of converging shock collapse, a two-dimensional

test was conducted using a 51 by 51 mm square shock tube for a plane shock Mach number of 2.2. Here, the nearly elliptical shock reflection on both sides of the major axis (figure 4.28c) was simulated by considering a planar shock reflection from a curved wall. A sequence of spark schlieren photographs is shown in figure 4.31. The initially planar shock front is reflected from the centre of the wall curvature. The initial reflection is of the Mach reflection type followed by a regular reflection. The contact surfaces, resulting from the Mach reflection, roll up to form a pair of vortices. The latter continue to slowly propagate and remain behind the reflected shock where the particle path is relatively small. From the two dimensional tests of figure 4.31, the direction of propagation of the pair of vortices trailing behind the reflected shock indicates that for elliptical converging shocks a pair of vortices will form and will propagate in a preferential directions being perpendicular to the major axis of the converging elliptic shock.

CHAPTER 5

CONCLUSION AND RECOMMENDATIONS

5.1. Conclusion

The propagation and stability of converging/diverging cylindrical shocks in wide and narrow cylindrical chambers was studied, experimentally, through a series of pressure measurements and spark schlieren photography. These results were compared with those obtained numerically by the method of characteristics. The boundary layer effects on the shock stability were experimentally analyzed by examining a set of spark shadowgraphs taken for different cylindrical chamber configurations. The tests were carried out for two incident plane shock Mach numbers, namely, 1.26 and 1.44. From the present study the following conclusions can be drawn:

1. For a cylindrical chamber width of 2.5 *mm*, excellent agreement was noted between the experimental values and the numerical ones obtained by the method of characteristics. This suggests that the present shock tube employed prevails the same uniform upstream conditions that were employed in the derivation of the *CCW* theory and the numerical integration of the characteristics equations.
2. The proposed new model was effective in isolating the boundary layer effects

from those induced by the interference of the area contraction. Flow conditions at the test section inlet remained undisturbed as the cylindrical chamber was narrowed which enabled us to obtain a satisfactory comparison between the experiments and the CCW which was based on uniform flow conditions upstream of the area contraction.

3. Shock Mach number and flow condition in the test section depend strongly on the cylindrical chamber width. Narrow cylindrical chambers induce a sharp decrease in shock strength and an increase in flow non-uniformity. The latter is the result of a complex interaction between the boundary layer and the disturbances which propagate in the flow domain. Larger cylindrical widths, however, results in a severe lateral shock deformation and eventually leads to lateral shock stabilities.
4. The asymmetry of the test section is an important parameter that controls the shock attenuation and stability, particularly in the case of a narrow cylindrical chamber. For cylindrical chamber widths larger than 0.6 mm , the converging shocks were found to retain their symmetry down to small radii. For smaller width the circular symmetry of the shock is lost in favour of an elliptical one at a much earlier stage. In all cases, shock breakdown is followed by the formation of a pair of vortices that propagates in a direction normal to the major axis of the ellipse.

5. For all test section configurations the converging shock does not collapse to a single point. The distance between the centre of collapse and the geometric one is found to increase as the cylindrical chamber is narrowed.
6. In all cases considered, the diverging cylindrical shock was found to regain its cylindrical shape as it propagates outwards. However, its strength was strongly reduced by the chamber narrowing.
7. From the experimental results, an empirical equation was developed to determine the variation in shock strength with radius R for a wide range of cylindrical chamber width W . For cylindrical chamber widths $W/R_o > .04$, boundary layer is found to have almost no effect on shock propagation.

5.2. Future work

Most of the previous works indicate that converging shocks are unstable. If an attempt is made to improve the stability, some measuring devices must be available to indicate the degree of such improvement. Presently, Neemeh and his associates are considering the vortices as the measuring mechanism. They are developing a relationship between the vortex pairs size and shape and the degree of shock instability. Once this relationship is developed, attempts will be made to enhance the stability of the shock using the vortex geometry as the measuring tool of such an improvement.

REFERENCES

1. Lau, J. H., Kekez, M. M., Laugheed, G. D. and Savic, P., "Spherically converging Shock Waves in Dense Plasma Research", *Proceeding of 10th International Symposium on Shock tube and Waves*, 1979, p. 386.
2. Glass, I. I. and Sagie, D., "Application of Explosive-Driven Implosions to Fusion", *Physics of Fluids*, Vol. 25, 1982, pp. 269-270.
3. Glass, I. I. and Sharma, S. P., "Production of Diamonds From Graphite using Explosive-Driven Implosions", *AIAA Journal*, Vol. 14, No. 3, 1976, pp. 402-404.
4. Perry, R. W., "The Production and Stability of Converging Waves", *Ph.D. Thesis*, Cornell University, 1951.
5. Perry, R. W., and Kantrowitz, A., "The Production and Stability of Converging Waves", *Journal of Applied Physics*, Vol. 22, No. 7, July 1951, pp. 878-886.
6. Knystautas, R., Lee, B. H. K. and Lee, J. H. S. "Diagnostic experiments on converging detonations", *Physics of Fluids suppl. I*, 1969, pp. 165-168.
7. Takayama, K., Onodera, O., Hoshizawa, Y., "Experiments on the Stability of converging cylindrical shock waves", *Theoretical and Applied Mechanics*, Vol. 32, 1984, pp. 117-127.
8. Takayama, K., Kleine, H., Grönig, H., "An Experimental Investigation of the Stability of converging Cylindrical Shock Waves in Air", *Experiments in Fluids*, vol. 5, 1987, pp. 351-322.
9. Wu, J. H. T., Neemeh, R. A., Ostrowski, P. P., "Experimental Studies of the

- Production of Converging Cylindrical Shock Waves", *AIAA Journal*, Vol. 18, 1980, pp. 47-48.
10. Neemeh, R. A., "Experimental Studies of Converging Cylindrical Shock Waves Produced by Area Contraction", *Ph.D. Thesis*, McGill University, 1976.
 11. Matsuo, H., Nakamura, Y. "Experiments on Cylindrically Converging Blast Waves in Atmospheric Air", *Journal of Applied Physics*, Vol. 51, No. 6, June 1980, pp. 3126-3129.
 12. Guderley, G., "Powerful Spherical and Cylindrical Compression shocks in Neighbourhood of the centre of the Sphere and the Cylindrical Axis", *Luftfahrtforschung*, Vol. 19, 1942, pp. 302-312.
 13. Butler, D. S., "The Stability of Converging Spherical and Cylindrical Shock Waves", *Armament Research and Development Establishment*, Report No. (B) 18/56, 1956.
 14. Stanyukovich, K. P., "Unsteady Motion of Continuous Media", *Gostekhizdat, Englo. Transl*, Pergamon Press, New York, 1960.
 15. Chester, W., "The Propagation of Shock Wave in a Channel Of Non-Uniform Width", *Quart. J. Mech. and Appl. Math.*, Vol. VI, Part 4, 1953, pp. 440-452.
 16. Chester, W., "The propagation of Shock Waves in a Channel, with Applications to Cylindrical and Spherical Shock Waves", *Journal of Fluid Mechanics*, 1958, Vol. 4, pp. 268-298.
 17. Chester, W., "The propagation of Shock Waves along Ducts of Varying Cross Section", *Advances in Appl. Mech.*, Vol. 6, 1960, pp. 119-152.

18. Chisnell, R. F., "The Motion of a Shock Wave in a Channel, with Applications to Cylindrical and Spherical Shock Waves", *Journal of Fluid Mechanics*, Vol. 4, 1958, pp. 268-298.
19. Whitham, G. B., "On the Propagation of Shock Waves Through Regions of Non-unicorn Area of Flow", *Journal of Fluid Mechanics*, Vol. 4, 1958, p. 337.
20. Butler, D. S., "Converging Spherical and Cylindrical Shocks", *Armament Research and Development Establishment, Report 52/56*, 1954.
21. Neemeh, R. A. *et al.*, "Stability of Normal Shock Reflected from a Concave Wedge-Shaped Wall", *Canadian Aeronautic Space Journal*, May, 1981, p.376.
22. Ahmad, Z., "A Theoretical and Experimental Study of the Stability of Converging Cylindrical Shock Waves", *Master Thesis*, Concordia University, 1984
23. Wu, J. H. T, Neemeh, R. A. and Ostrowski, P. P., "Stability of Cylindrical Converging Shock Perturbed by a Bleed Aperature", *Proceedings of the 12th International Symposium on Shock Tubes and Waves*, Jerusalem, 1979, p. 324.
24. Watanabe, M. and Takayama, K. "Stability of Converging Cylindrical shock Waves", *Shock Waves*, Vol. 1, 1991, pp. 149-160.
25. Rudinger, G., *Wave Diagrms for Non Steady Flow in Ducts*, D. Van Nostrand Company, Inc., Toronto, 1955.
26. Courant, R., Friedrichs, K. O. and Lewy, H., "Über Die Partiellen Differenzengleichungen Der Mathematischen Physick.," *Math. Ann.*, Vol. 100, 1928, p. 32.
27. Reo, P L., "Approximate Riemann Solvers , Parameter Vectors, and Difference

- Schemes," *Journal of Computational Physics*, Vol. 42, No. 1, 1981, pp. 195-211.
28. Moretti, G., "Computation of Flows with Shocks," *Annual Review of Fluid Mechanics*, Vol. 19, 1987, pp. 313-337
 29. Courant, R., Isaacson, E., and Rees, M., "On the solution of Nonlinear Hyperbolic Differential Equations By Finite Difference," *Communications in Pure and applied Mathematics*. Vol. 5, 1952, pp. 243-255.
 30. John, J. E. A., *Gas Dynamics*, Allyn-Bacon, Boston, 1984.
 31. Liepmann, H.W. and Roshko, A. *Elements of Gas Dynamics*, John Wiley & Sons, Inc., New York, 1967, pp. 159-161.
 32. Mirels, H., "Attenuation in a Shock Tube due to Unsteady-Boundary-Layer Action", *NACA TN-3278*, 1956

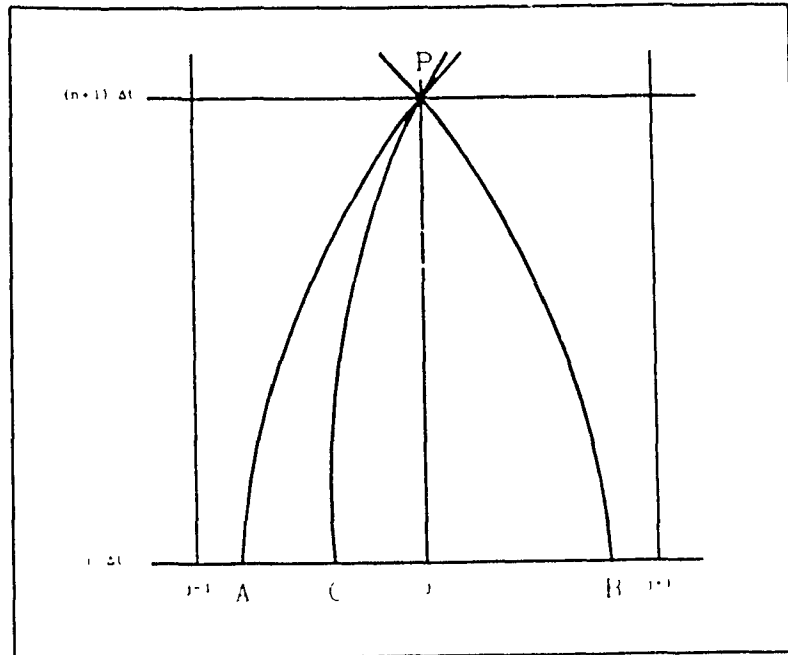


Figure 2.1. The general solution of the characteristics method

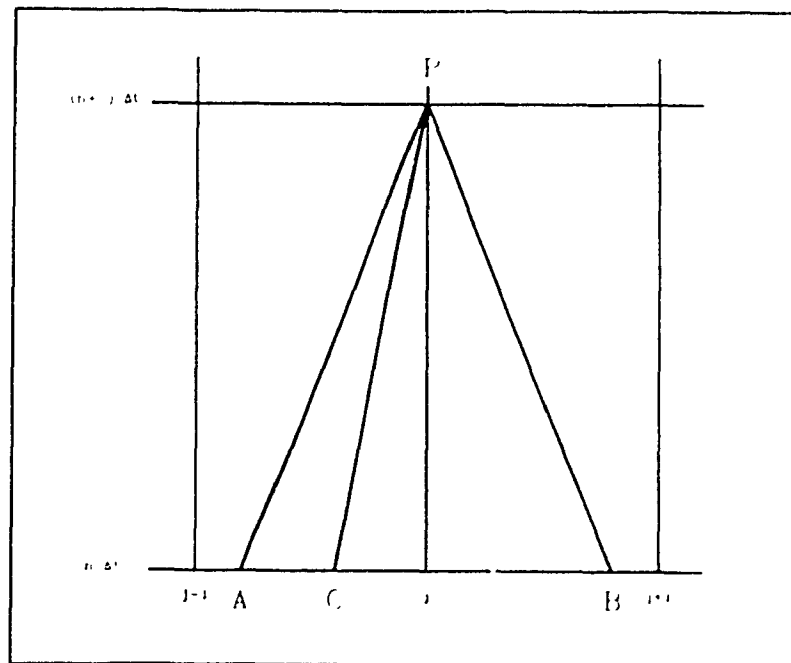


Figure 2.2. The computational solution of the characteristics method

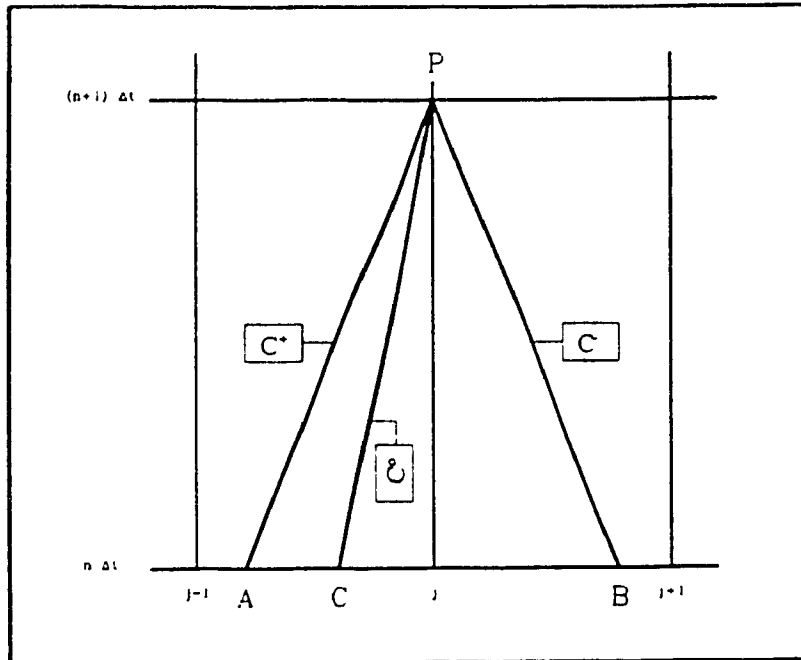


Figure 2.3. Characteristics method for a subsonic flow

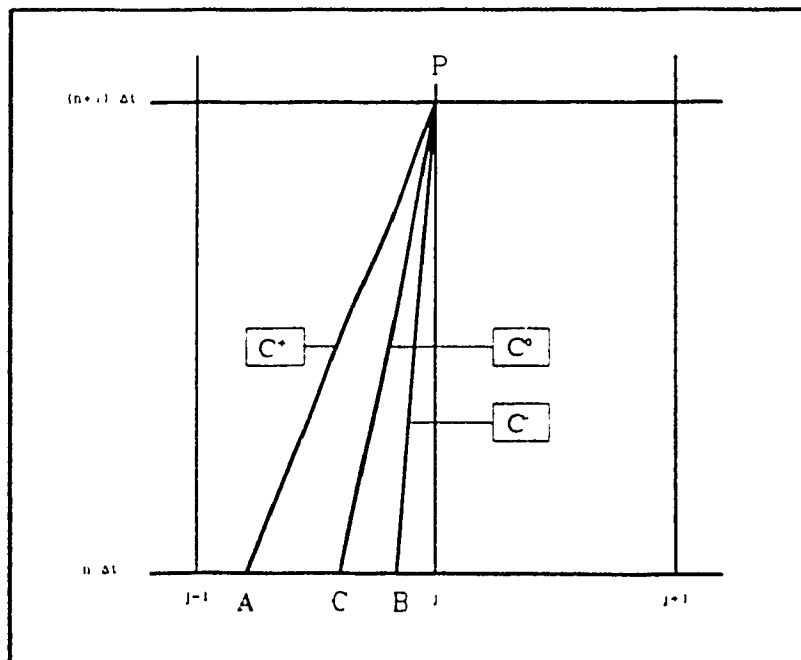


Figure 2.4. Characteristics method for a supersonic flow.

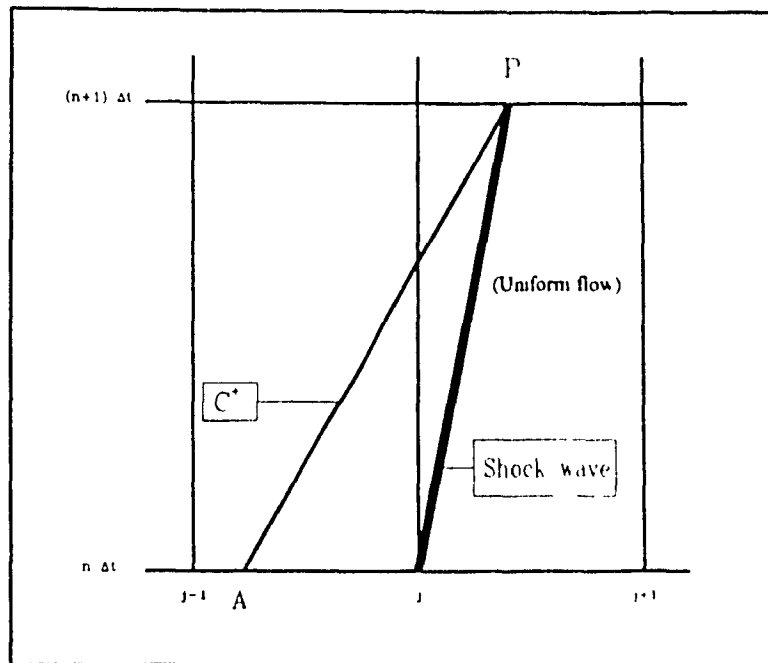


Figure 2.5. The characteristics method solution for converging shock points

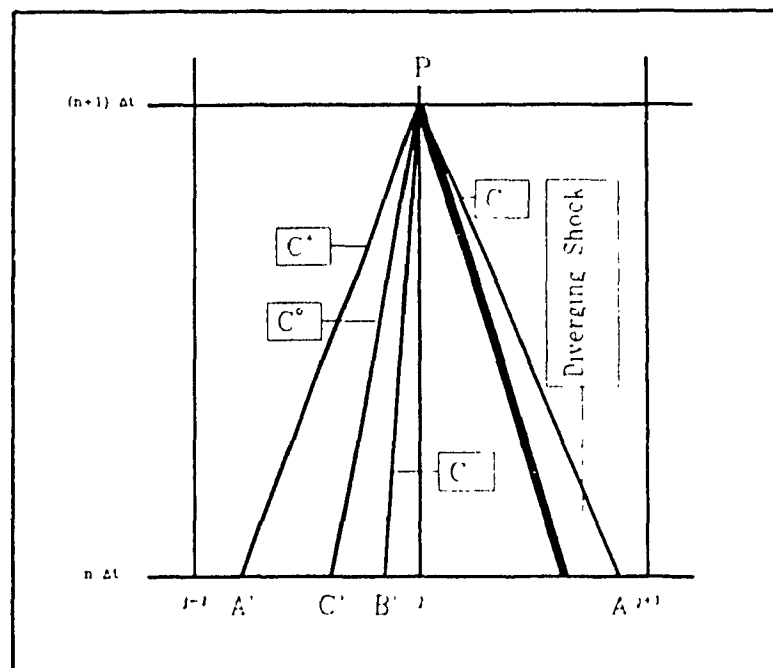


Figure 2.6. The characteristics method solution for diverging shock points

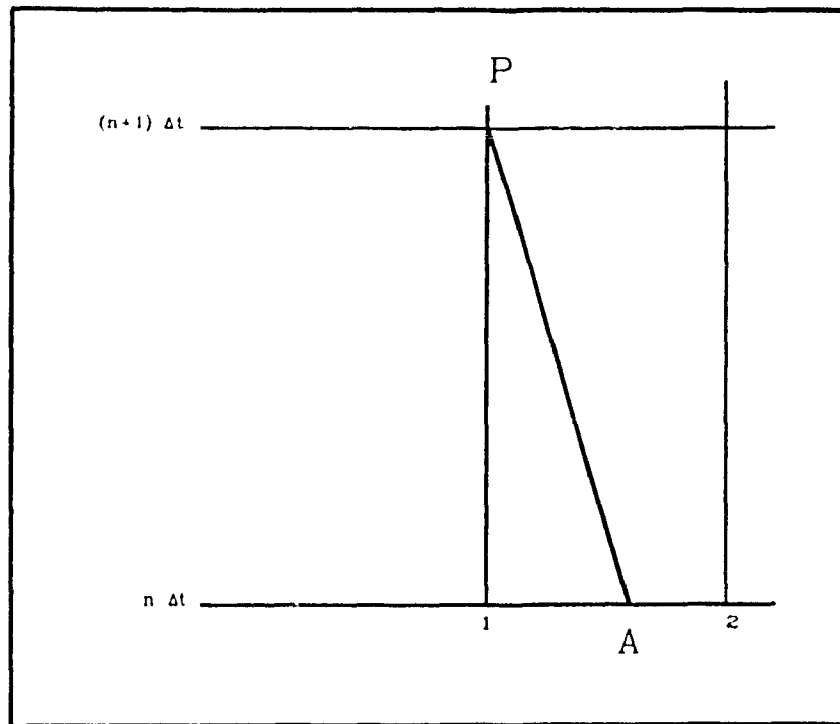


Figure 2.7. The characteristics method solution for flow points at the test section inlet.

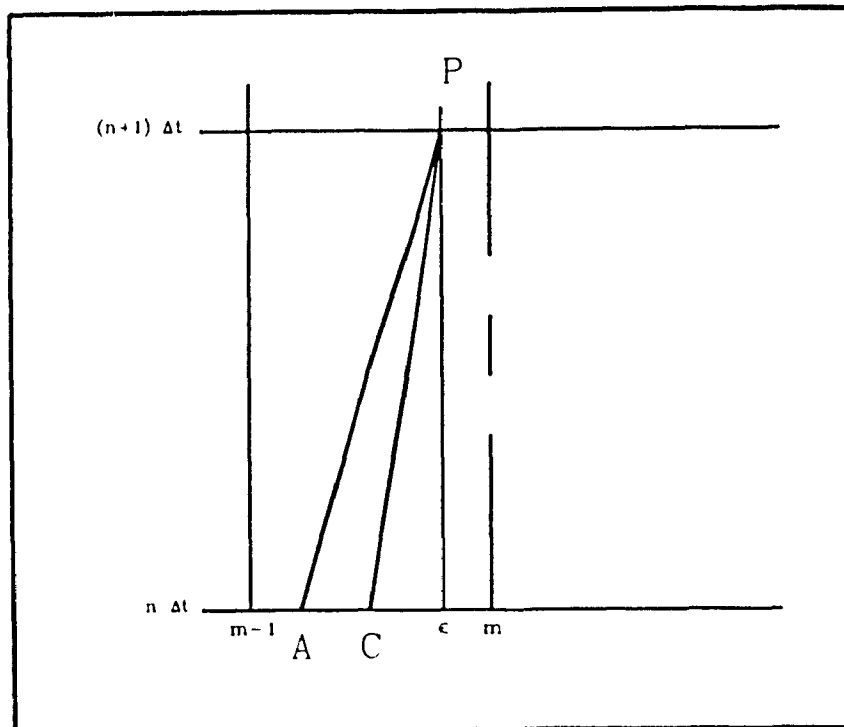


Figure 2.8. The characteristics method computational solution for flow points near the axis.

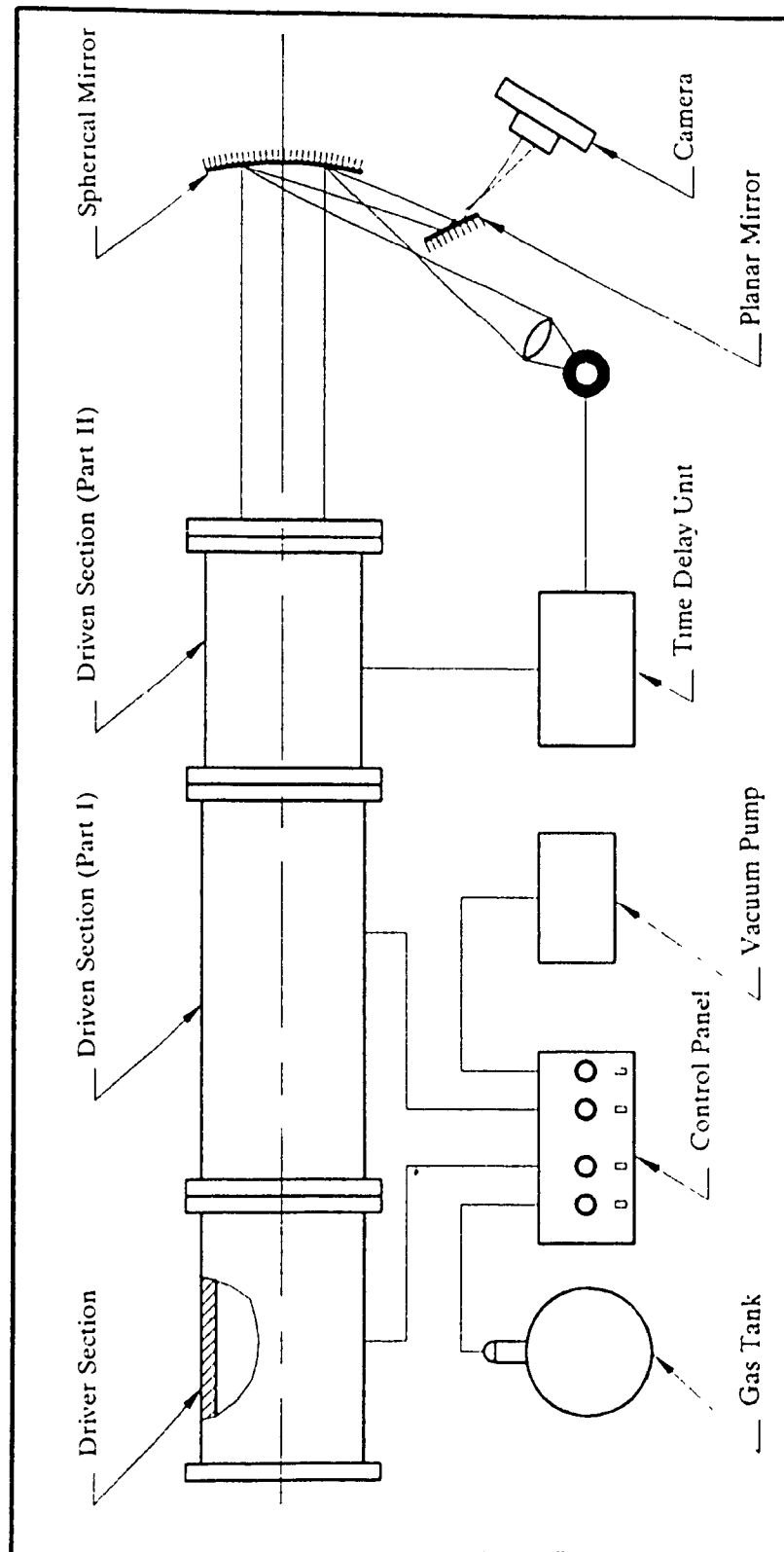


Figure 3.1. A schematic diagram of the experimental set up

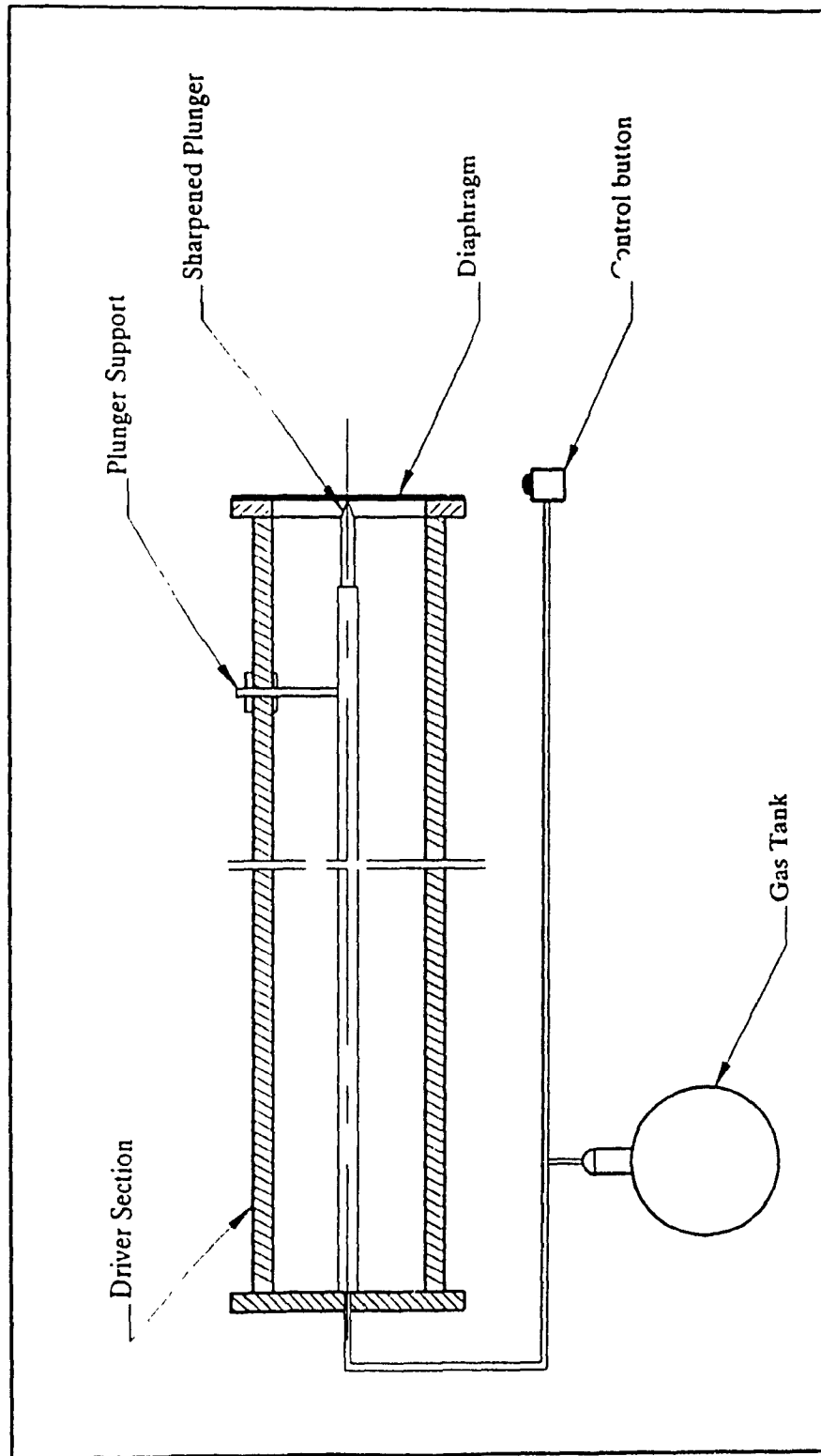


Figure 3.2. A schematic diagram of the plunger mechanism

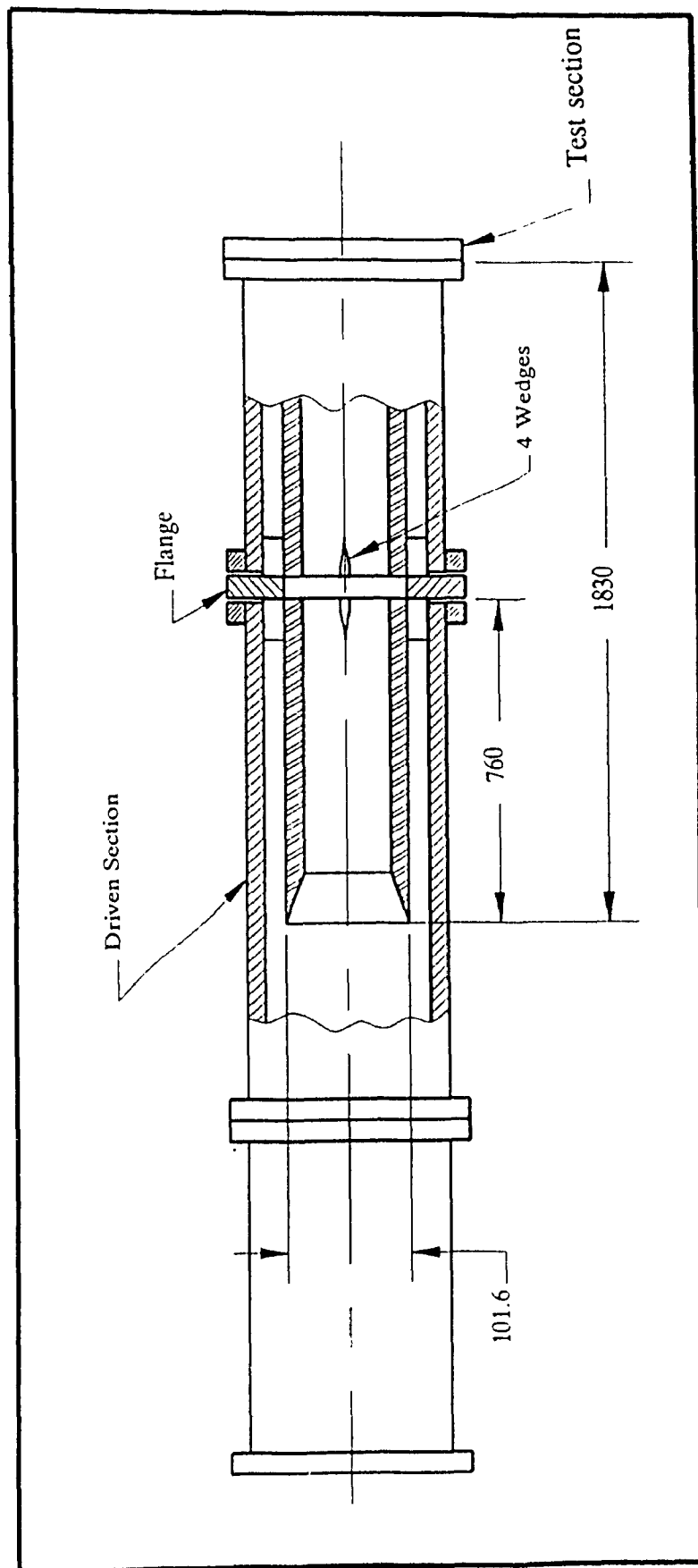


Figure 3.3. Upstream of the test section

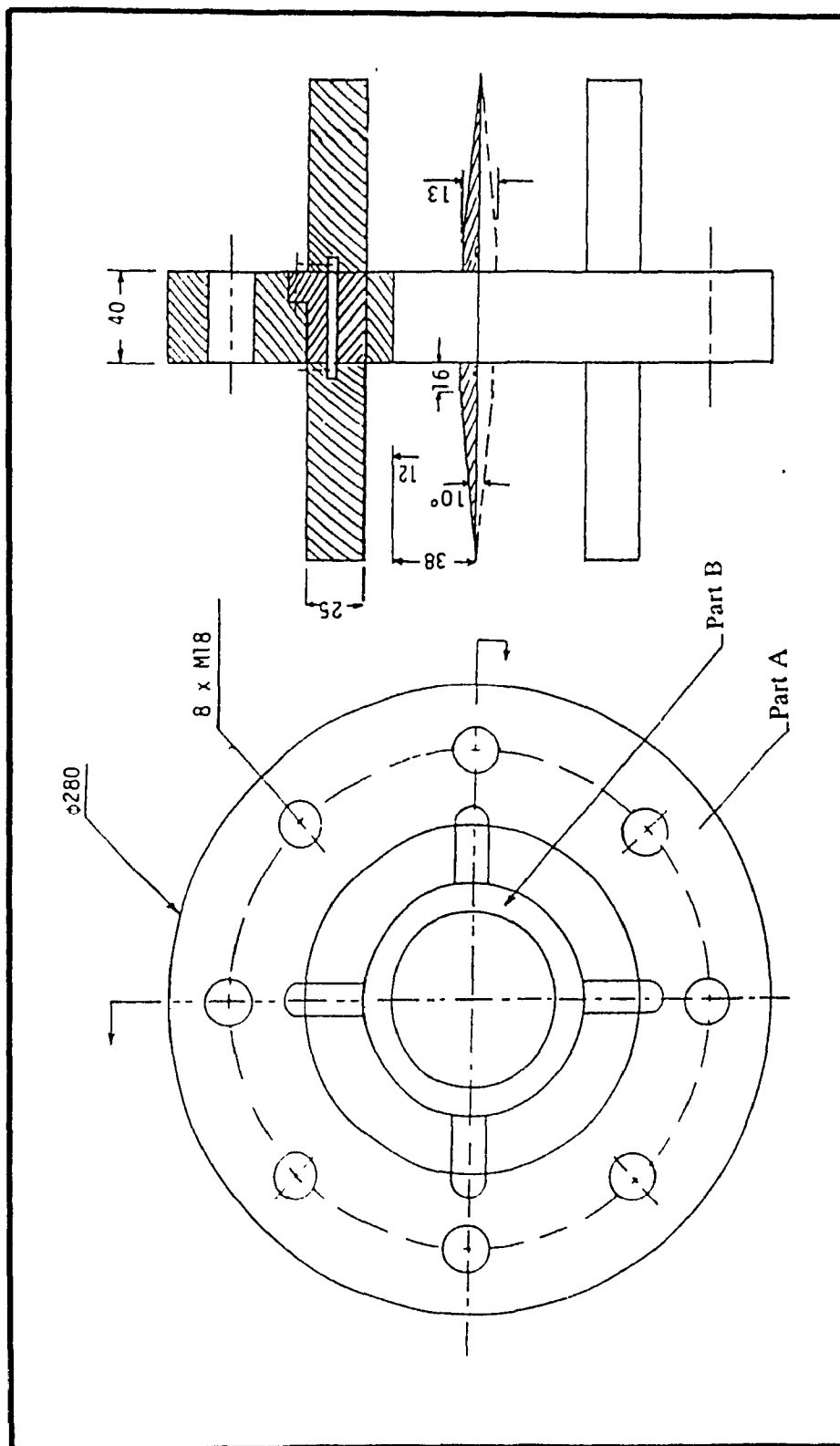


Figure 3.4. Sectional view of the flange

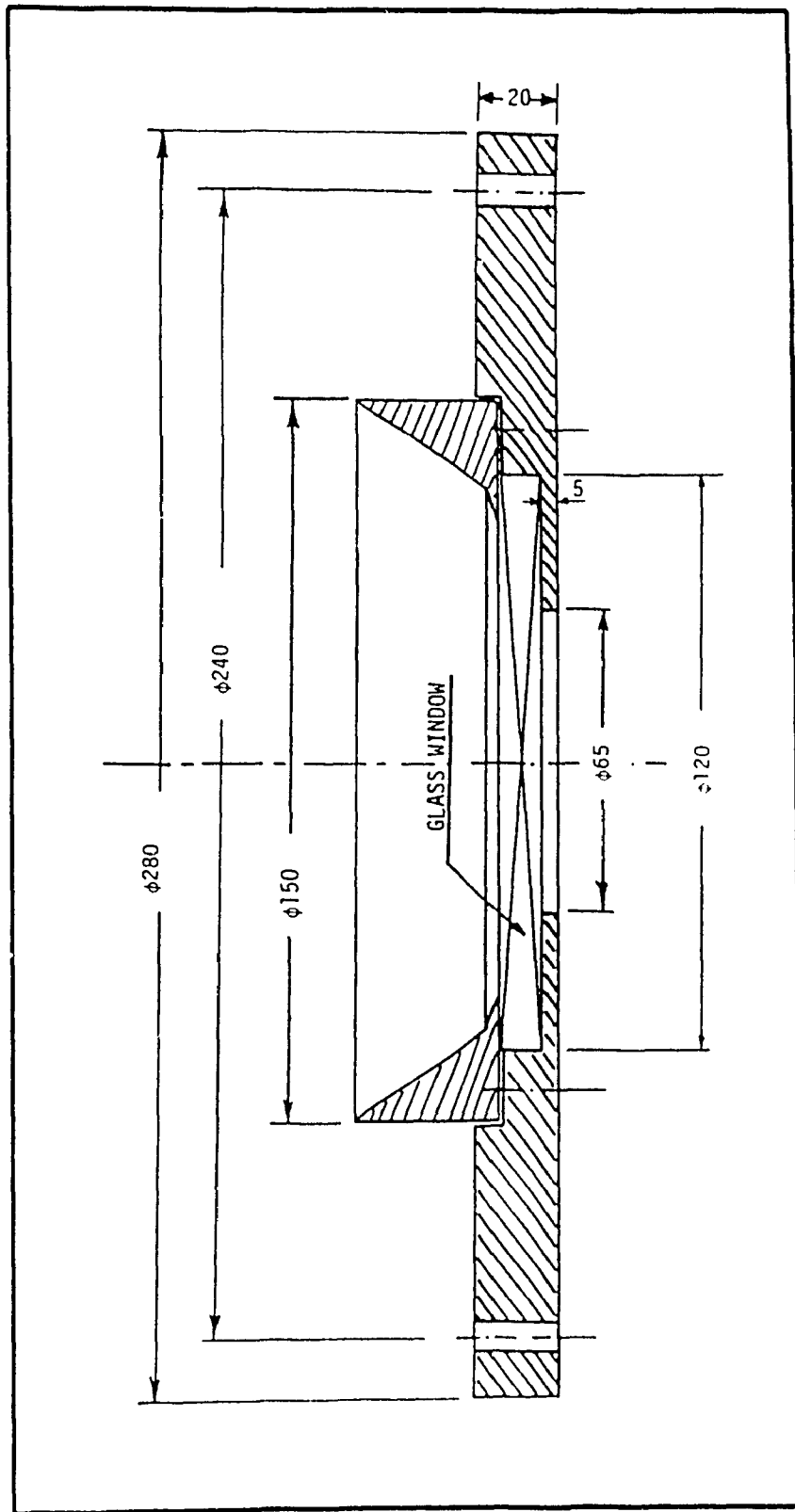


Figure 3.5. Sectional view of the downstream end of the shock tube

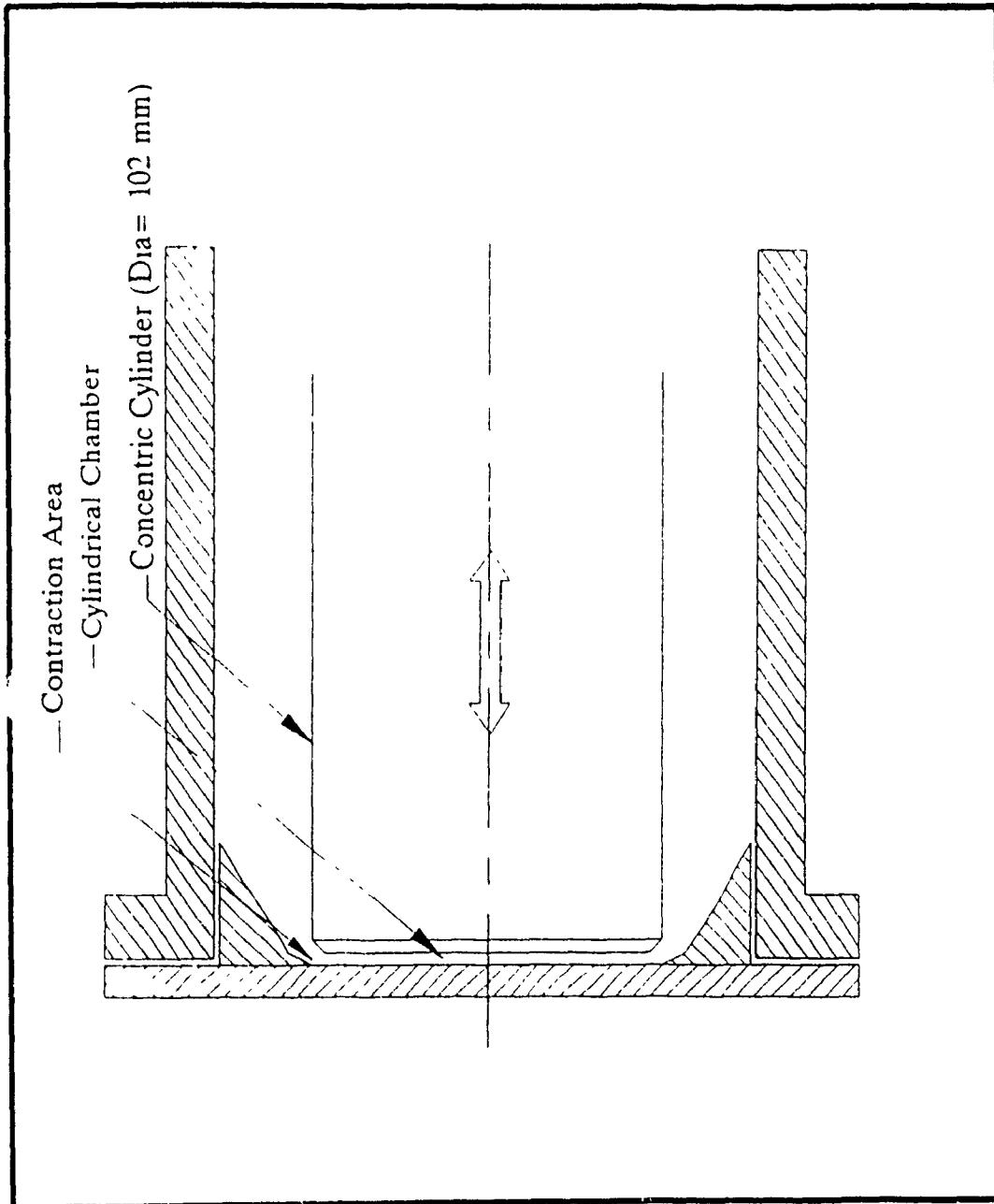


Figure 3.6. A schematic diagram of the test section (original model)

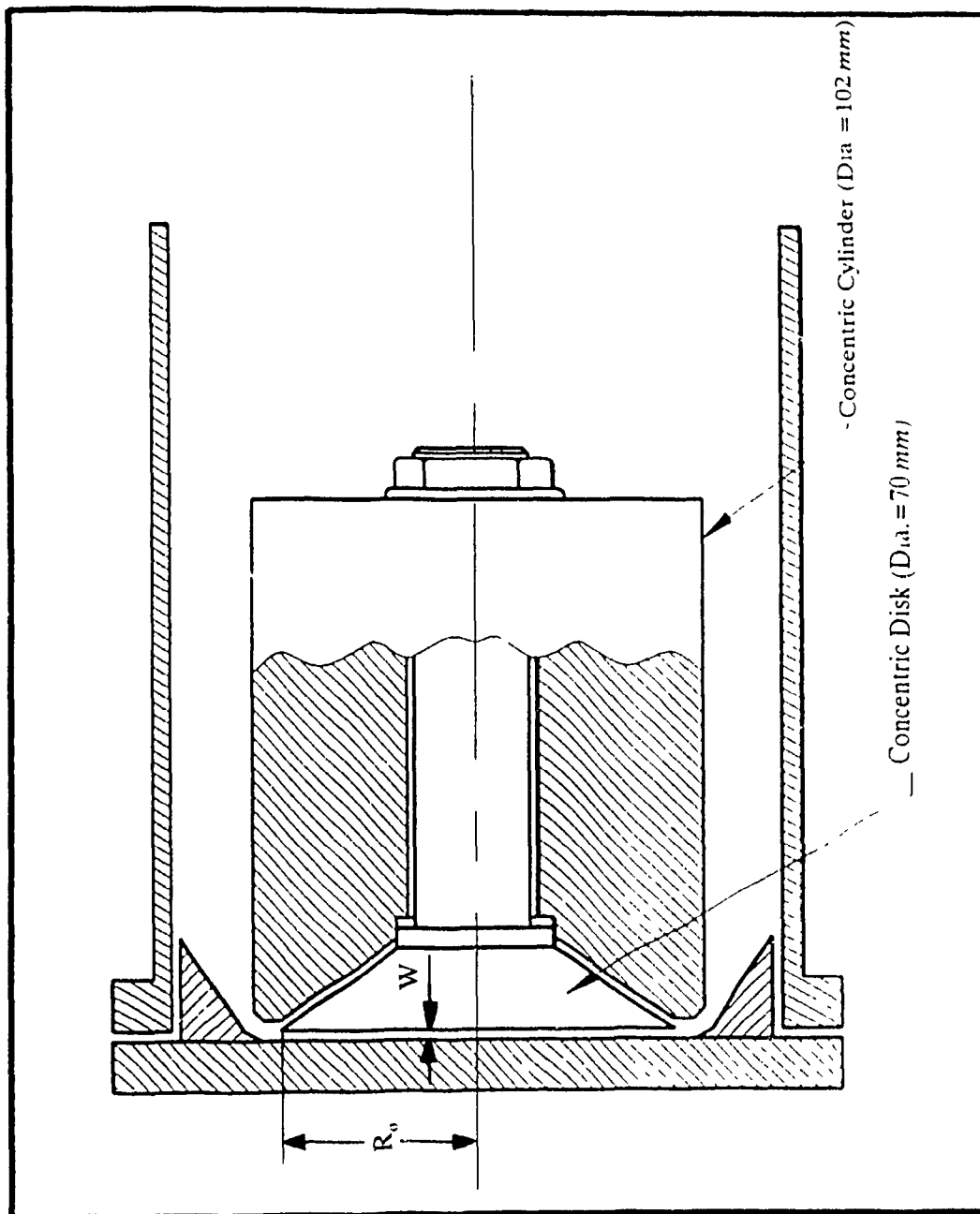


Figure 3.7. A schematic diagram of the test section (new model)

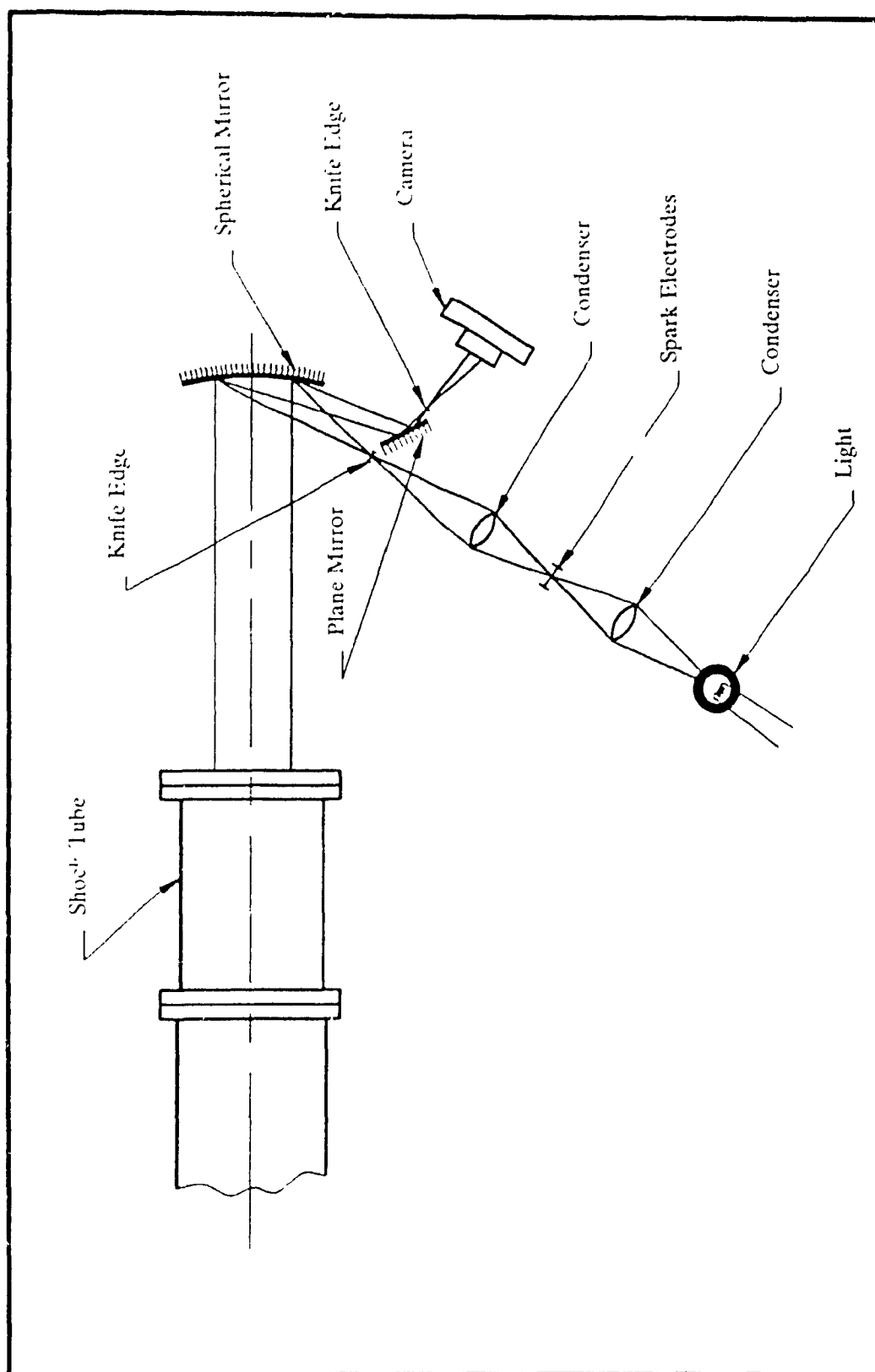


Figure 3.8. A schematic diagram of the schlieren photography system

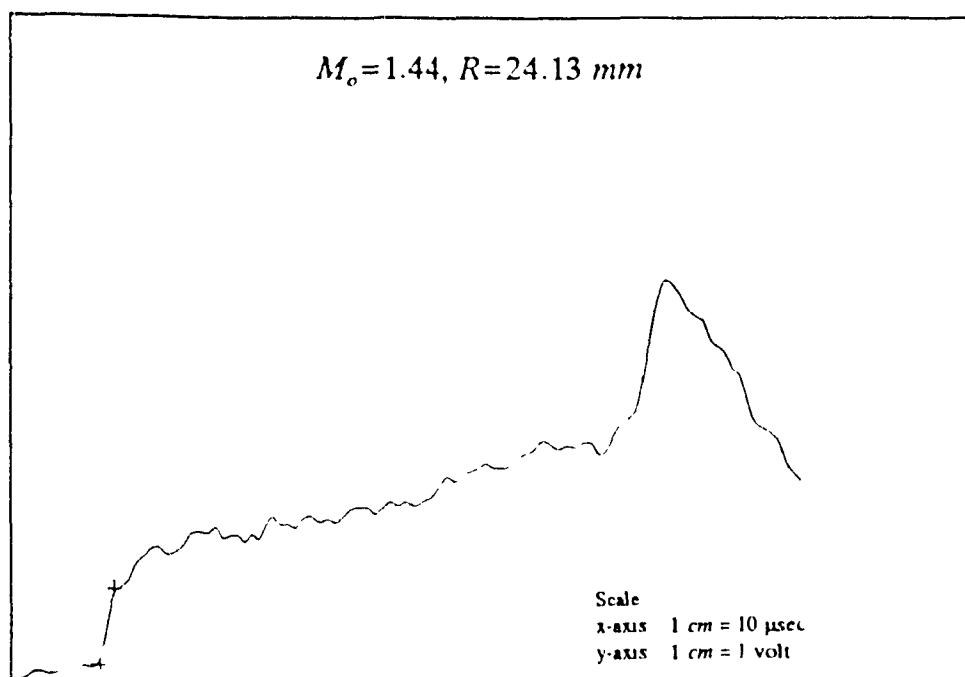


Figure 4.1a

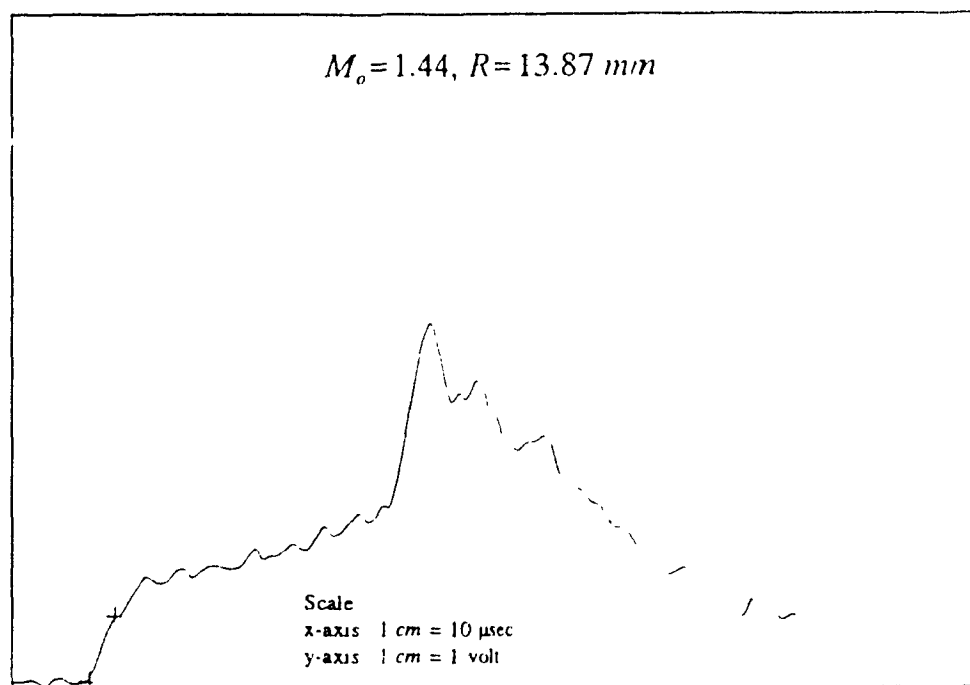


Figure 4.1b

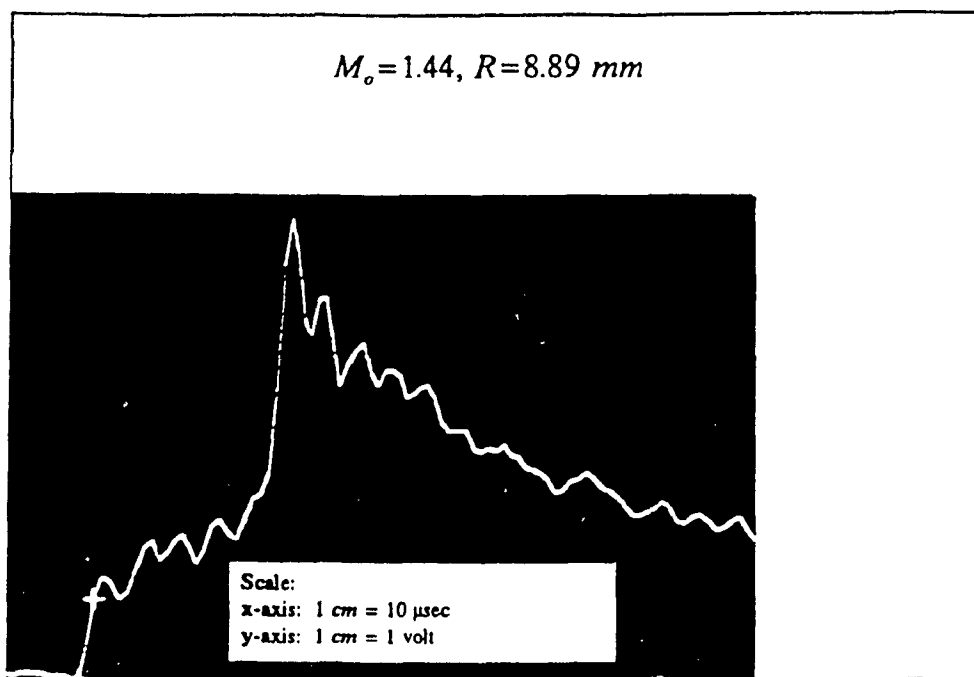


Figure 4.1c

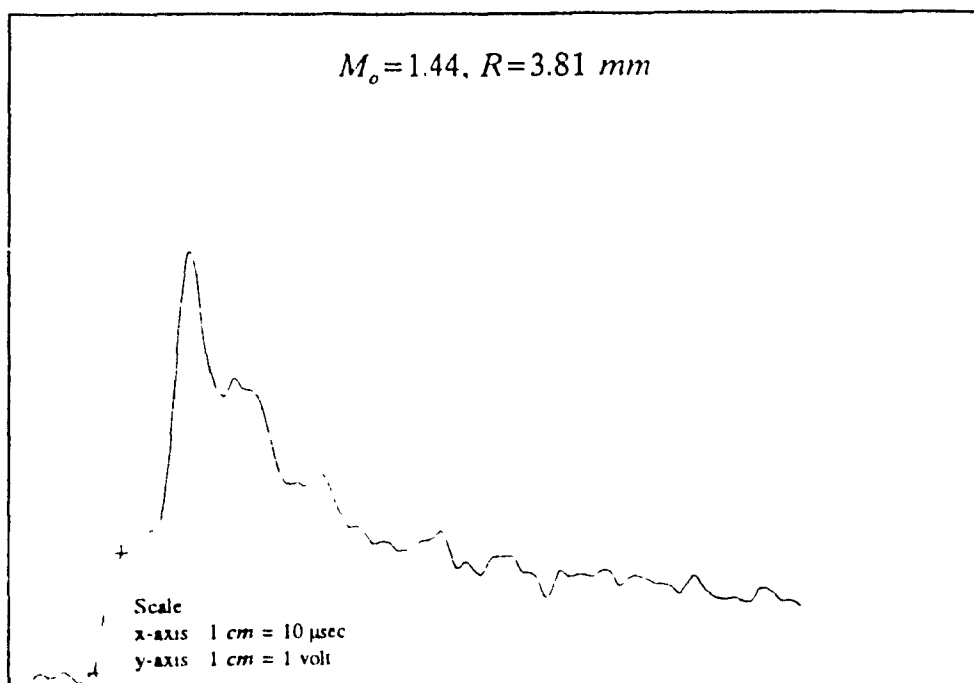


Figure 4.1d

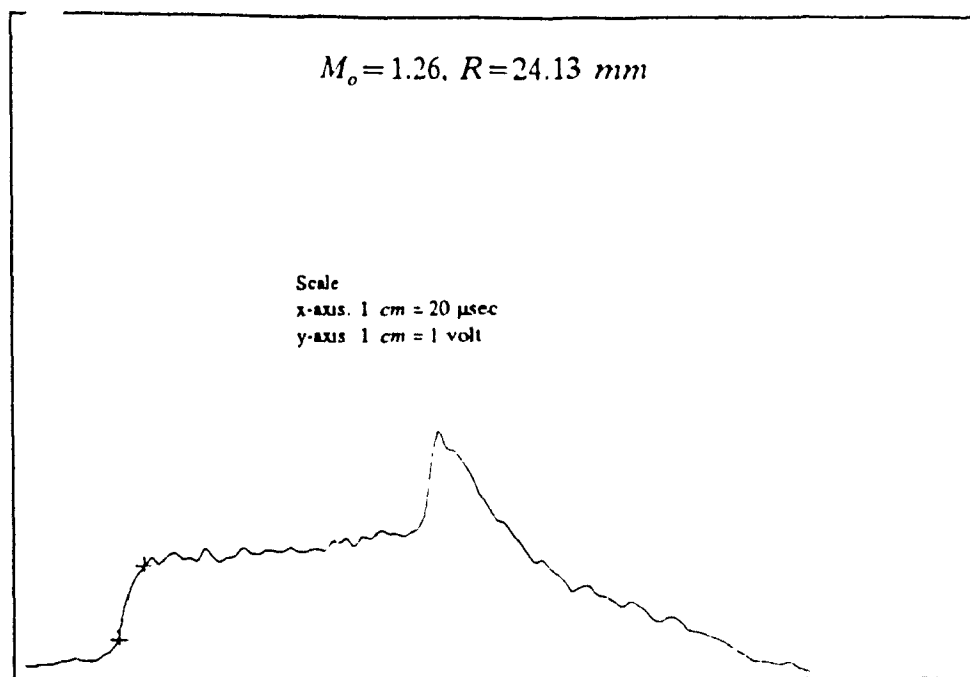


Figure 4.1e

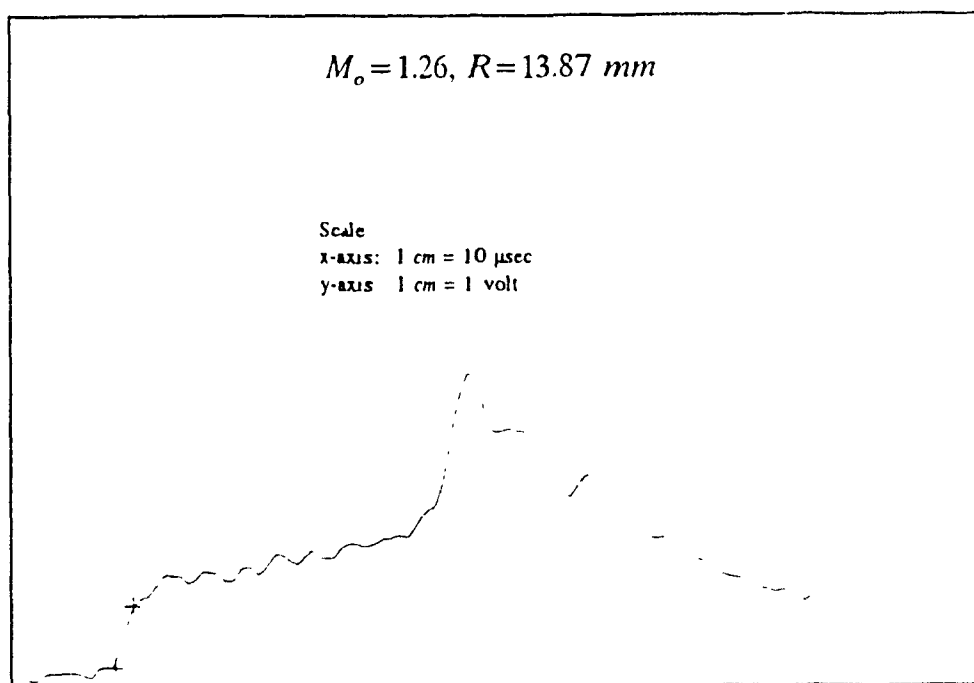


Figure 4.1f

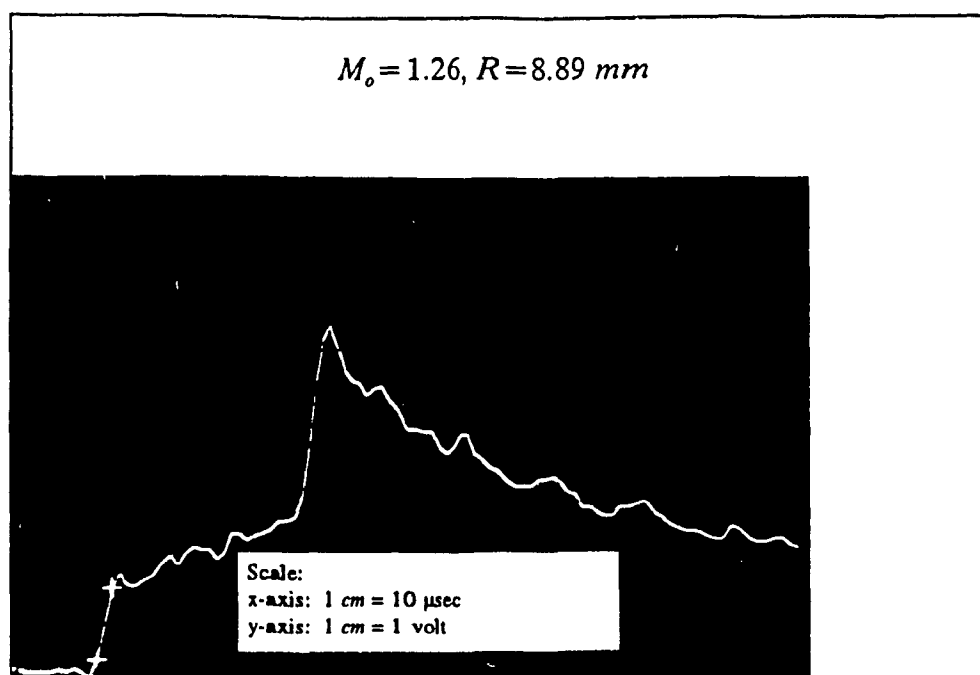


Figure 4.1g

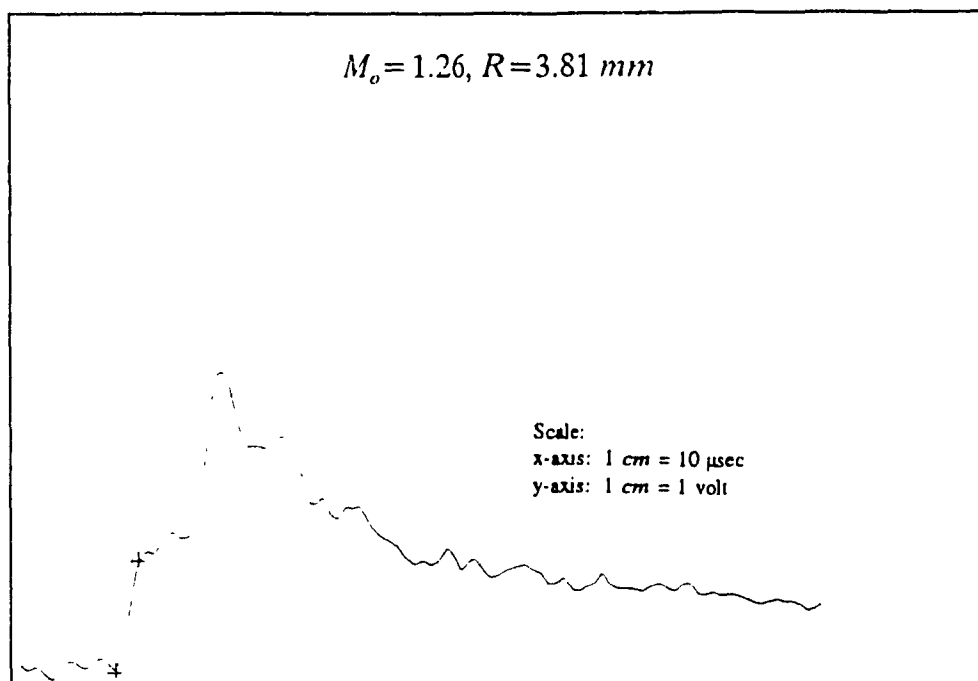


Figure 4.1h

Figure 4.1. Oscilloscope traces for $M_o = 1.44$ and $M_o = 1.26$ with $W' = 2.5 \text{ mm}$.

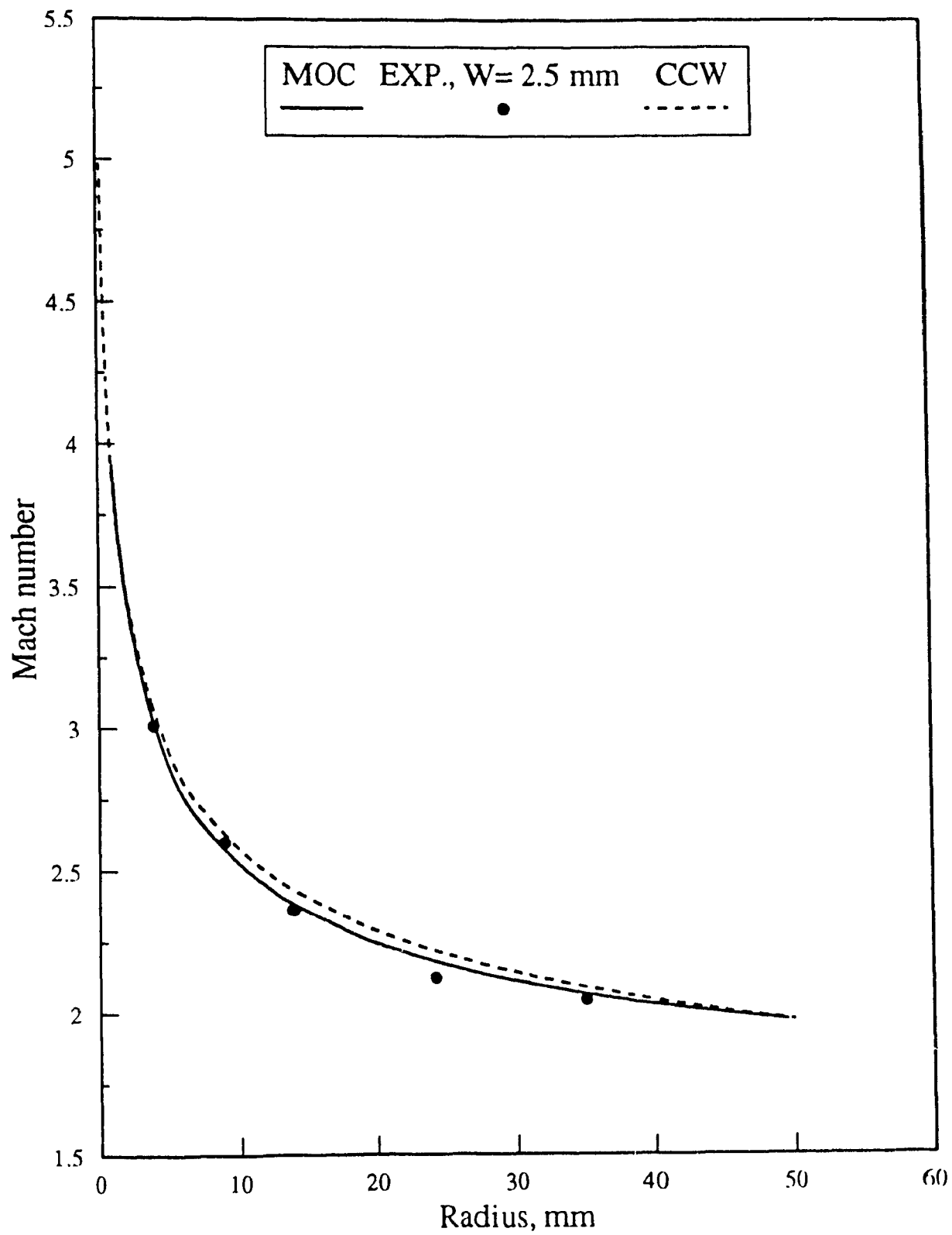


Figure 4.2. Shock Mach number versus radius for $M_e = 1.44$ and $W = 2.5 \text{ mm}$

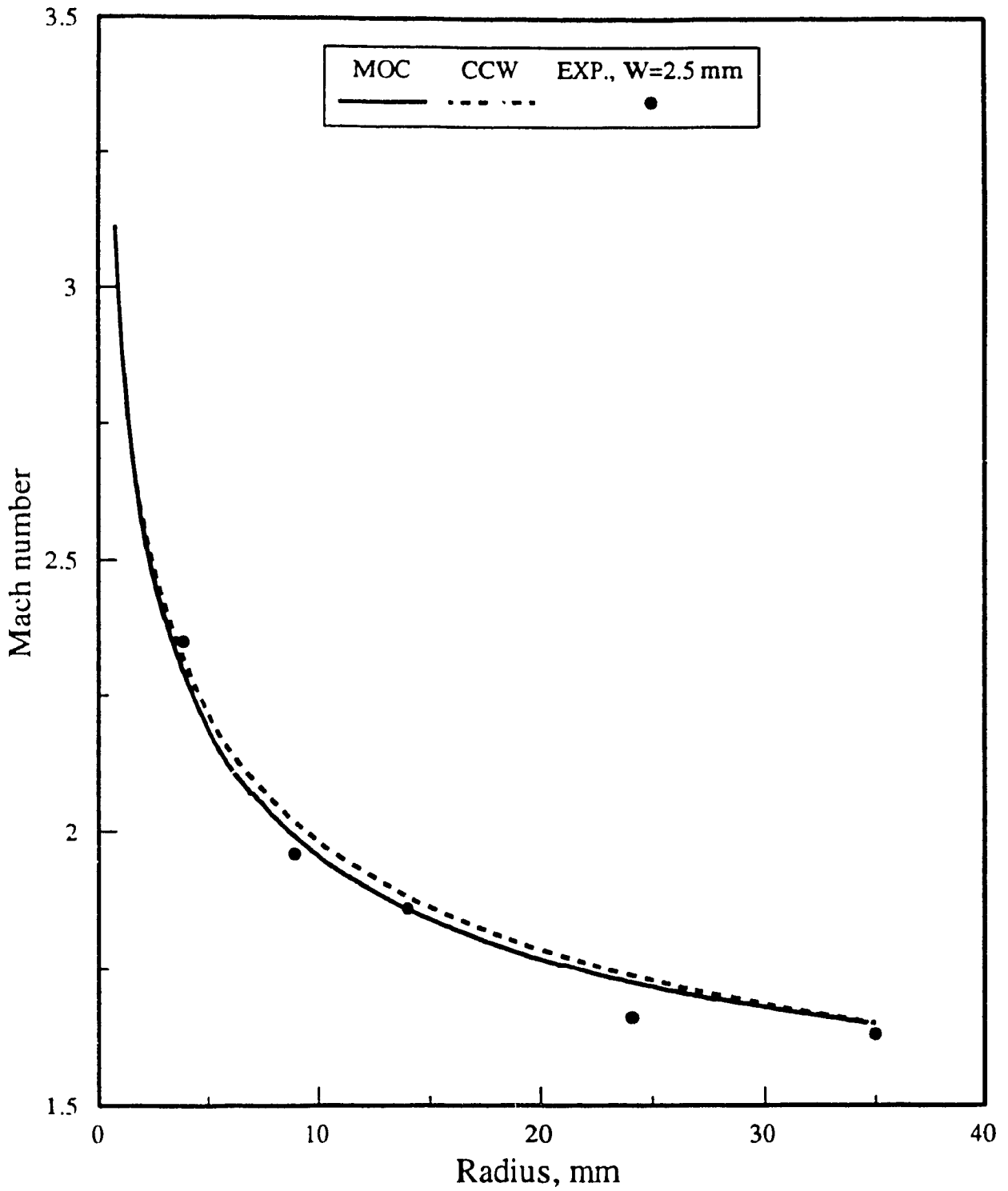


Figure 4.3. Shock Mach number versus radius for $M_o = 1.26$ and $W = 2.5$ mm.

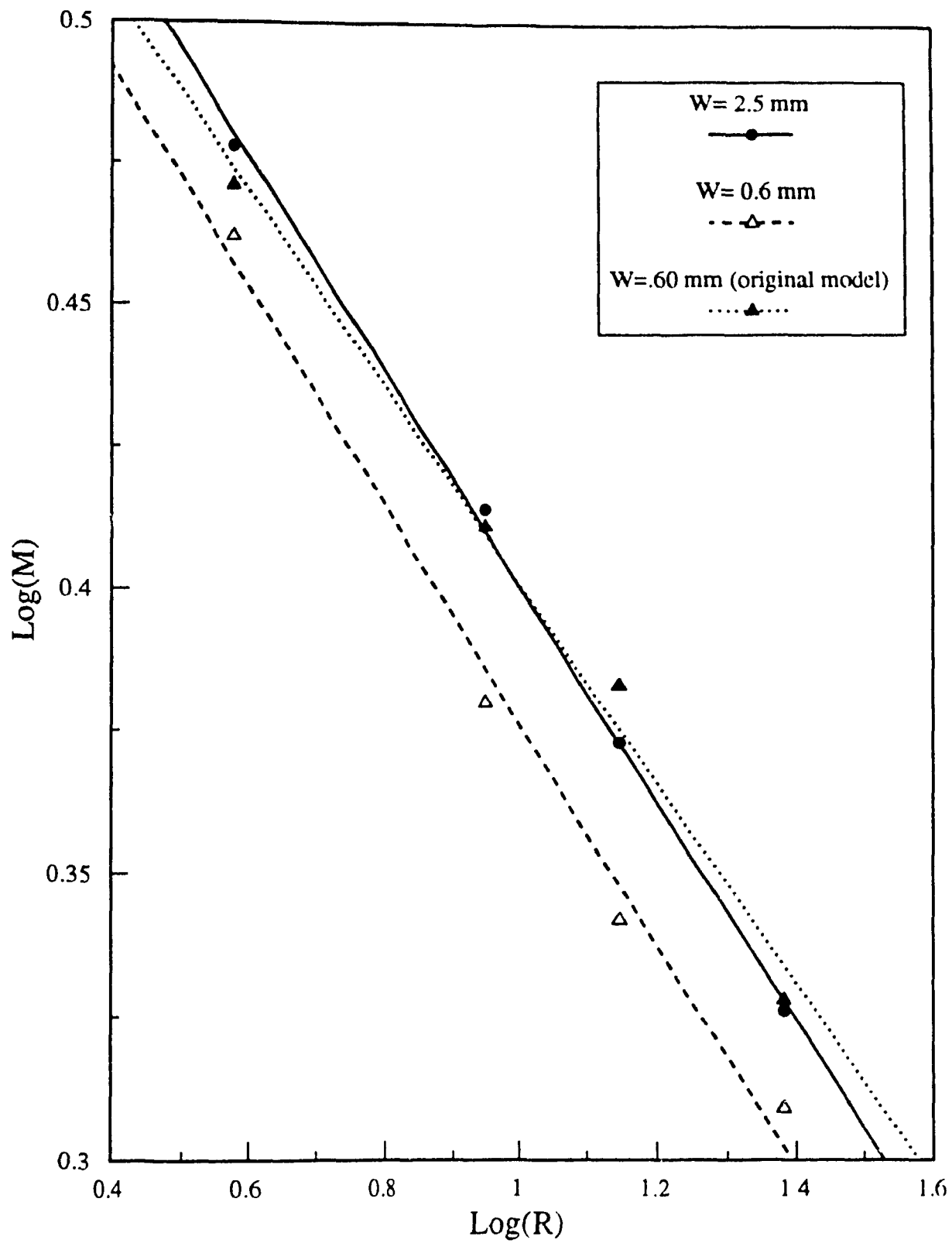


Figure 4.4. Shock Mach number versus radius for $M_o=1.44$ in Log-Log scale

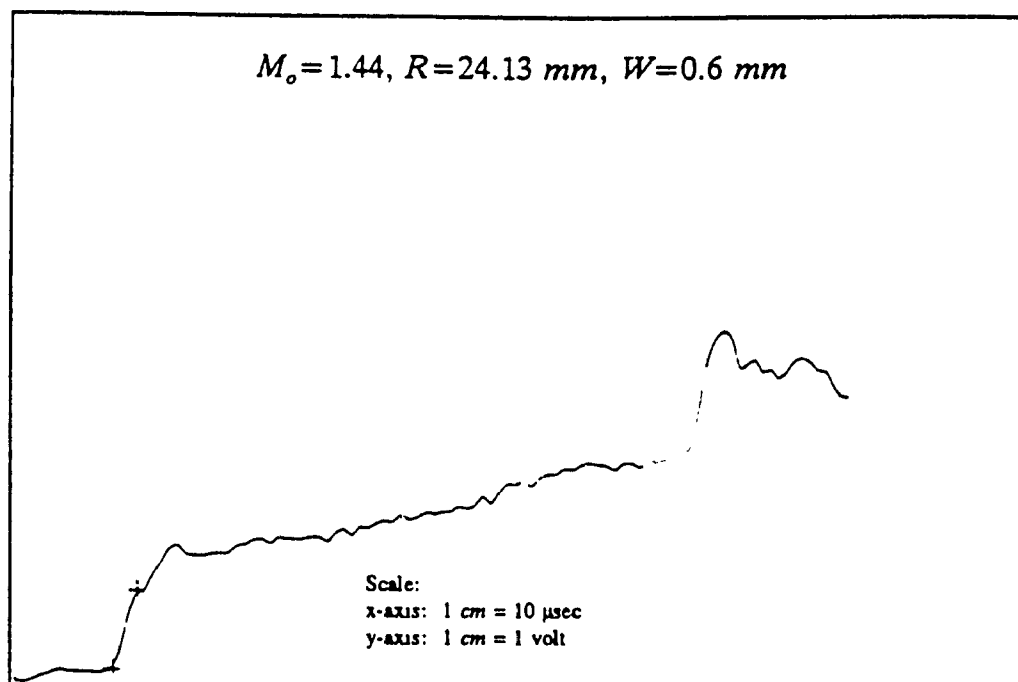


Figure 4.5a

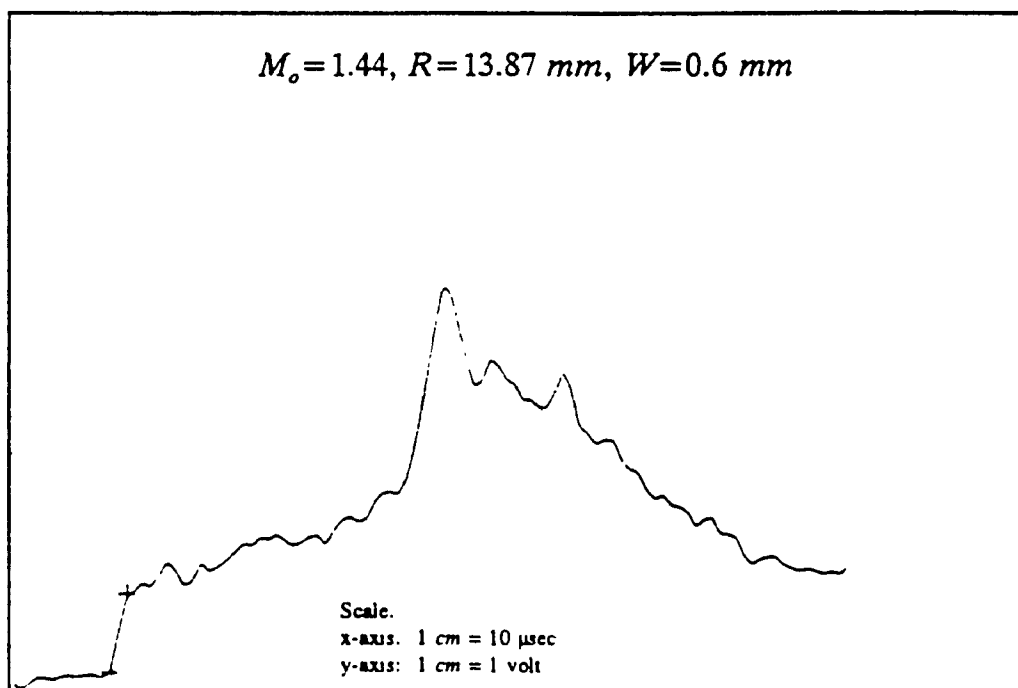


Figure 4.5b

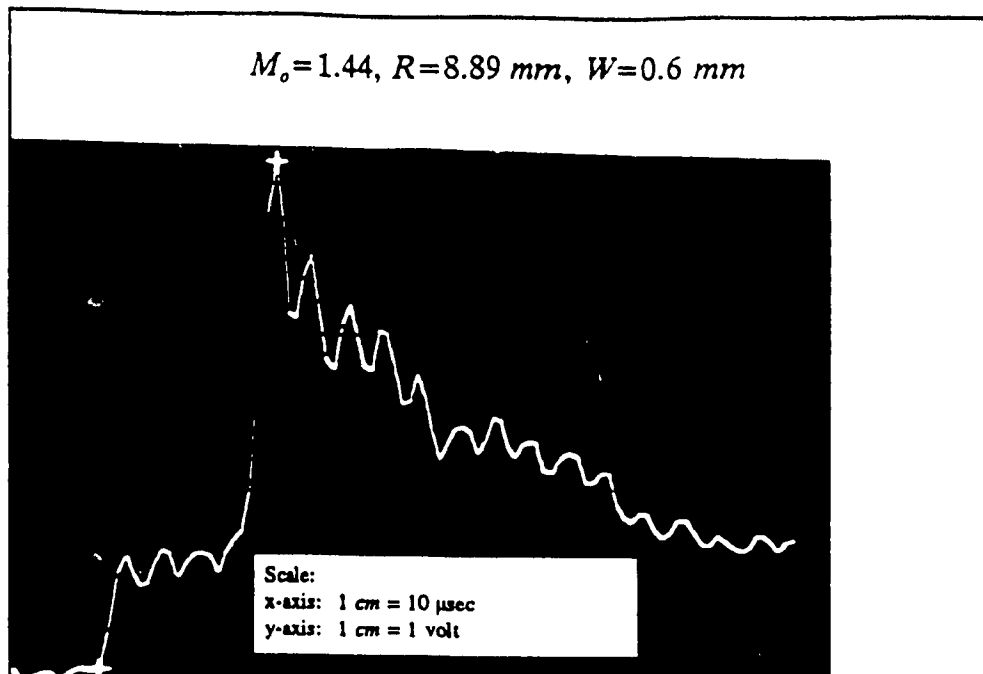


Figure 4.5c

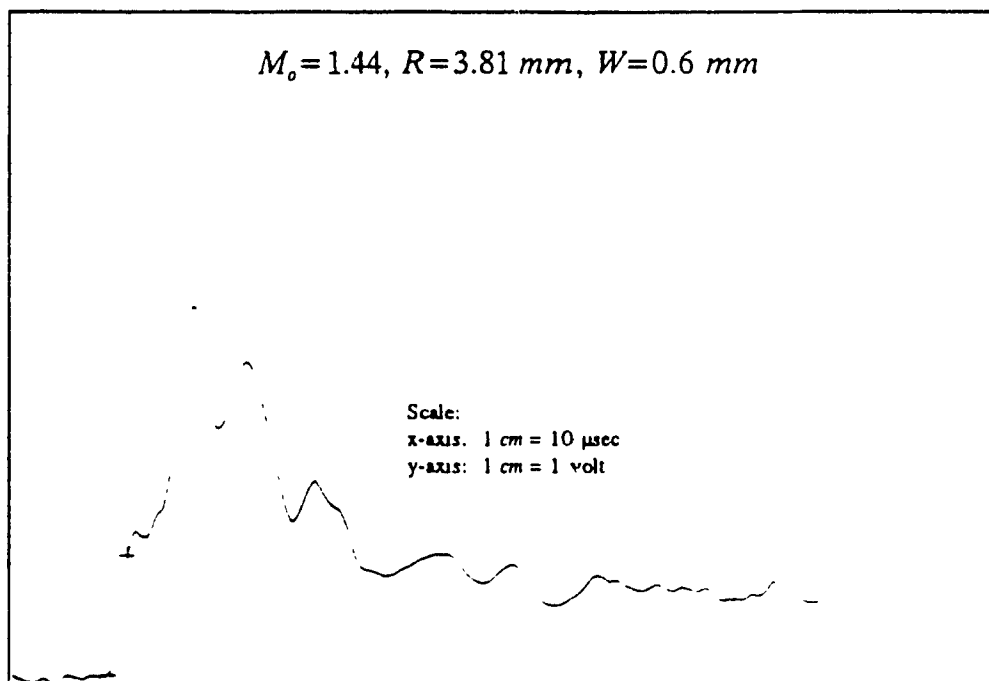


Figure 4.5d

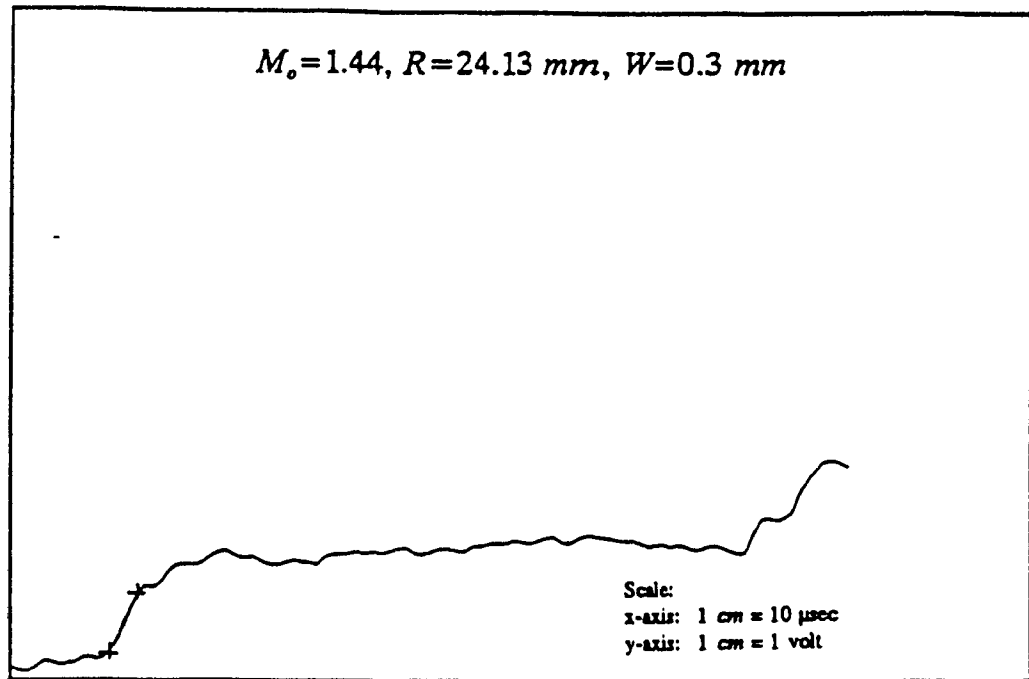


Figure 4.5e

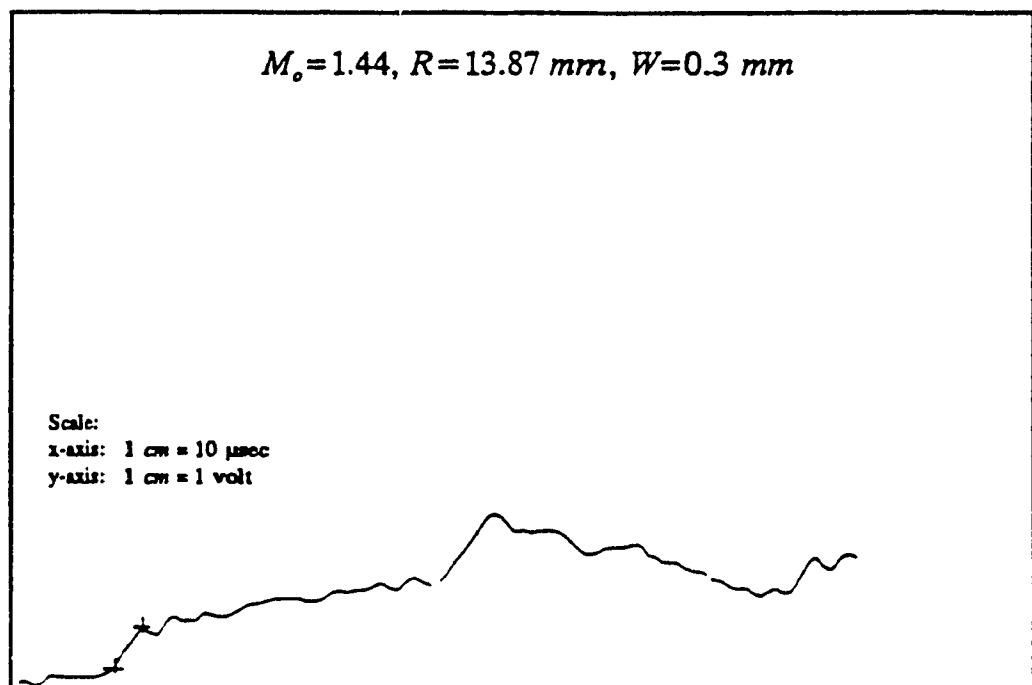


Figure 4.5f

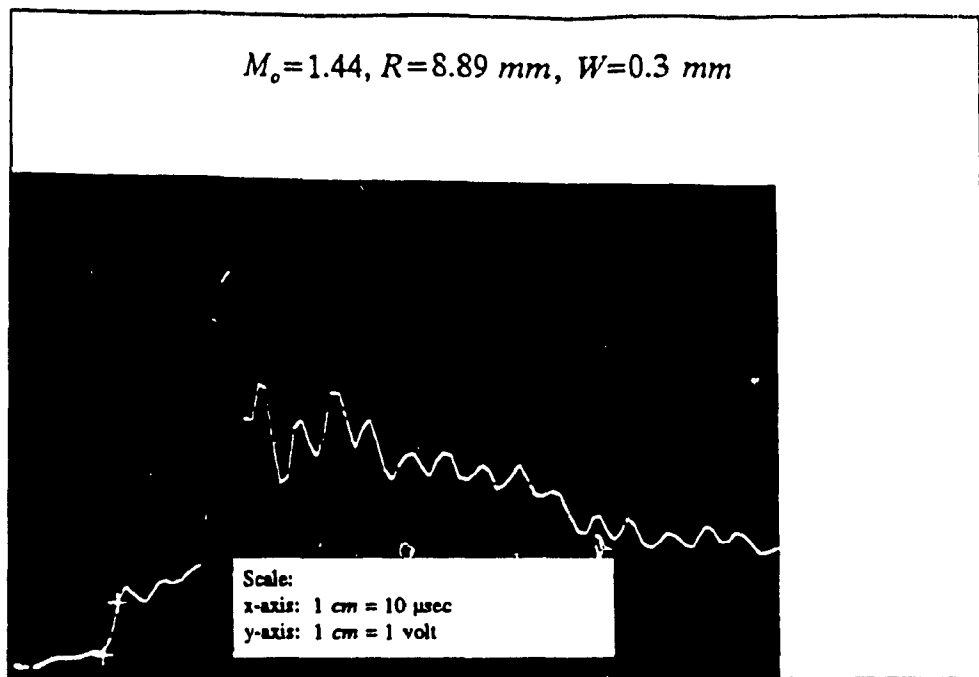


Figure 4.5g

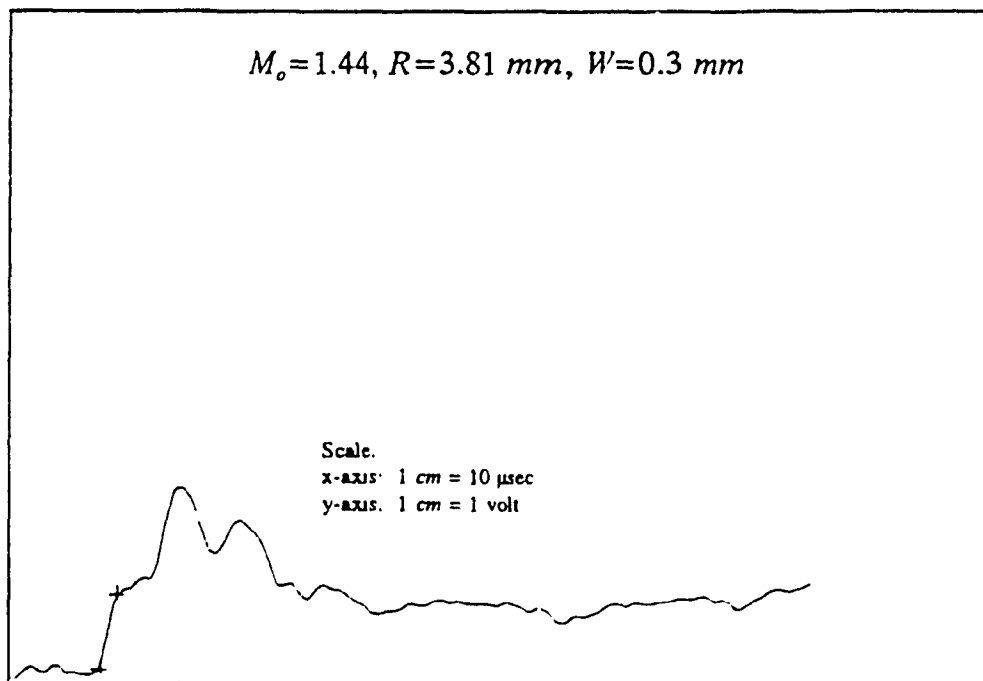


Figure 4.5h

Figure 4.5 Oscilloscope traces for $M_o=1.44, R=24.13 \text{ mm}, 13.87 \text{ mm}, 8.89 \text{ mm}$ and $3.81 \text{ mm}, W=0.6 \text{ mm}$ and 0.3 mm .

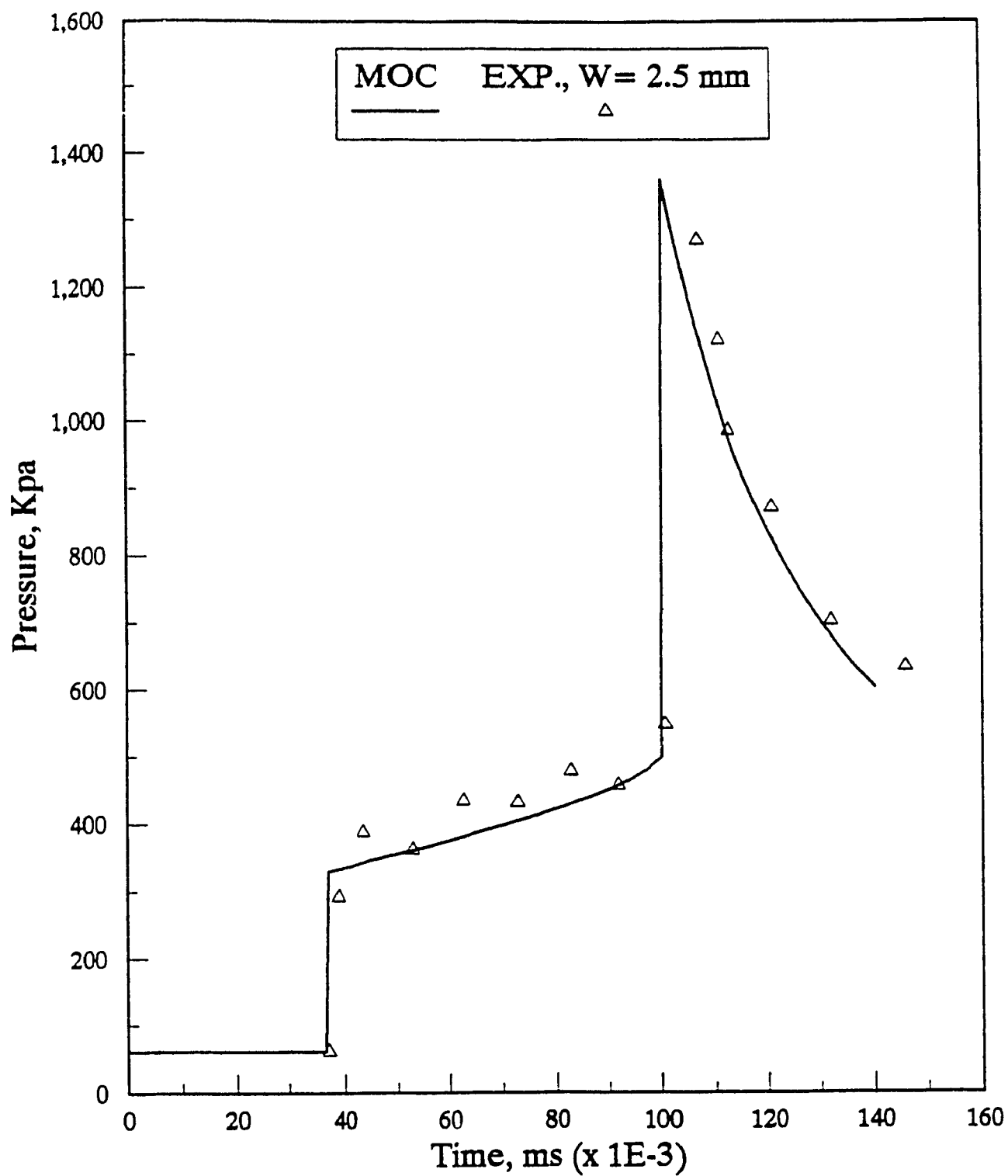


Figure 4.6. Pressure history for $M_o = 1.44$, $W=2.5$ mm and $R=24.13$ mm, comparison of the experiments with the results obtained using the method of characteristics.

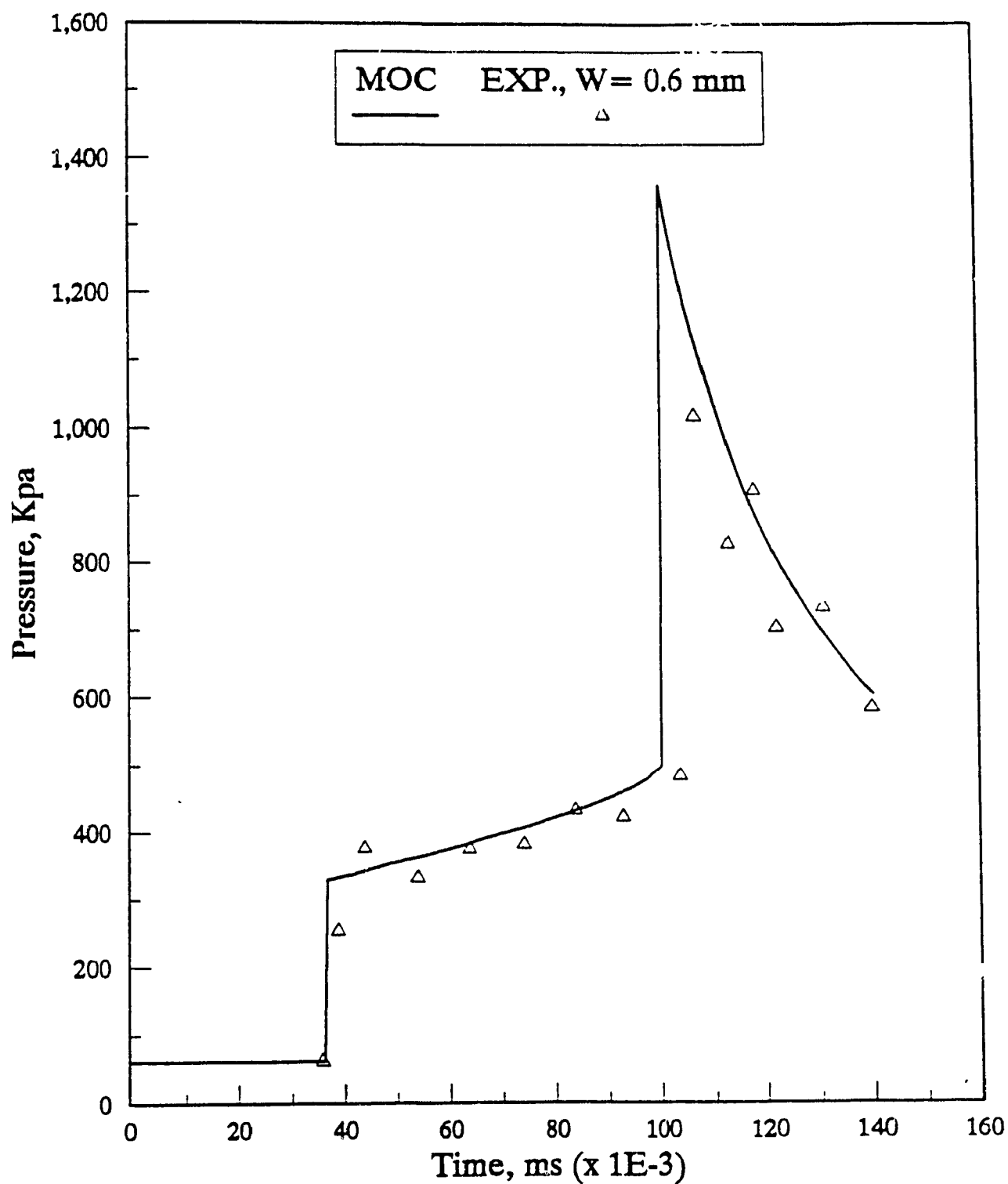


Figure 4.7. Pressure history for $M_o = 1.44$, $W=0.6$ mm and $R=24.13$ mm, comparison of the experiments with the results obtained using the method of characteristics.

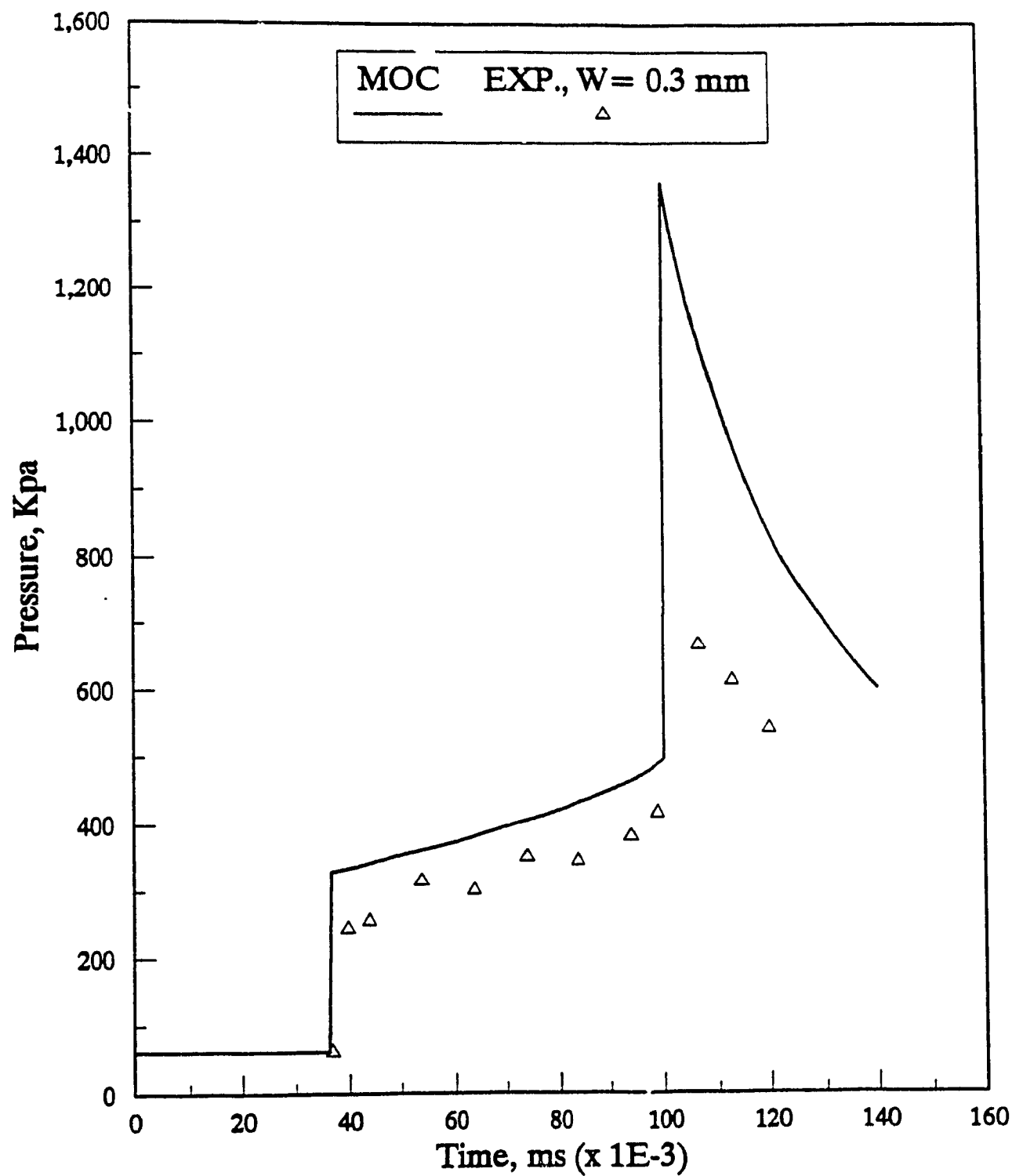


Figure 4.8. Pressure history for $M_o = 1.44$, $W = 0.3 \text{ mm}$ and $R = 24.13 \text{ mm}$, comparison of the experiments with the results obtained using the method of characteristics.

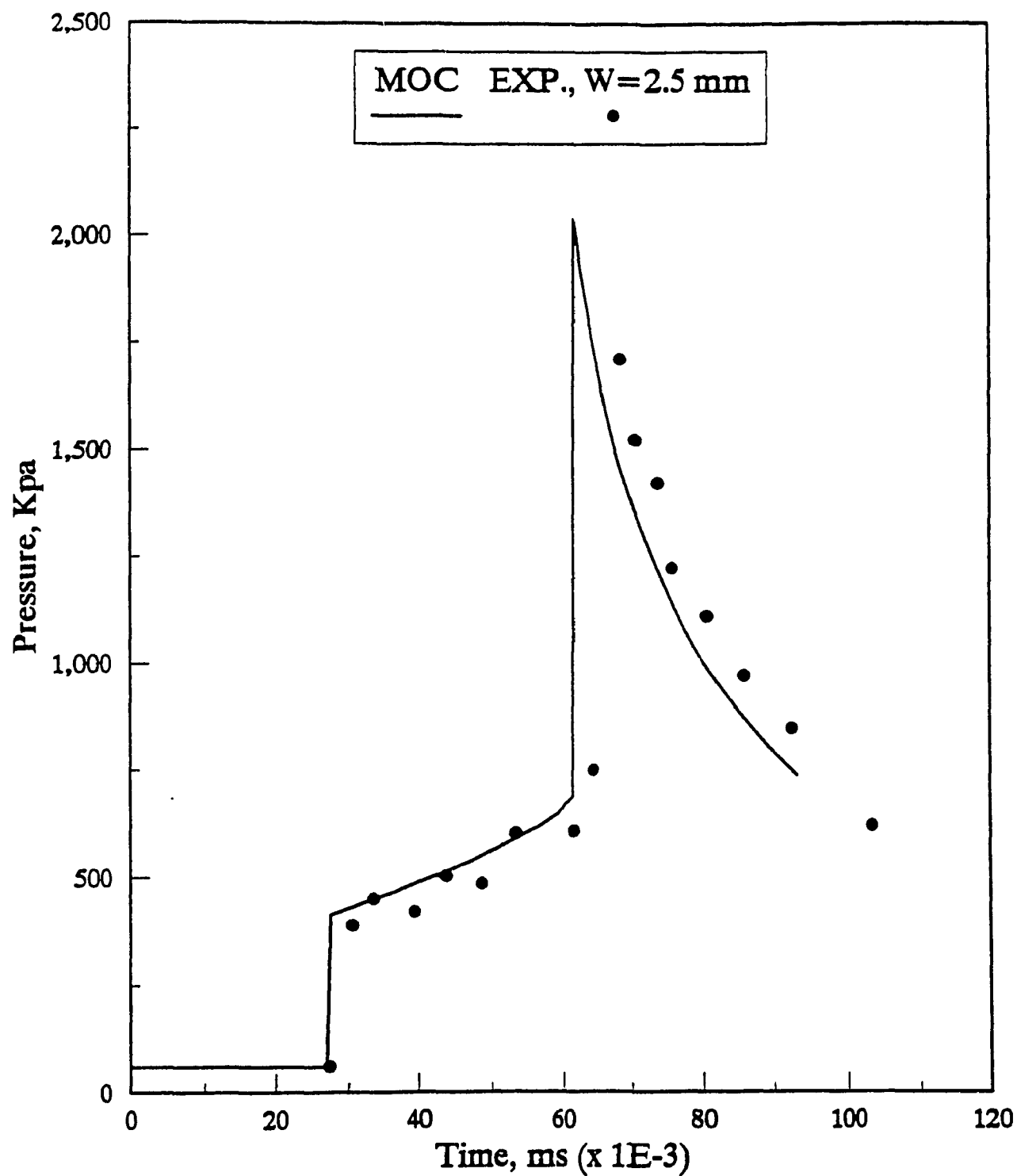


Figure 4.9. Pressure history for $M_o=1.44$, $W=2.5$ mm and $R=13.87$ mm, comparison of the experiments with the results obtained using the method of characteristics.

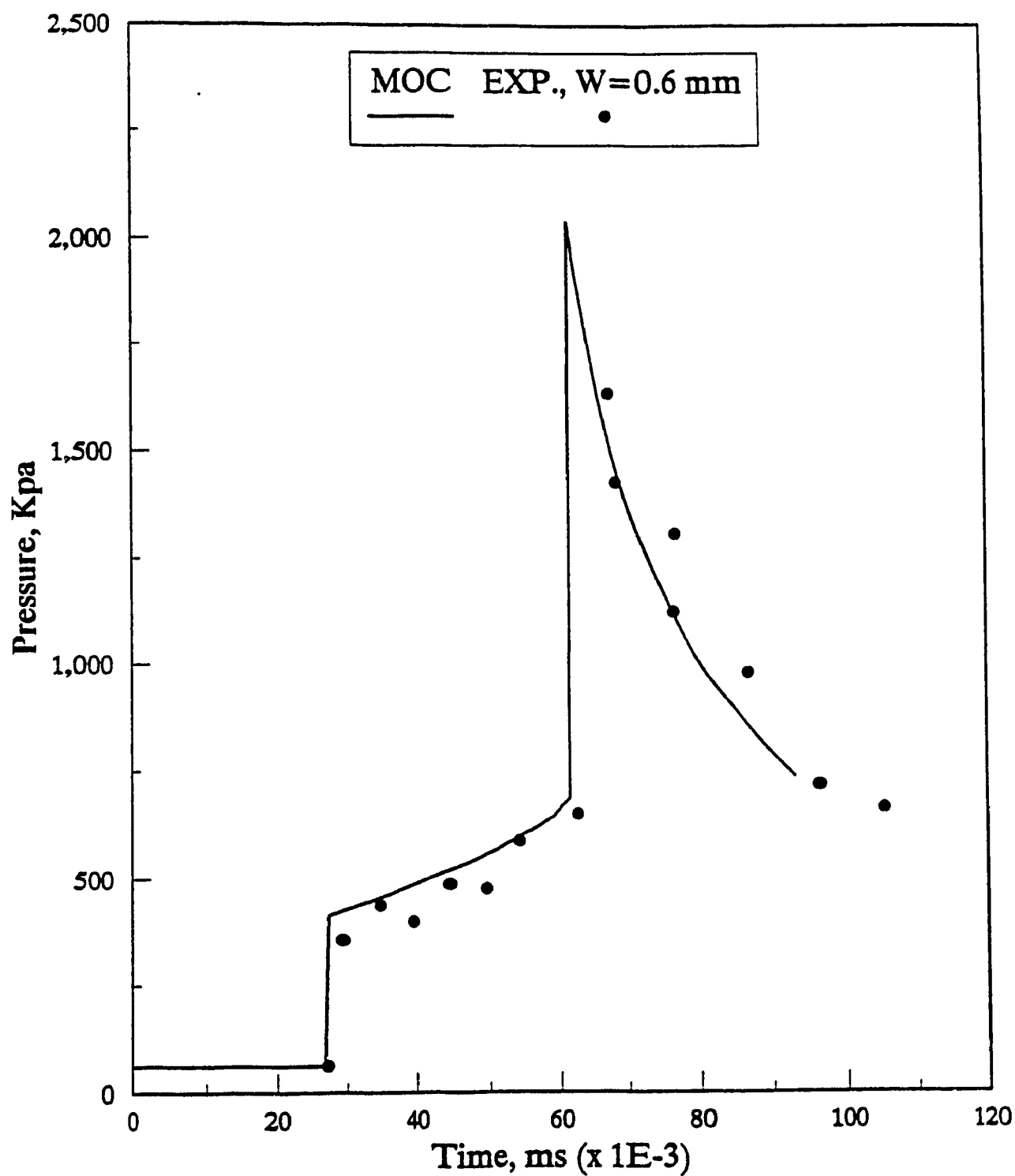


Figure 4.10. Pressure history for $M_o=1.44$, $W=0.6$ mm and $R=13.87$ mm, comparison of the experiments with the results obtained using the method of characteristics.

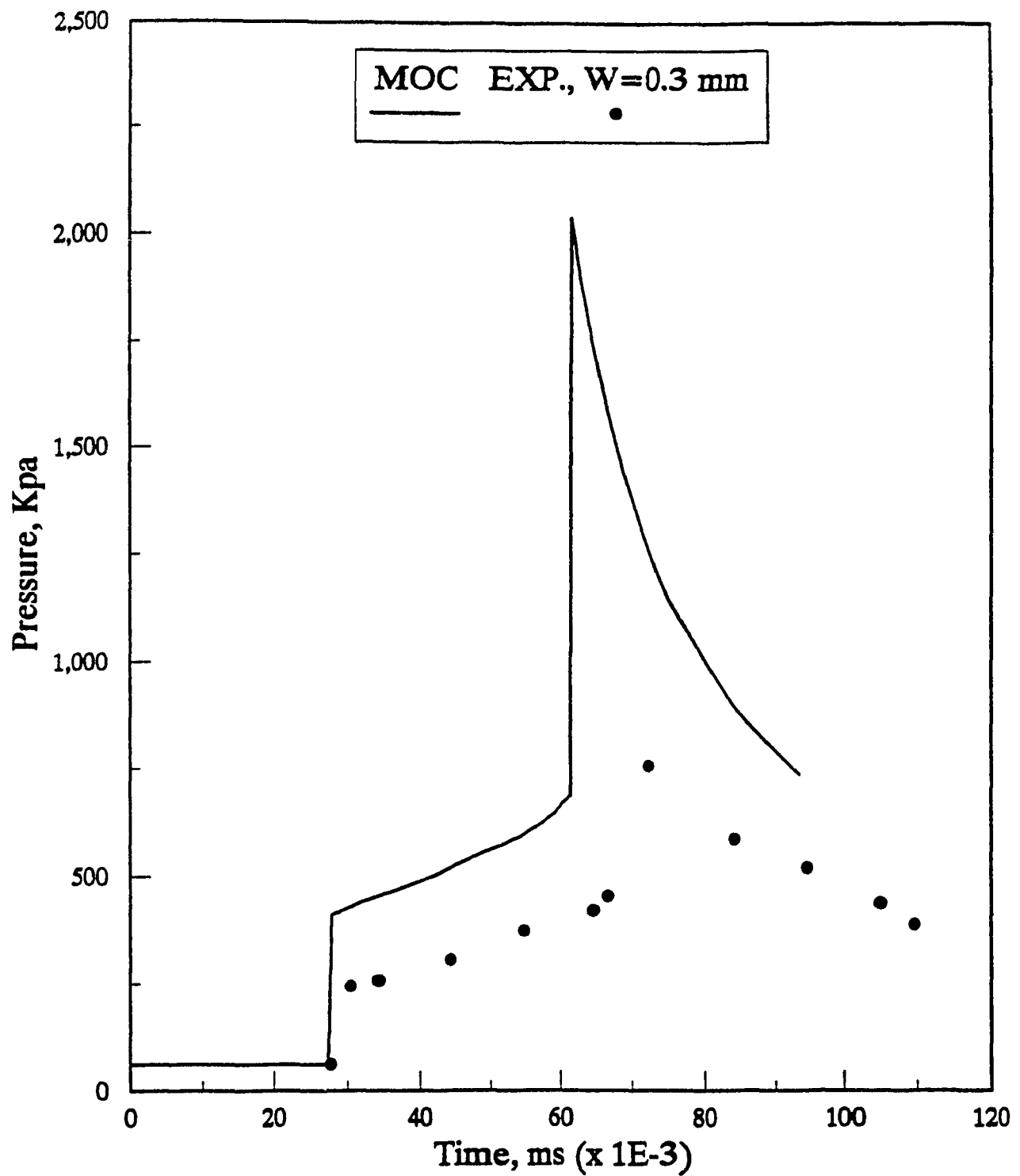


Figure 4.11. Pressure history for $M_o=1.44$, $W=0.3$ mm and $R=13.87$ mm, comparison of the experiments with the results obtained using the method of characteristics.

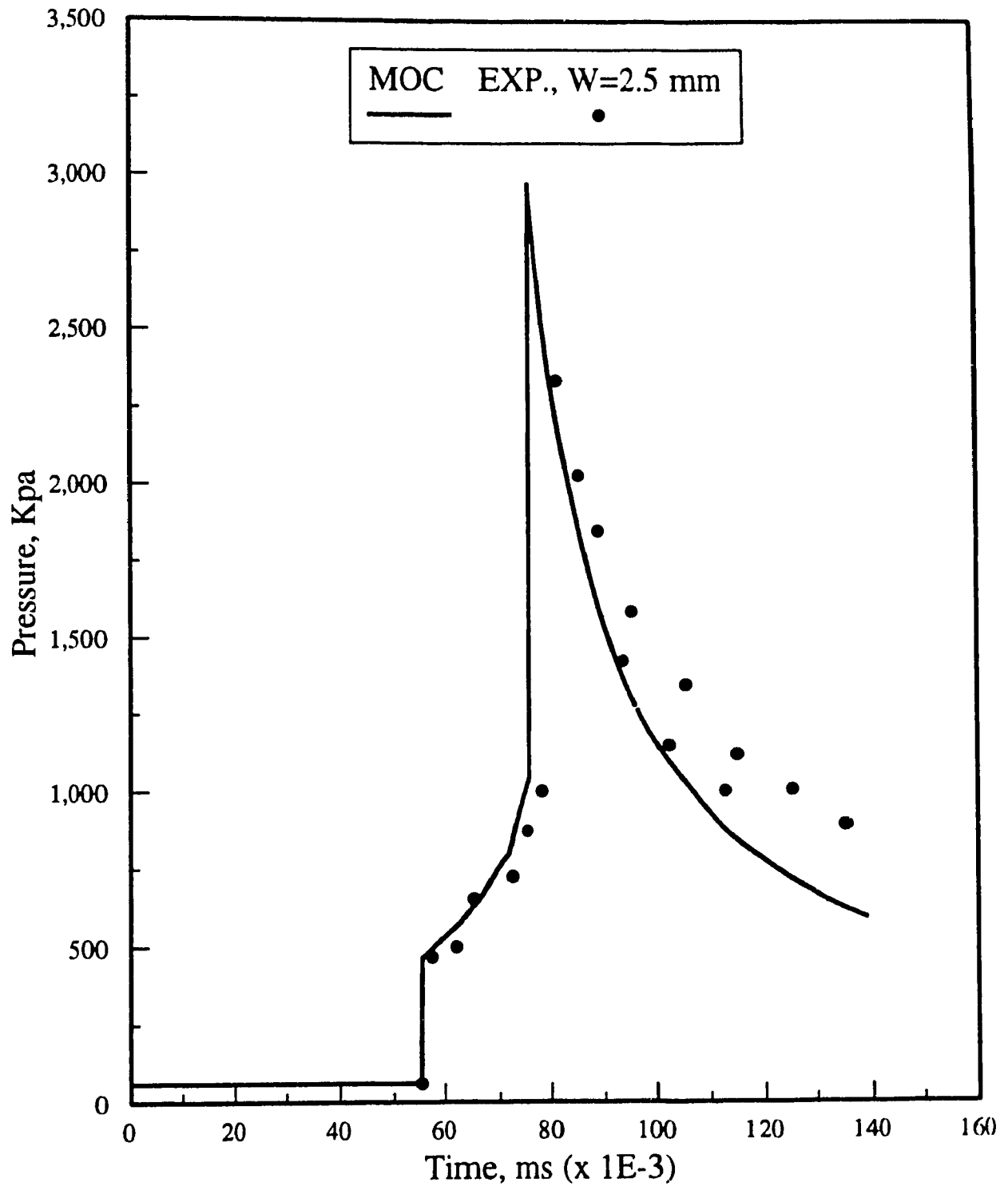


Figure 4.12. Pressure history for $M_o=1.44$, $W=2.5$ mm and $R=8.89$ mm, comparison of the experiments with the results obtained using the method of characteristics.

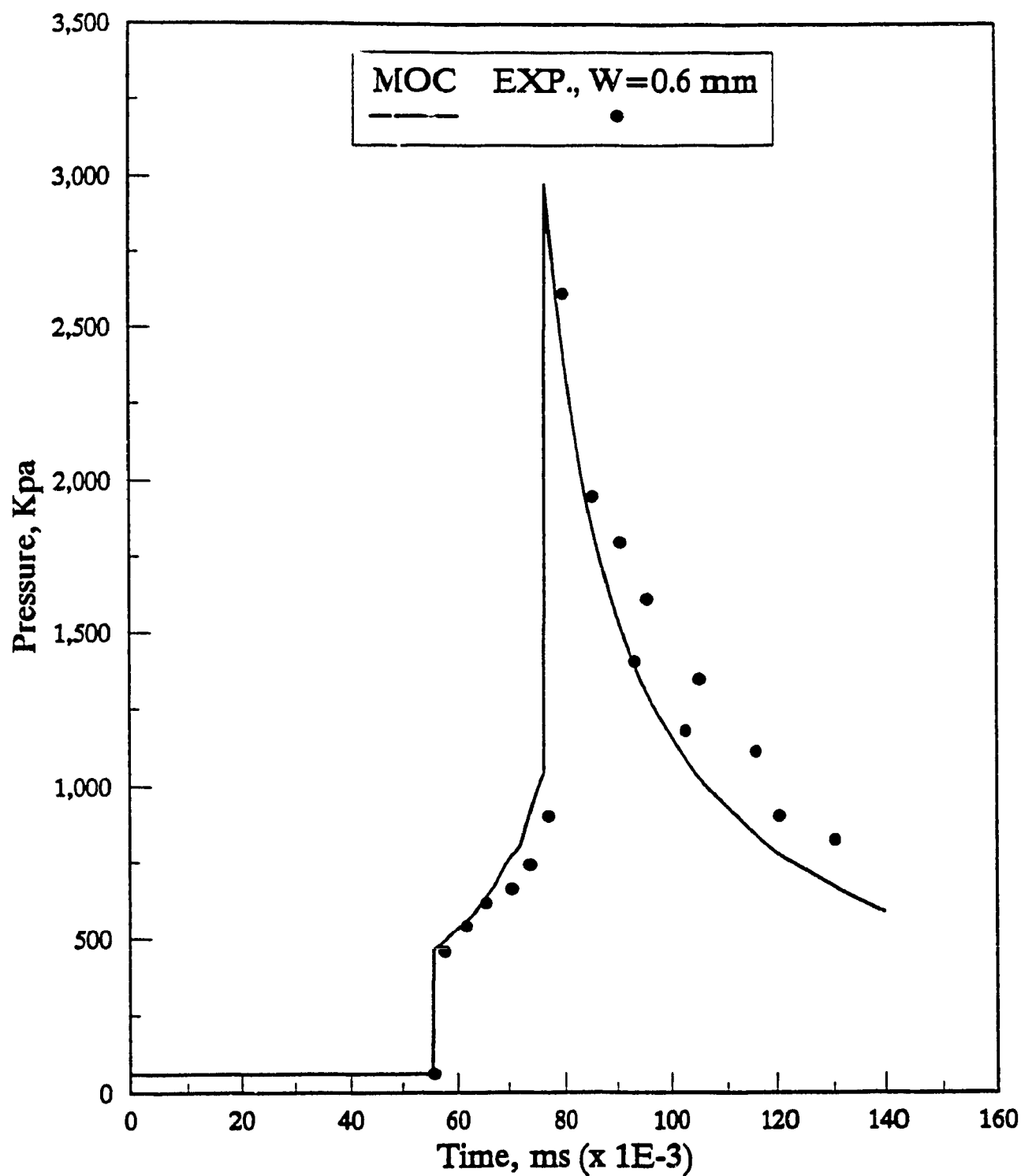


Figure 4.13. Pressure history for $M_o=1.44$, $W=0.6$ mm and $R=8.89$ mm, comparison of the experiments with the results obtained using the method of characteristics.

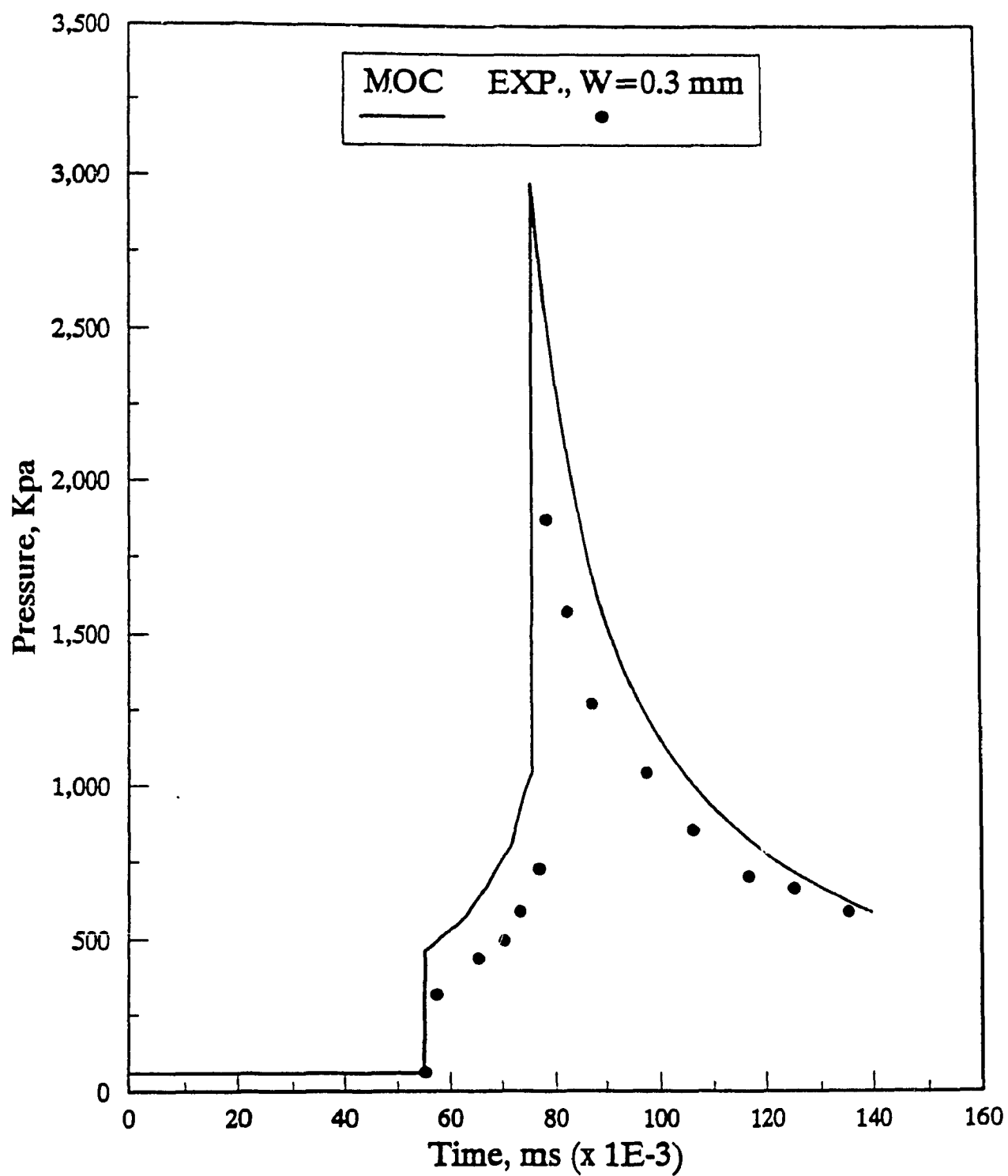


Figure 4.14. Pressure history for $M_o=1.44$, $W=0.3$ mm and $R=8.89$ mm, comparison of the experiments with the results obtained using the method of characteristics.

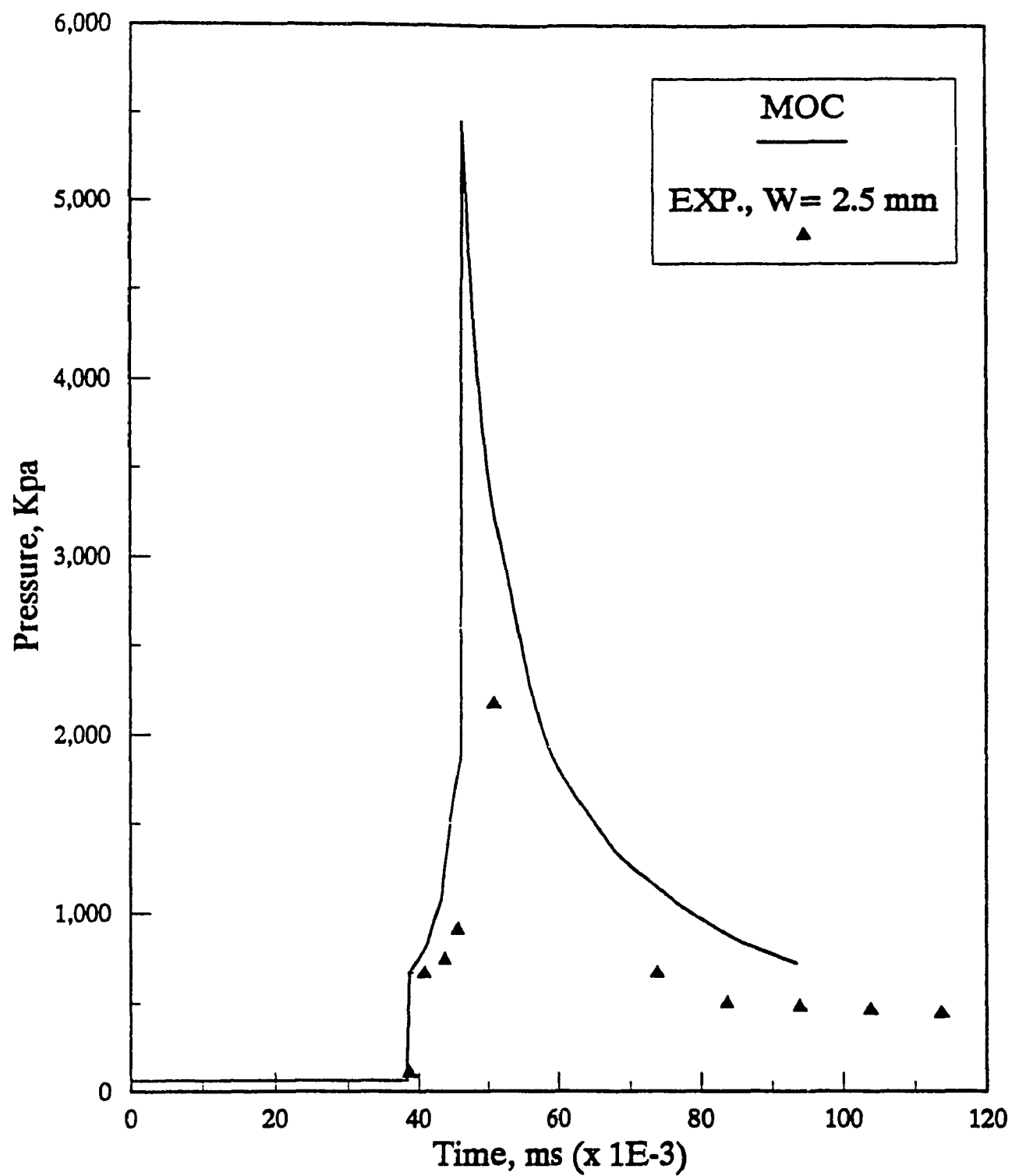


Figure 4.15. Pressure history for $M_o=1.44$, $W=2.5$ mm and $R=3.81$ mm, comparison of the experiments with the results obtained using the method of characteristics.

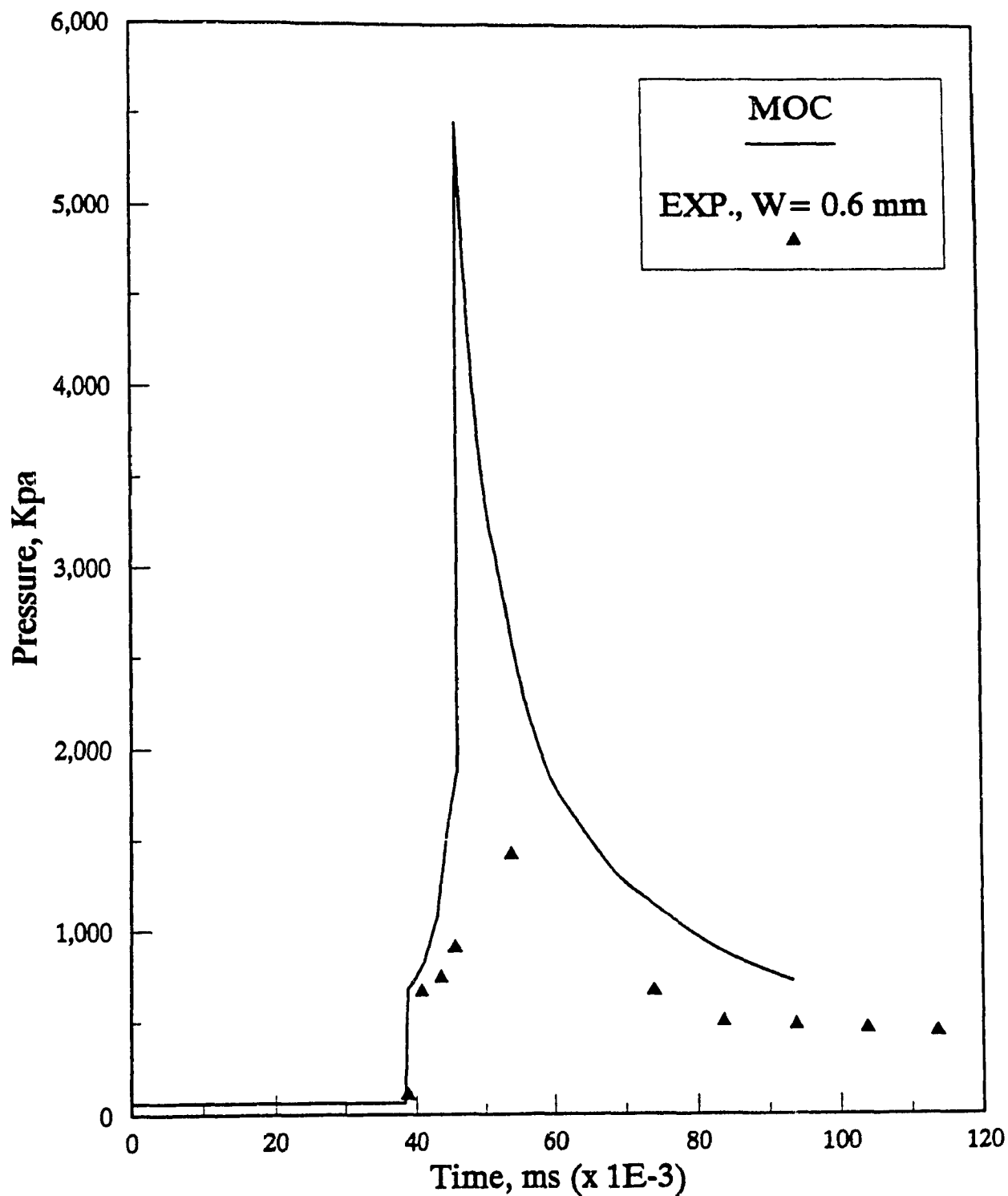


Figure 4.16. Pressure history for $M_o=1.44$, $W=0.6$ mm and $R=3.81$ mm, comparison of the experiments with the results obtained using the method of characteristics.

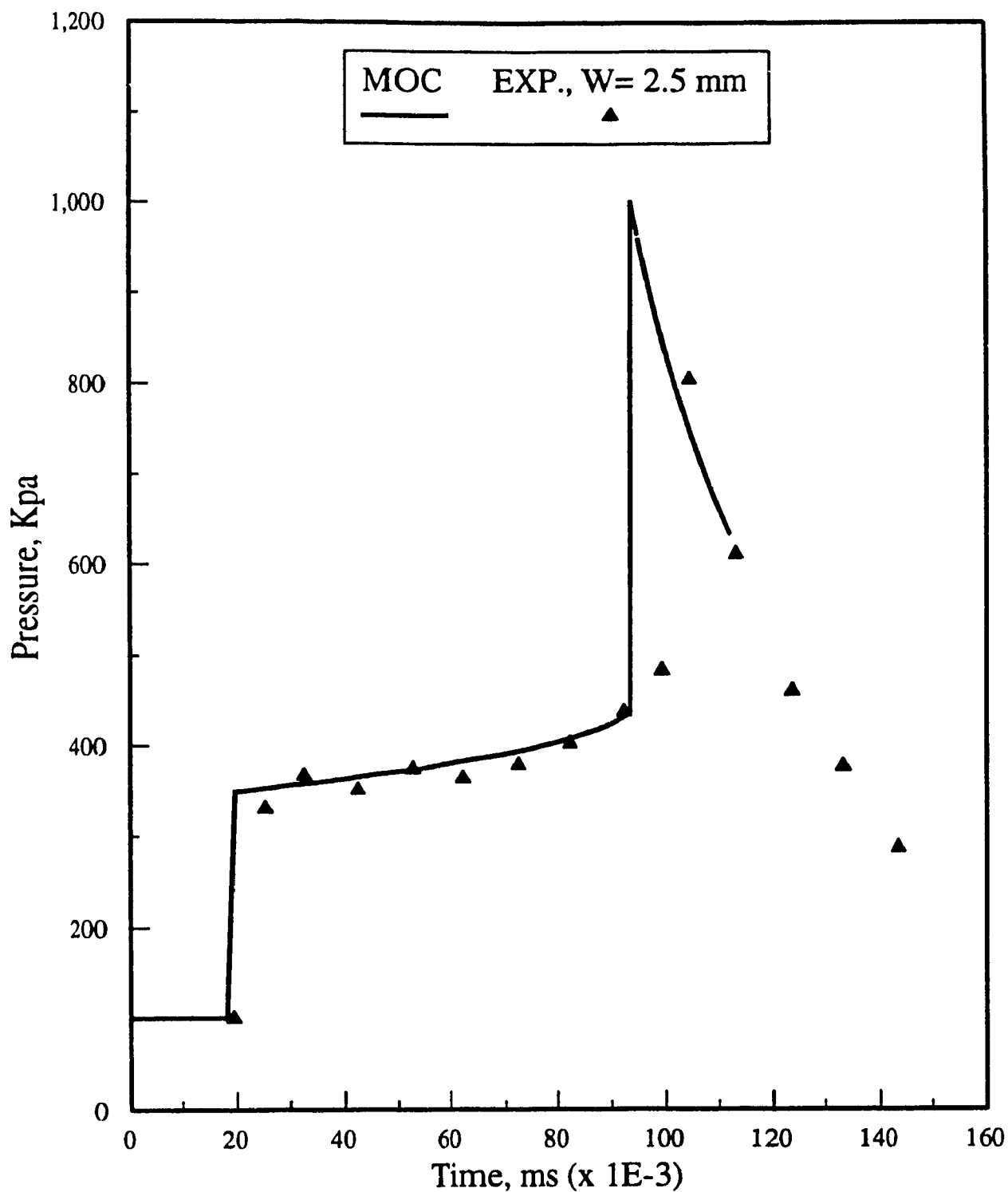


Figure 4.17. Pressure history for $M_o=1.26$, $W=2.5$ mm and $R=24.13$ mm, comparison of the experiments with the results obtained using the method of characteristics.

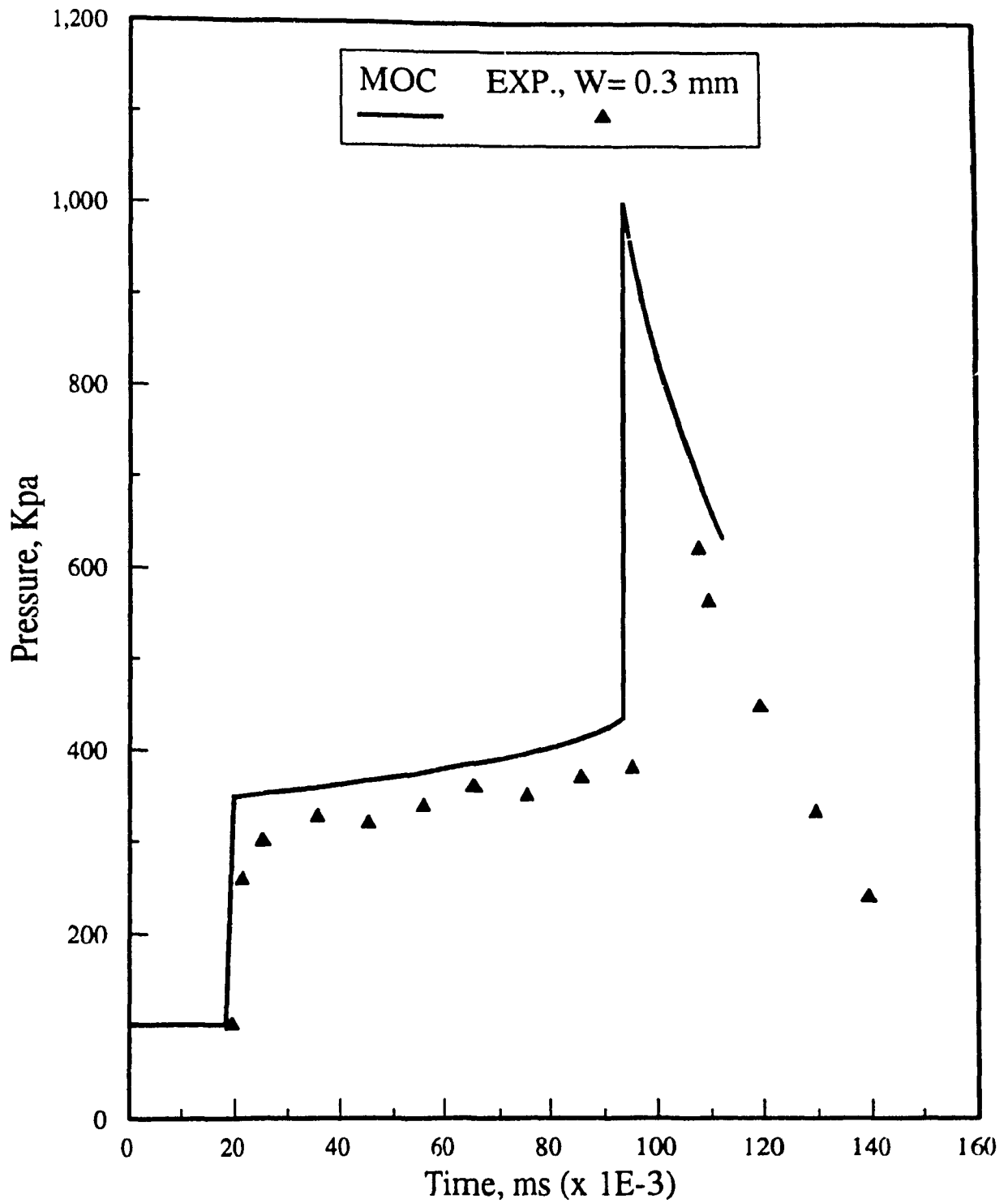


Figure 4.18. Pressure history for $M_o=1.26$, $W=0.30$ mm and $R=24.13$ mm, comparison of the experiments with the results obtained using the method of characteristics.

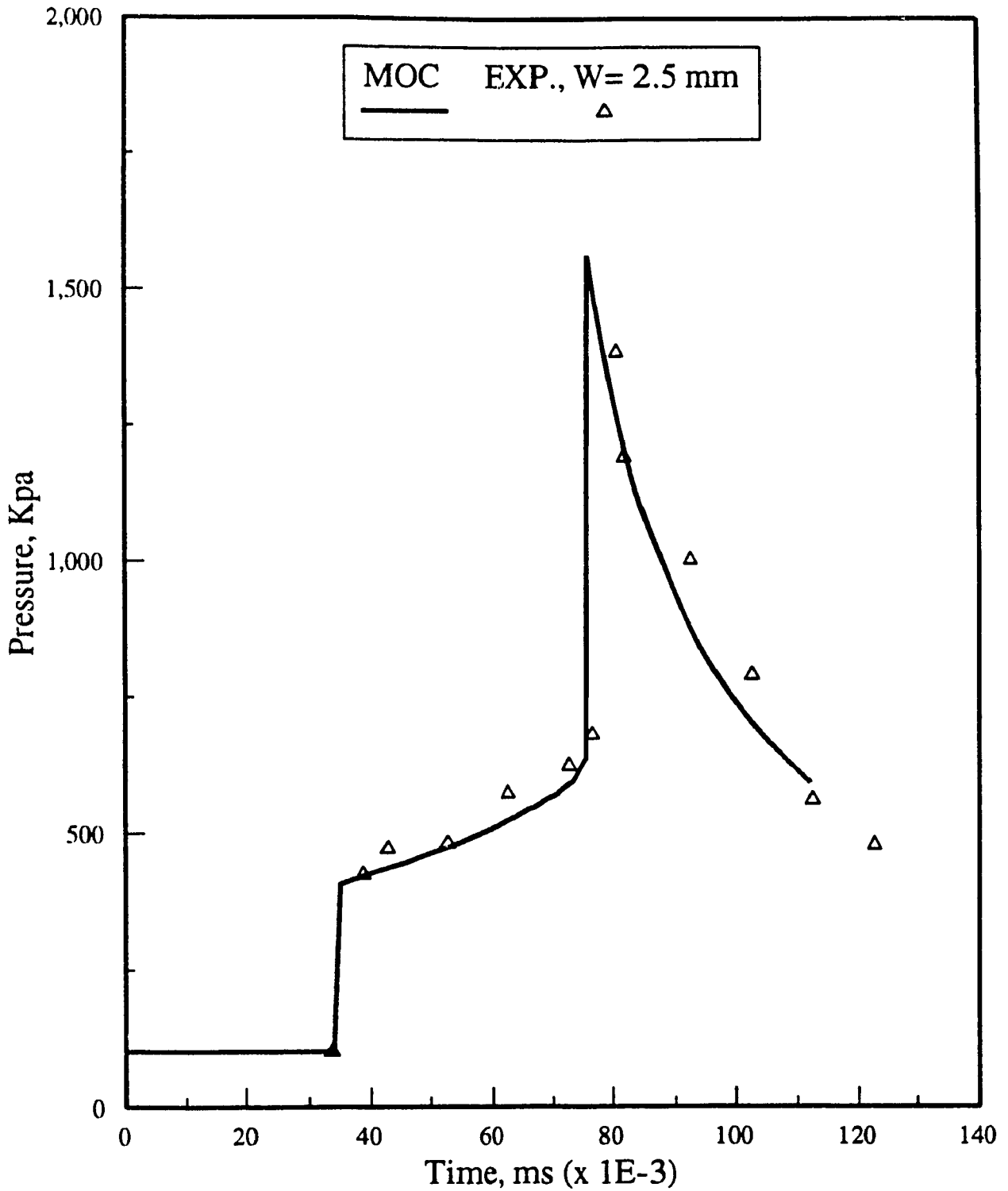


Figure 4.19. Pressure history for $M_o=1.26$, $W=2.5$ mm and $R=13.87$ mm, comparison of the experiments with the results obtained using the method of characteristics.

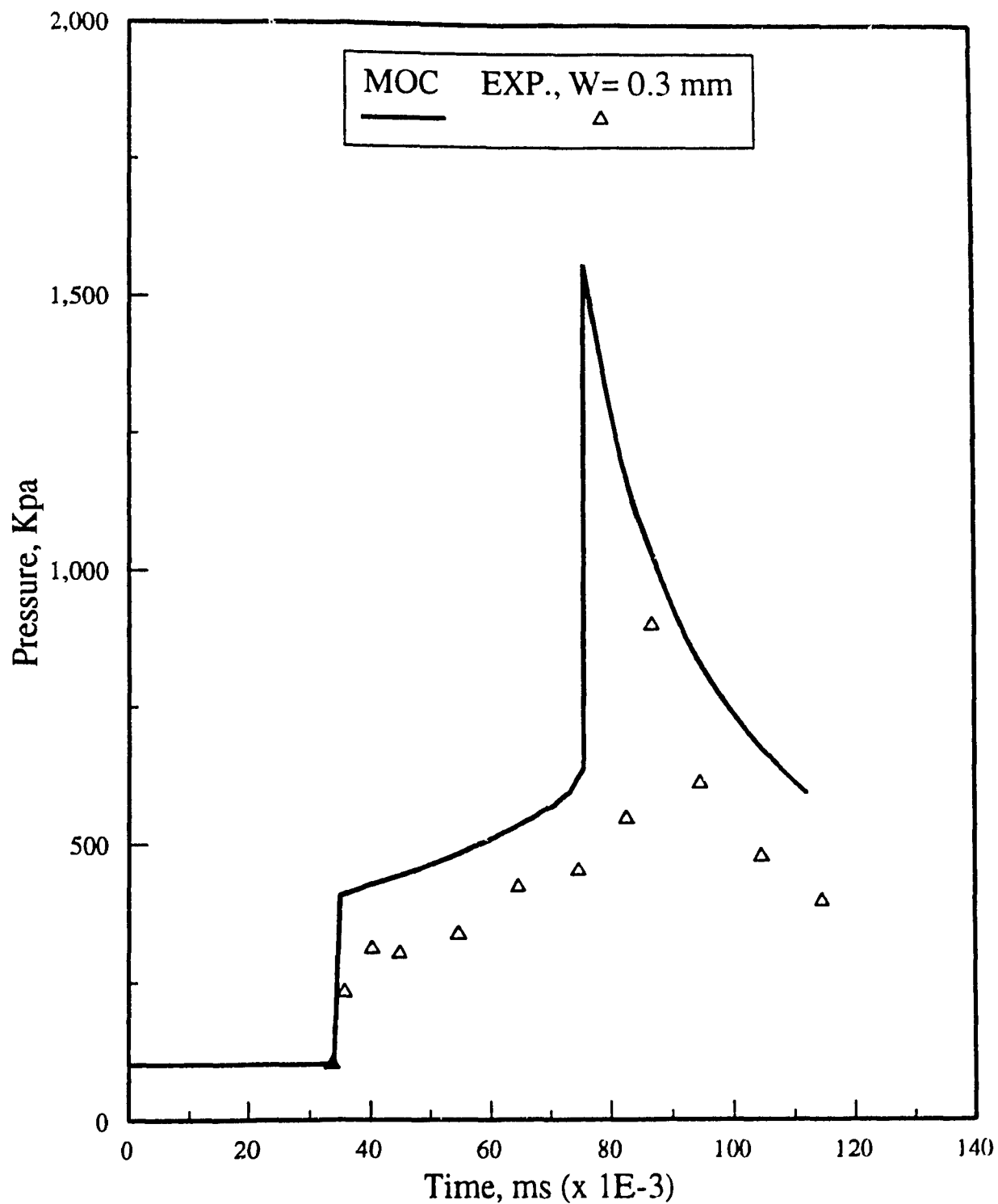


Figure 4.20. Pressure history for $M_o=1.26$, $W=0.30$ mm and $R=13.87$ mm, comparison of the experiments with the results obtained using the method of characteristics.

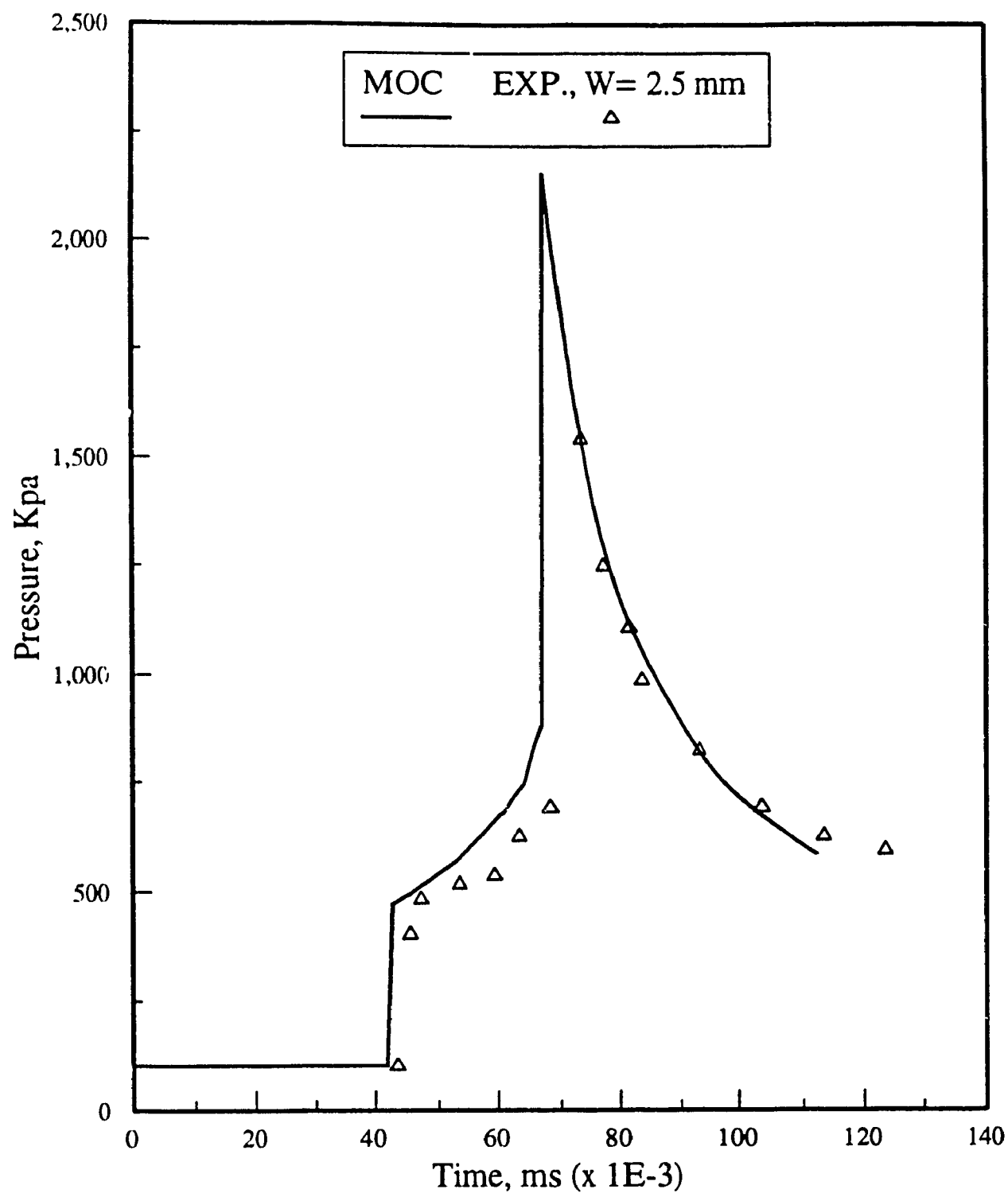


Figure 4.21. Pressure history for $M_0=1.26$, $W=2.5$ mm and $R=8.89$ mm, comparison of the experiments with the results obtained using the method of characteristics.

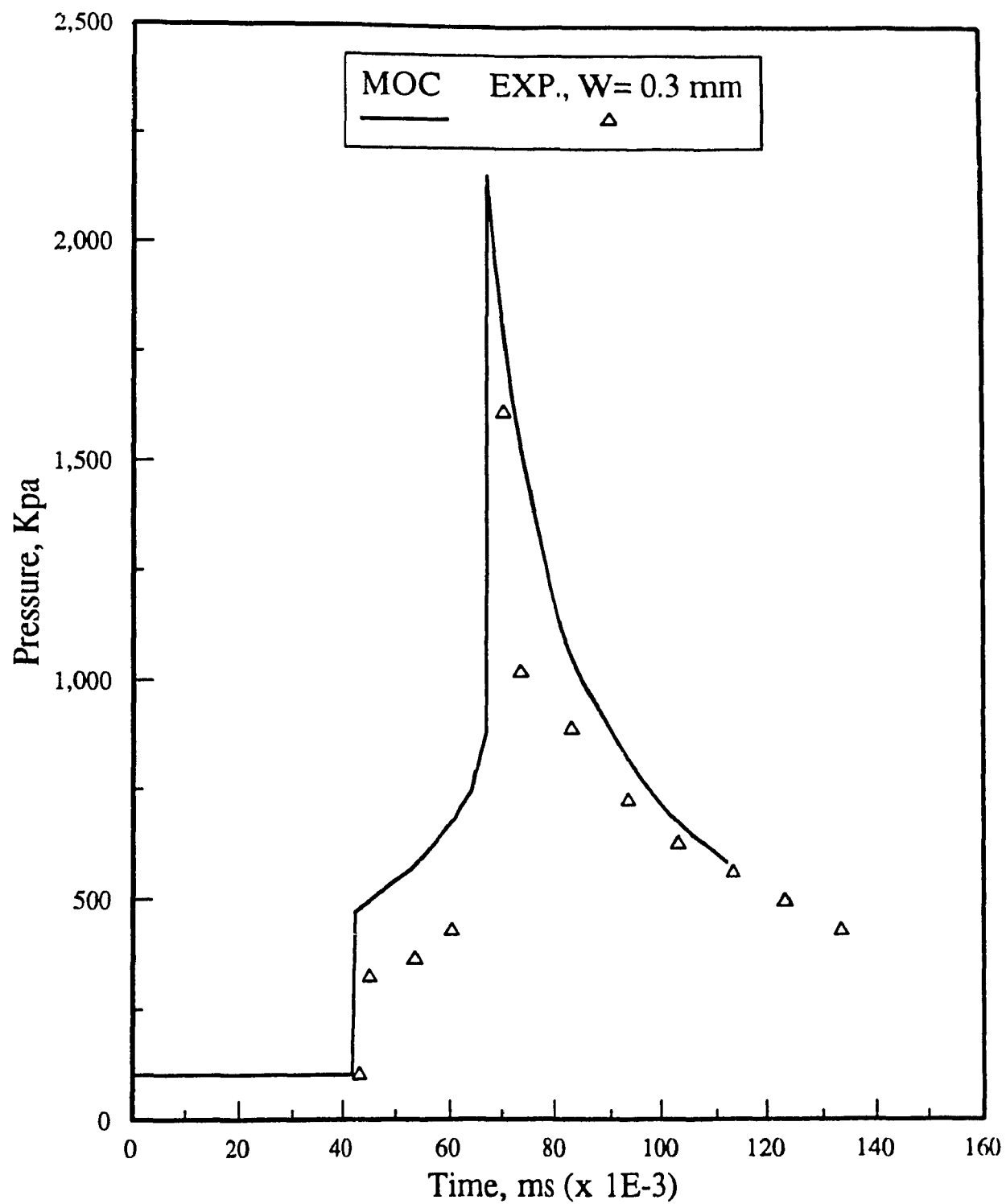


Figure 4.22. Pressure history for $M_o=1.26$, $W=0.3\text{ mm}$ and $R=8.89\text{ mm}$, comparison of the experiments with the results obtained using the method of characteristics.

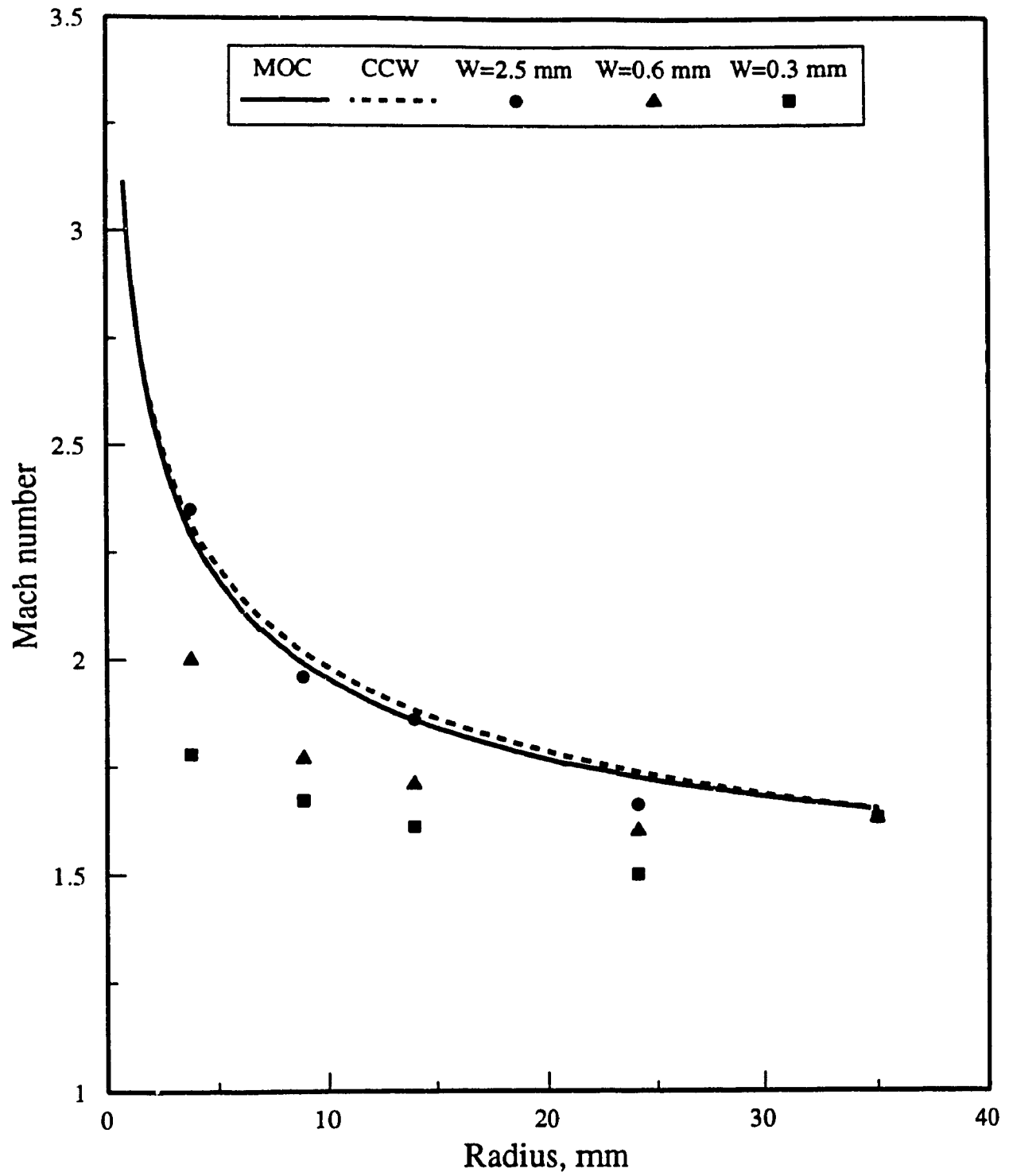


Figure 4.23. Shock Mach number versus radius for $M_o=1.26$ with $W=2.5$ mm, 0.6 mm and 0.3 mm

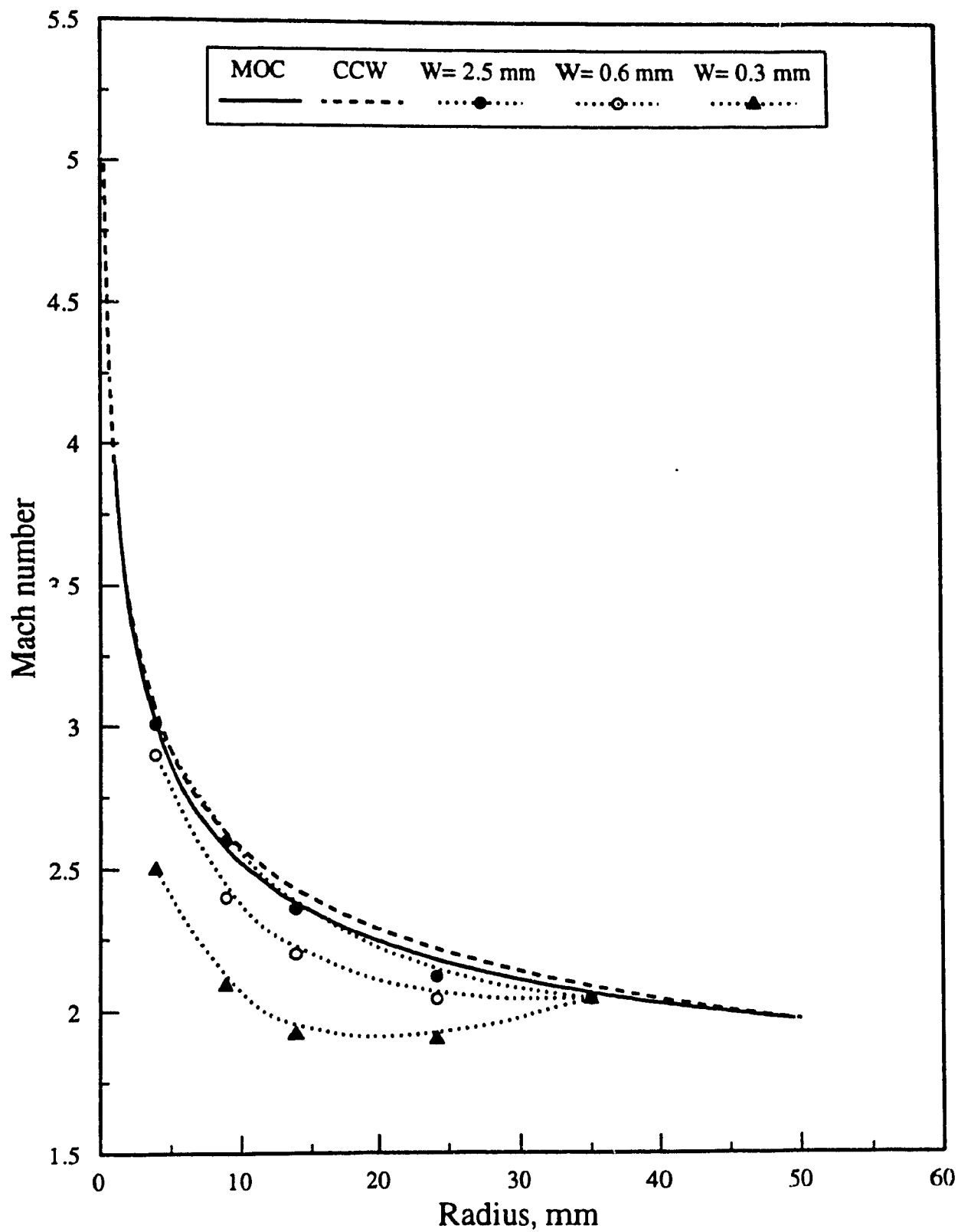


Figure 4.24 Shock Mach number versus radius for $M_o=1.44$. The dotted lines represent data obtained using equation (4.7)

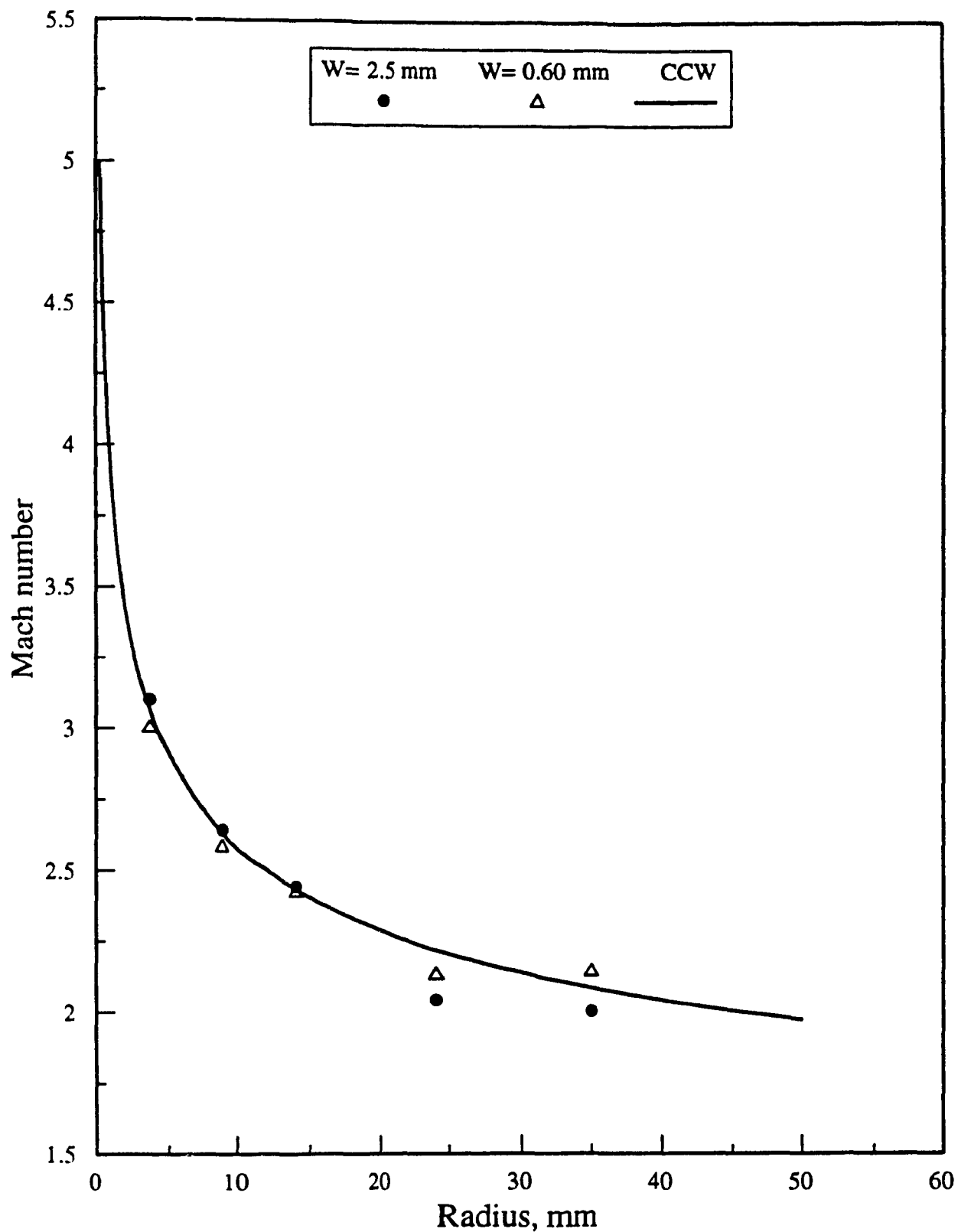


Figure 4.25. Shock Mach number versus radius for $M_0=1.44$ using the original model

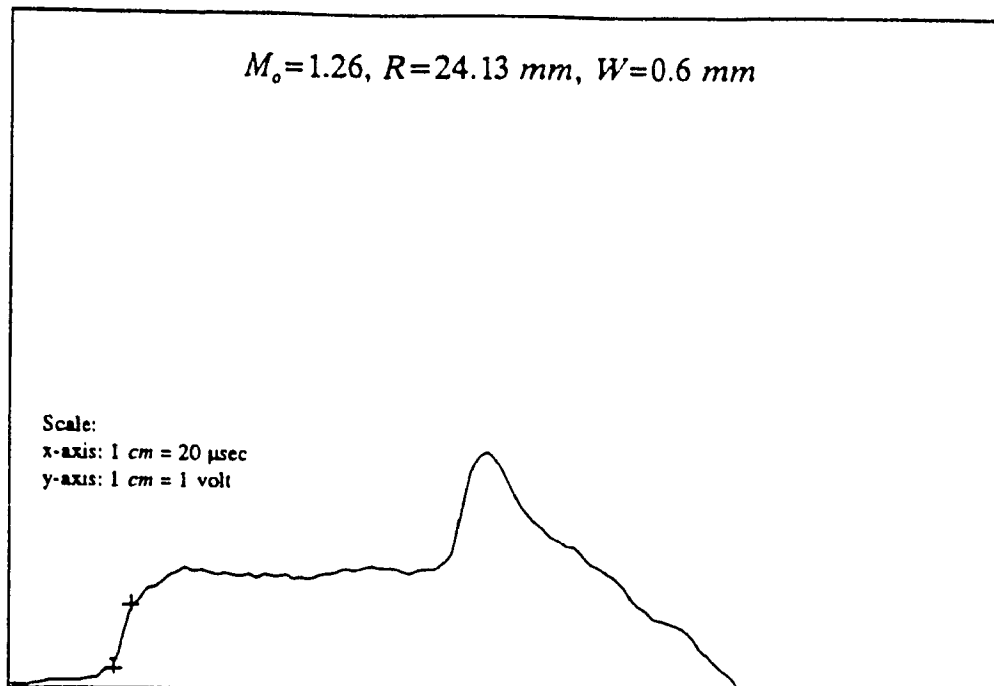


Figure 4.26a

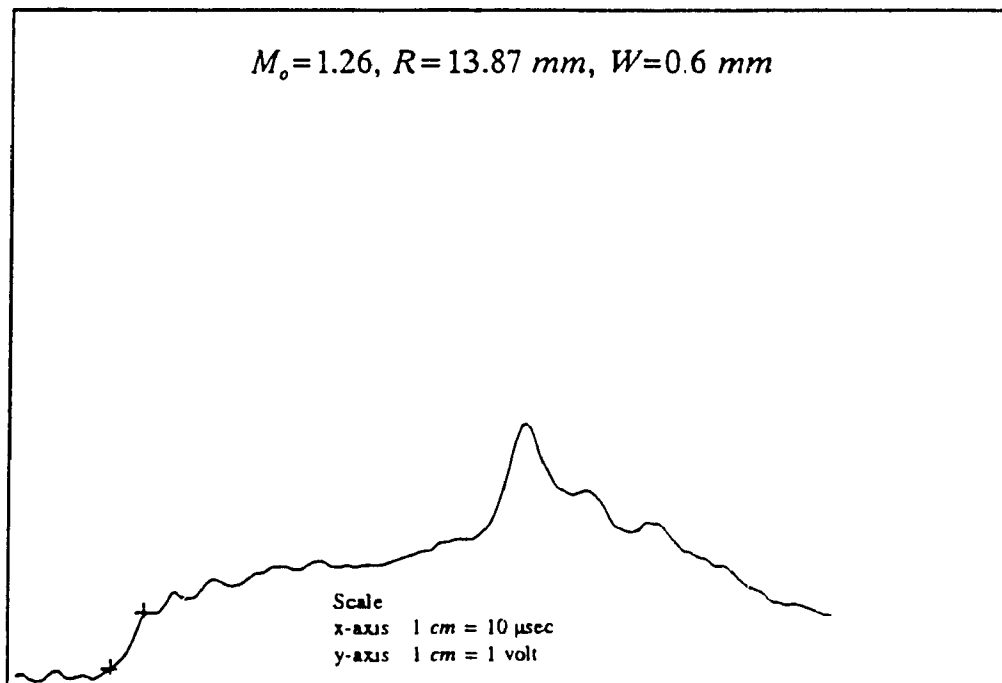


Figure 4.26b

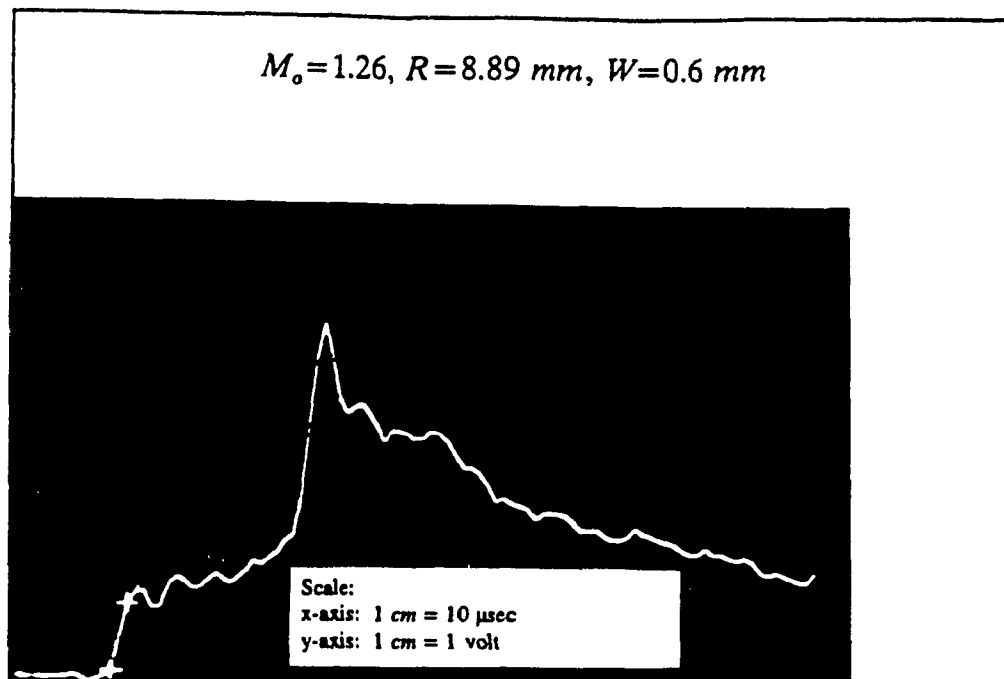


Figure 4.26c

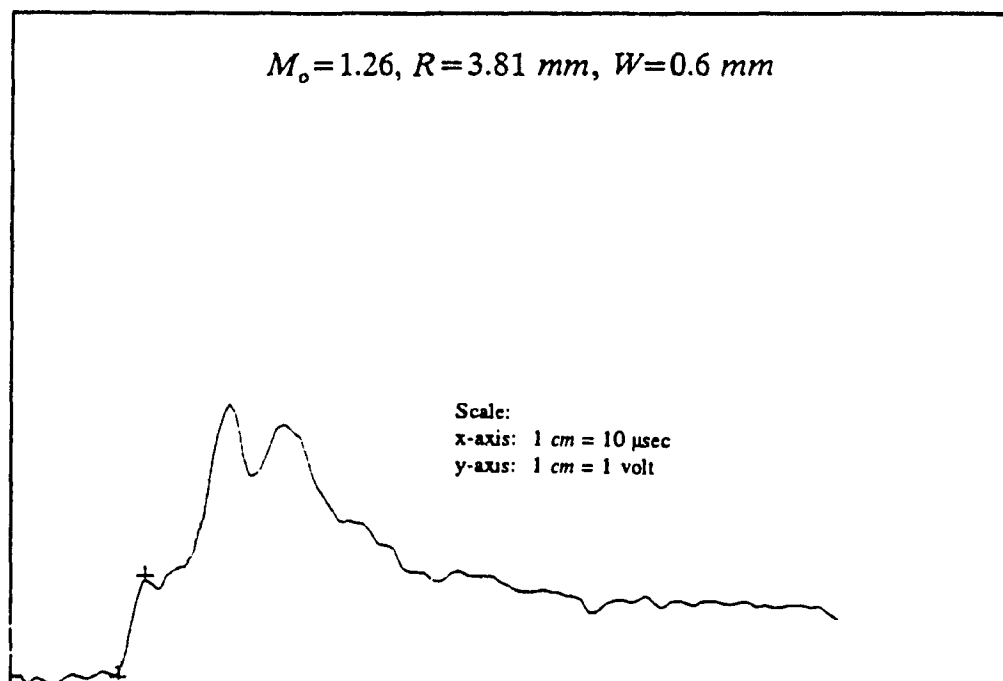


Figure 4.26d

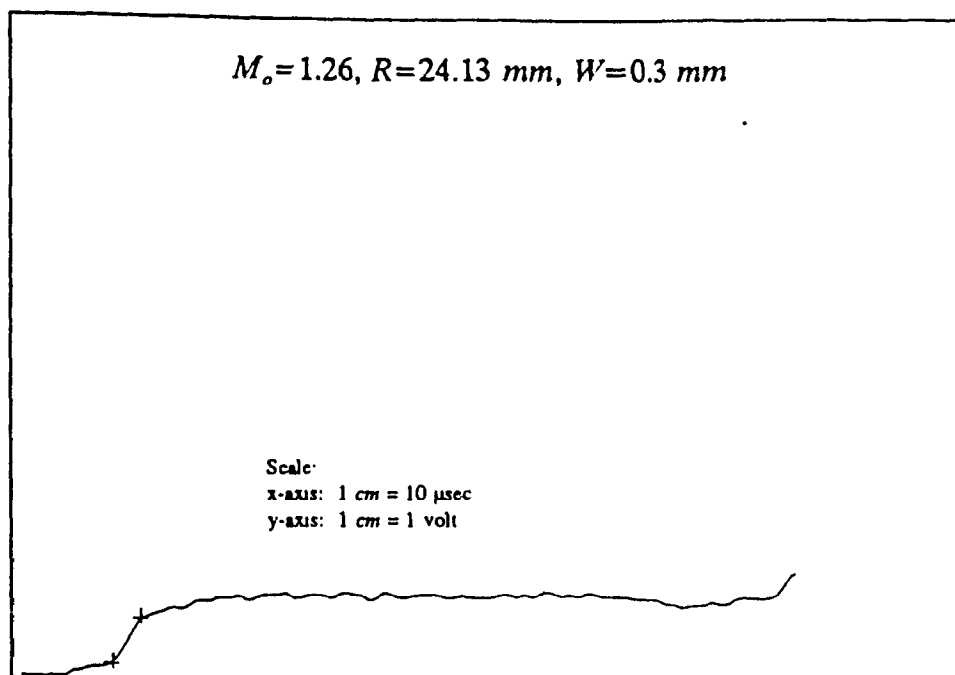


Figure 4.26e

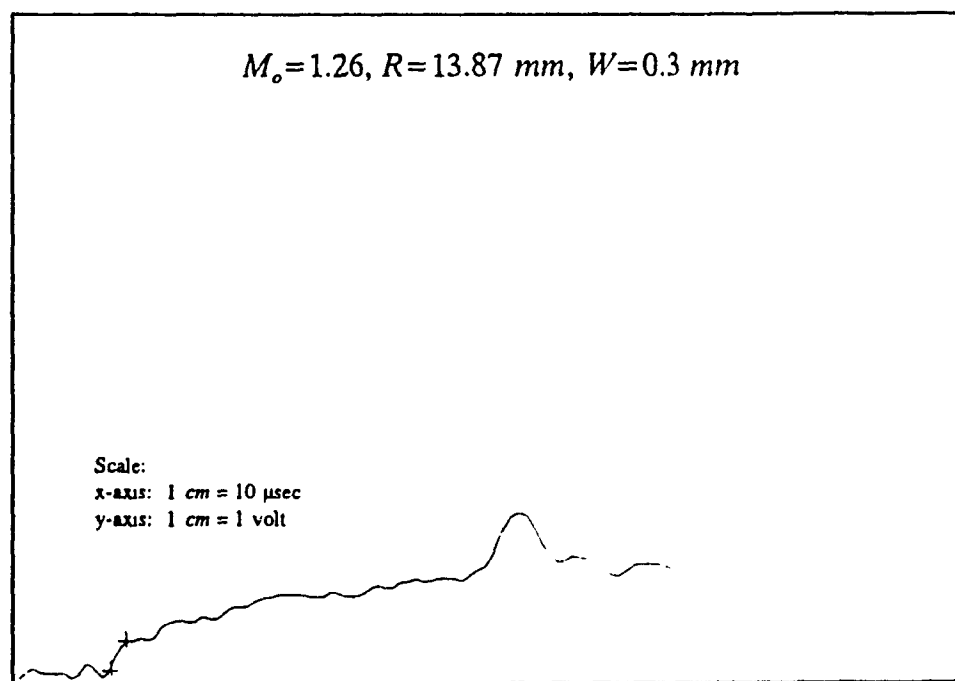


Figure 4.26f

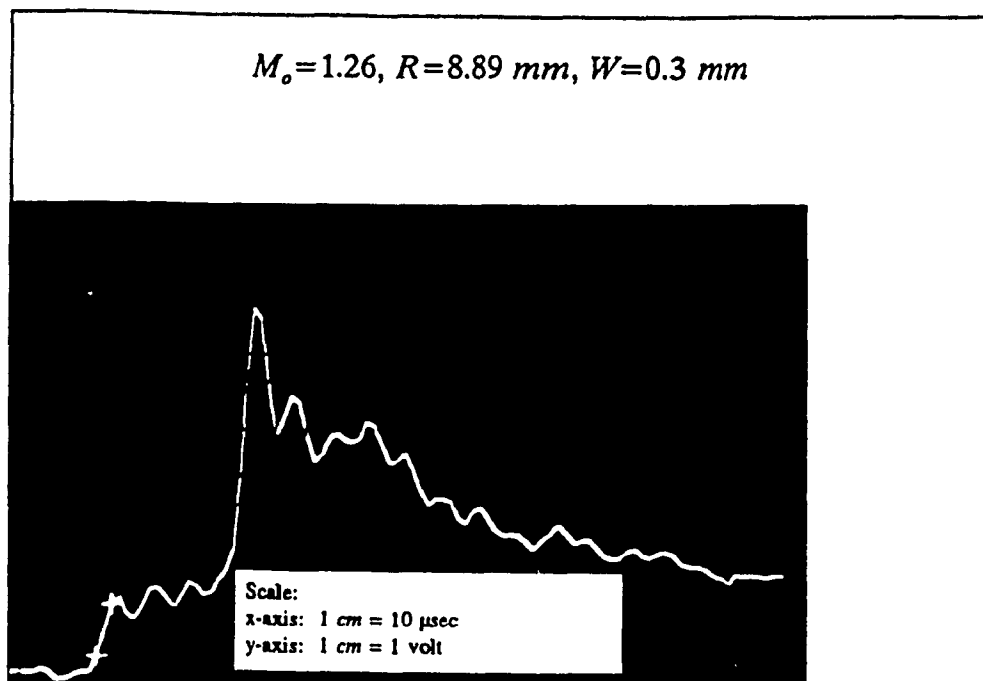


Figure 4.26g

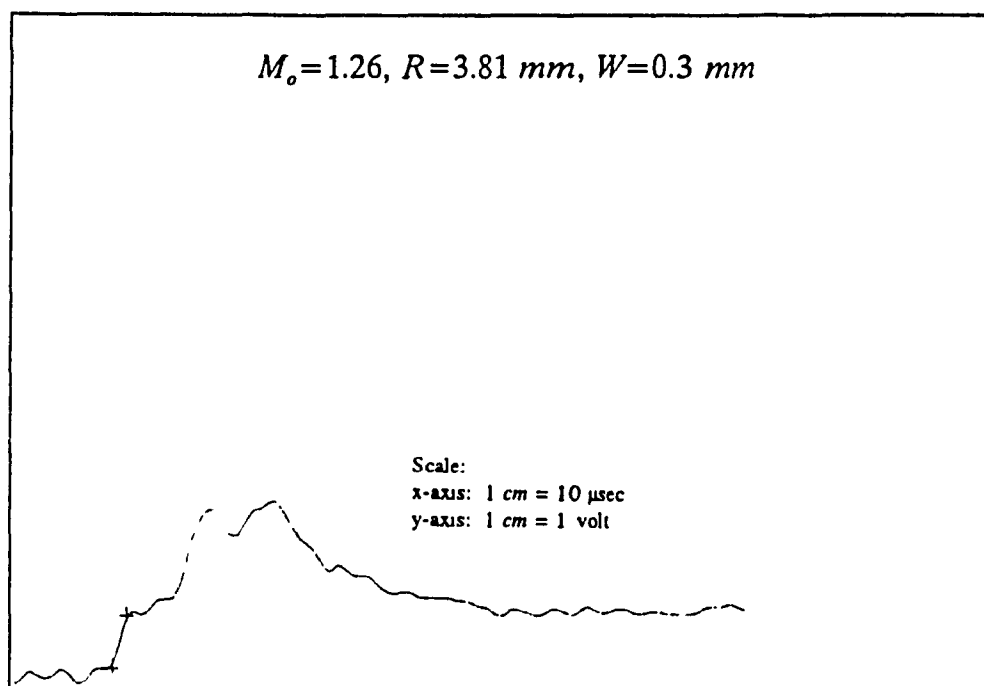


Figure 4.26h

Figure 4.26 . Oscilloscope traces for $M_o=1.26, R=24.13 \text{ mm}, 13.87 \text{ mm}, 8.89 \text{ mm}$ and $3.81 \text{ mm}, W=0.6 \text{ mm}$ and 0.3 mm .

(a)

(b)

(c)

(d)

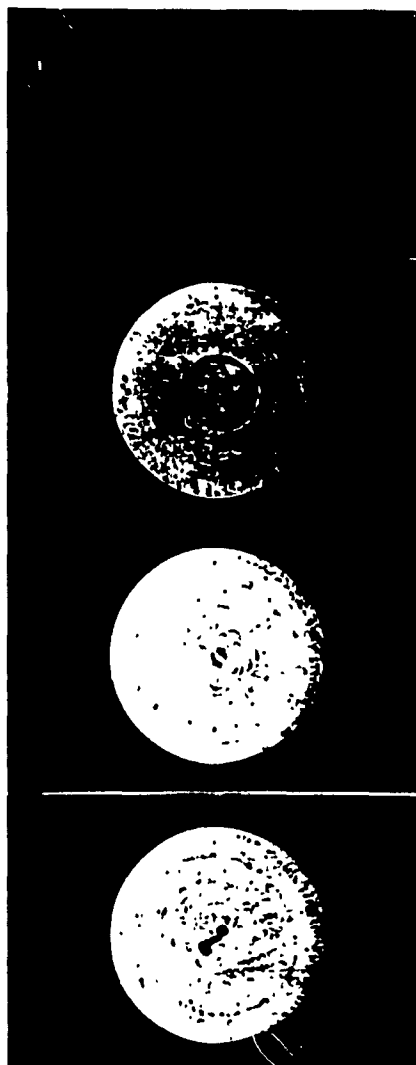


Figure 4.27 Spark shadowgraphs illustrating the propagation of cylindrical shock wave in a narrow cylindrical chamber for $M_0=1.26$ and $W=0.6 \text{ mm}$

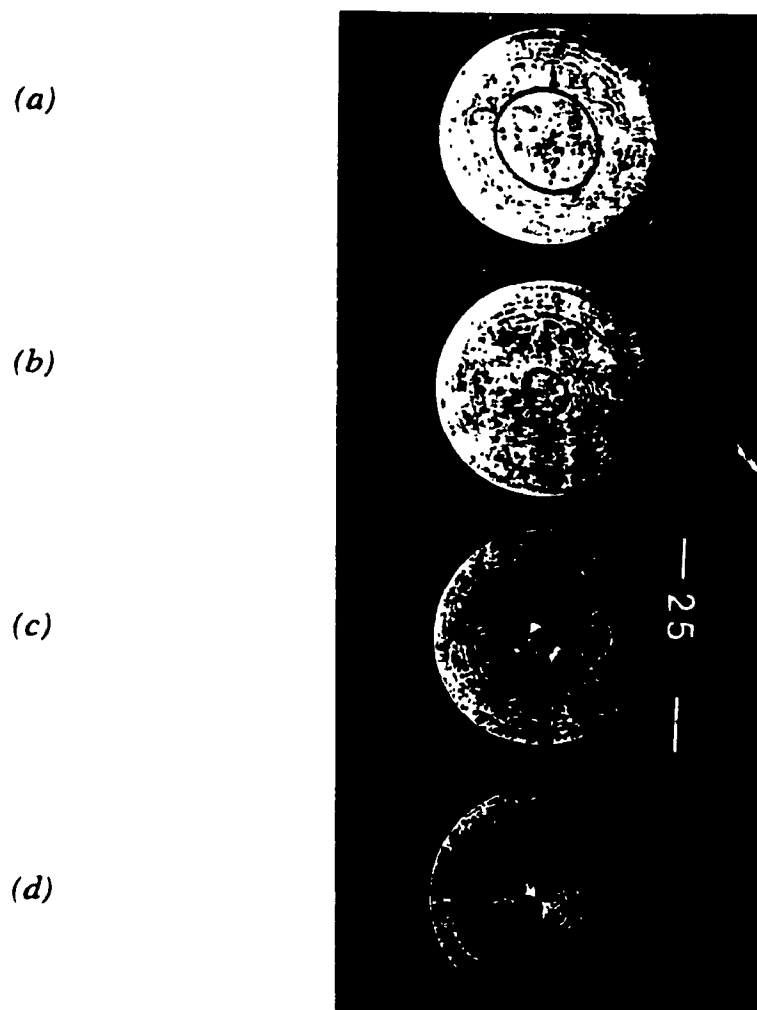
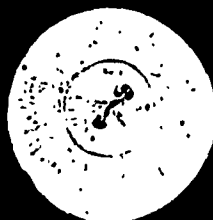


Figure 4.28 Spark shadowgraphs illustrating the propagation of cylindrical shock wave in a narrow cylindrical chamber for $M_o=1.26$ and $W=0.3 \text{ mm}$

(e)



(f)

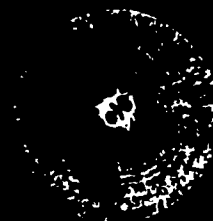


Figure 4.28 (continued)

(a)

(b)

(c)

(d)



Figure 4.29 Spark shadowgraphs illustrating the propagation of cylindrical shock wave in a narrow cylindrical chamber for $M_o=1.26$ and $W=2.5\text{ mm}$

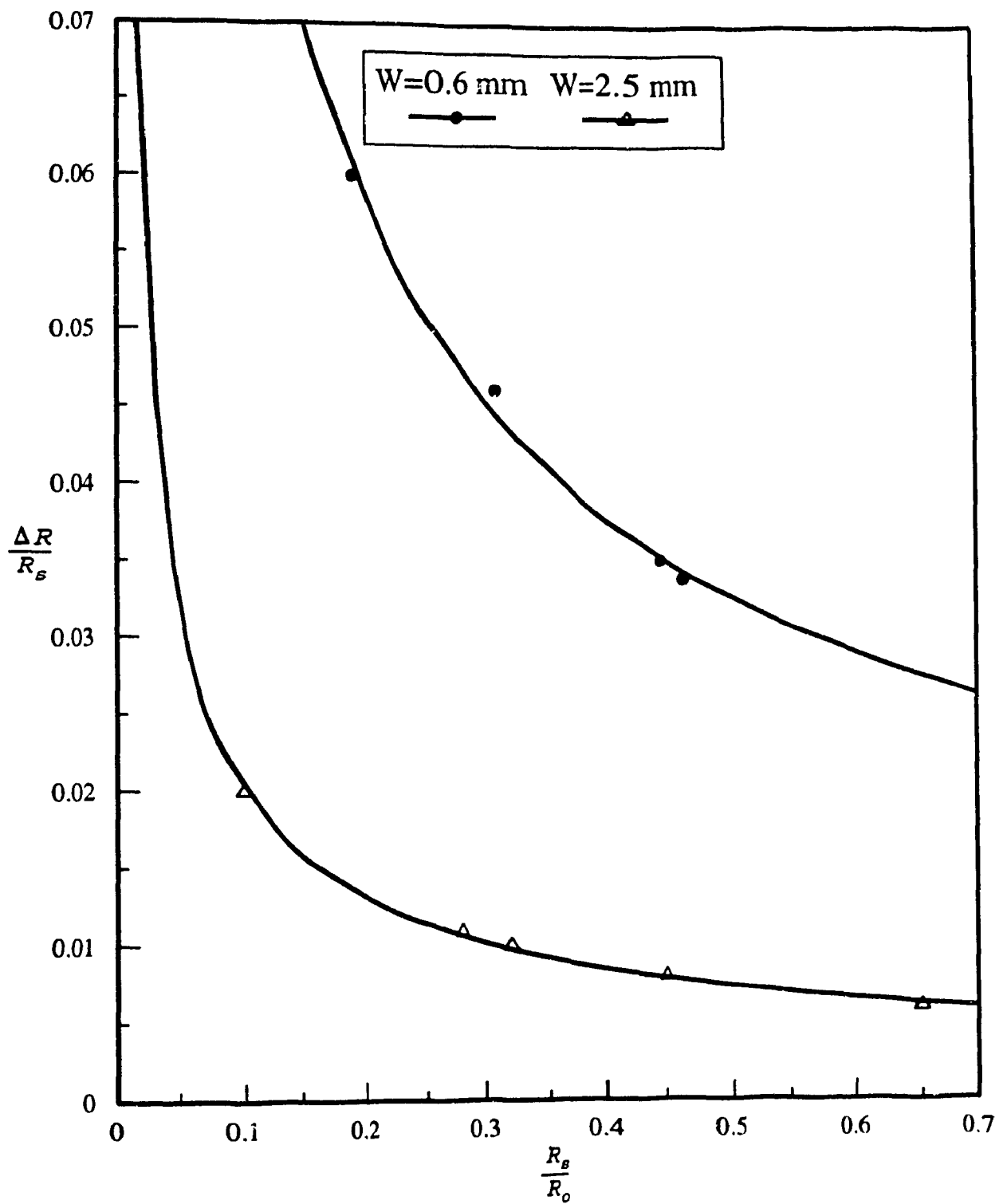


Figure 4.30 Rate of propagation of the converging cylindrical shock for $M_o = 1.26$

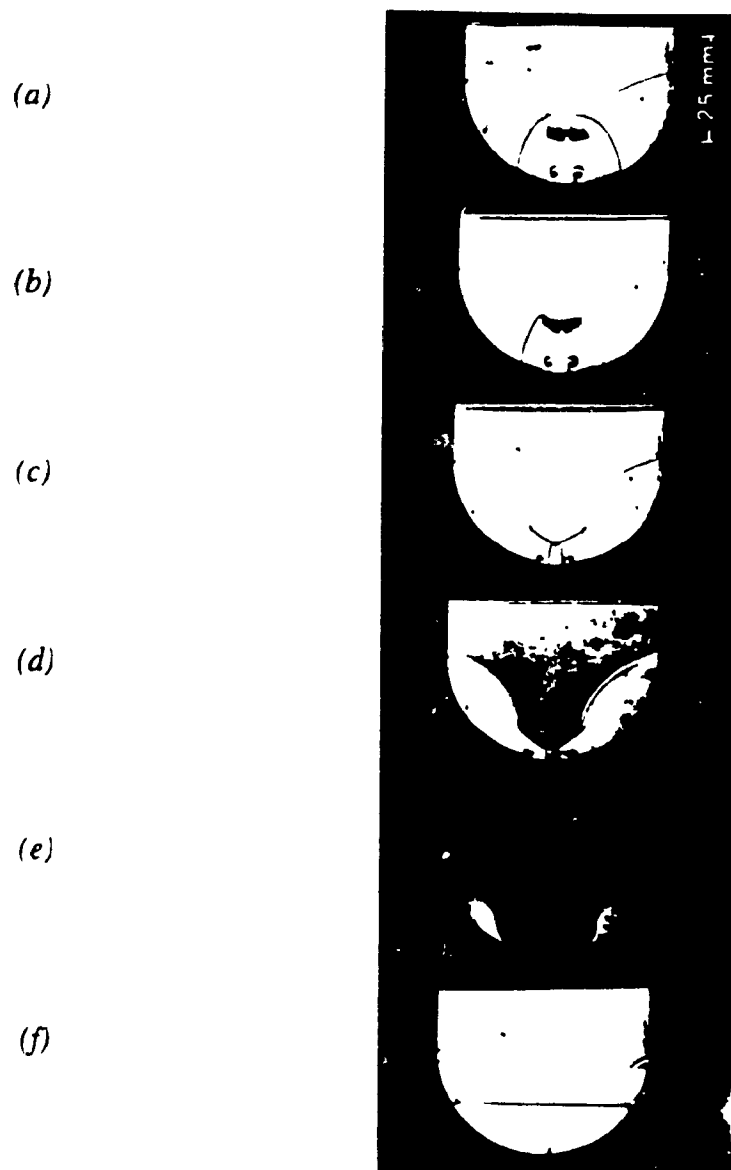


Figure 4.31 Spark schlieren photographs of plane shock reflection from a semi-circular end wall, $M_\infty = 2.2$